Measurement of the Production Cross Section for $W + \gamma$ in the Electron Channel in $\sqrt{s} = 1.8$ TeV $\bar{p}$-p Collisions

A Dissertation

submitted by

Douglas P. Benjamin

In partial fulfillment of the requirements

for the degree of

Doctor of Philosophy

in

Physics

Tufts University

November, 1993

Abstract

The production cross section times decay branching ratio for $W+\gamma$ in the electron decay channel in $\sqrt{s} = 1.8$ TeV $\bar{\text{p}}$-p collisions has been measured using $W \rightarrow e\gamma$ data sample obtained from the CDF 1988-89 Tevatron collider run. For photons in the central region ($|\eta_\gamma| < 1.1$) of the CDF detector with transverse energies $E_T^\gamma > 5.0$ GeV and lepton-photon angular separation $\Delta R_{\ell\gamma} > 0.7$, eight electron $W\gamma$ candidates were observed. From these events, the production cross section times decay branching ratio for the electron sample was measured to be: $\sigma \cdot B(W\gamma)_{exp} = 17.0^{+13.6}_{-13.4}(\text{stat.} + \text{syst.})\,\text{pb}$. The $W\gamma$ cross section is sensitive to the anomalous couplings of the W boson. Using the $W\gamma$ cross section measurement, the absence of an excess of large E_T photons accompanying the production of a W boson enables one to obtain direct limits on anomalous $WW\gamma$ couplings. The experimental limits on the anomalous couplings was measured to be: $-7.2 < \Delta\kappa < +7.7$ ($\lambda = 0$) and $-3.5 < \lambda < +3.4$ ($\Delta\kappa = 0$) at 95% CL. These experimental limits impose contraints on possible internal structure of the W boson with compositeness scale sensitivity $\Lambda_W \geq 1\,\text{TeV}$ for saturation of unitarity, corresponding to probing a distance scale of order $L_W \leq 2.0 \times 10^{-4}\,\text{fm}$. The experimental limits on anomalous $WW\gamma$ couplings place bounds on the higher-order electromagnetic moments of the W boson – the magnetic dipole and electric quadrupole moments and the W boson mean-squared charge radius. The experimental results presented in this thesis are in good agreement with Standard Model expectations.

Dedication

This work is dedicated to my loving father-in-law, Dr. Paul Nash, who died shortly before I could defend this thesis. He was looking forward to my obtaining a Ph.D. and would have been very proud.

Acknowledgments

I would like to begin by thanking my advisor Krzysztof Sliwa for giving me the opportunity to pursue my graduate research at the Collider Detector at Fermi Lab (CDF). His guidance was invaluable.

I have enjoyed collaborating with Professor Steve Errede of University of Illinois at Urbana-Champaign. He has been a wise and thoughtful mentor and a good friend. Thank you to Professors Steve and Debbie Errede for their generous hospitality during my work at the University of Illinois.

I would like to thank Ulrich Baur for his enormous help and the extensive use of his Monte Carlo programs.

I would also like to thank the members of the W gamma analysis group at CDF for their help. I especially thank Dr. Mike Lindgren for his perseverance through many versions of this thesis and for his help during my analysis.

I am grateful to Professor Melissa Franklin and Dr. Jimmy Proudfoot for providing ongoing support and direction during my time at Fermi Lab. I want to thank Dr. Brian Harral for his thoughtful advice on this thesis and for his long suffering work during our "sentence" at the test beam together.

My thanks go out to Professor Richard Milburn for his years of interest in my physics career. I also want to thank the rest of the High Energy Physics group at Tufts University for all of their help during my graduate career. Thank you to Dr. Stephane Willocq for provided stimulating physics discussions throughout our time together as office mates at Tufts. Thank you to Dr. Matthew Koss, whose caring and concern kept me on track numerous times early in my career at Tufts. Thank you to Bill Miller for making my stays at Soudan, Minnesota a joy. Thank you to my friends at Fermi for making life a Fermi Lab more bearable.

My wife, Jenny, deserves many thanks for her hours of work proof reading my thesis, and for her unending patience as I pursue my physics career. A special thank you to my parents and parents-in-law for their generous love and support.

Table of Contents

List of Figures

List of Tables

Chapter 1

Introduction

The physical world around us is composed of major components: matter and the forces that interact with matter. Elementary particle physics tries to answer the question "What is matter?" on the most fundamental level. This branch of physics strives to understand matter in the form of minute particles (quarks and leptons, whose size is $\ll 10^{-15}$ m) and the forces that govern their interactions. The current understanding of the known quarks and leptons is summarized in Table 1.1 from reference [1]. Elementary particle physics is a science which has evolved over the past one hundred years and in which exciting discoveries are still made today.

There are four fundamental forces in Nature: strong, electromagnetic, weak and gravitational. These forces are summarized in table 1.2. Each of these forces is assumed to be mediated by the exchange of a particle. The gravitational force is described classically by Newton's law of universal gravitation. The graviton is thought to mediate the gravitational force though no graviton has been seen experimentally. The electromagnetic (EM) force describes the visible light that we see in our everyday world. Radio waves are also a manifestation of electromagnetism. Maxwell's equations, formulated over one hundred years ago, describe the EM force on a macroscopic scale. The photon mediates the EM force on a microscopic scale. The strong nuclear force describes the binding together of quarks to form neutrons and protons. The strong force also describes the binding of neutrons and protons to form nuclei. The gluon is the mediator for the strong force. The weak force first presented by Fermi in 1933 to explain radioactivity was further refined by Lee and

Table 1.1: Fundamental Fermions - Quarks and Leptons

Quarks			Leptons		
Flavor	Mass (MeV/c^2)	Charge (e)	Flavor	Mass (MeV/c^2)	Charge (e)
U Up	$2-8$	$+\frac{2}{3}$	ν_e	$< 7 \times 10^{-6}$	0
D Down	$5-15$	$-\frac{1}{3}$	e Electron	0.511	-1
C Charm	$1300-1700$	$+\frac{2}{3}$	ν_μ	< 0.27	0
S Strange	$100-300$	$-\frac{1}{3}$	μ Muon	105.6	-1
T Top	$> 1.1 \times 10^5$	$+\frac{2}{3}$	ν_τ	< 35	0
the TOP quark has NOT been discovered					
B Bottom	$4700-5300$	$-\frac{1}{3}$	τ	1777	-1

Yang, Feynman, Gell-Mann and many others in the 1950's. In this theory the intermediate vector bosons $W^{\pm}$ and Z are responsible for transmitting the weak force between quarks and leptons.

The small size of elementary particles dictate that quantum mechanics be used to describe their behavior. In addition these particles are often traveling at or very close to the speed of light, c. Any theory describing them must obey the laws of Special Relativity. Quantum field theories are the relativistic analogue to quantum mechanics.

The oldest, simplest, and most successful of the quantum field theories describes the electromagnetic force. The theory of Quantum Electrodynamics (QED) was developed by Tomonaga, Feynman and Schwinger in the 1940's. This theory describes the interaction between the photon, the massless "force particle" and electrically charged matter[1].

[1]Electric Charge is a fundamental property of a particle. Some elementary particles are charged

Table 1.2: Fundamental Forces in Nature

Force	Relative Strength	Range	Mediator	Source	Typical Interaction time scale
Strong	$\alpha_s \sim 1$	≤ 1 fm	gluon	"Color Charge"	10^{-23} sec
EM	$\alpha_{em} \sim \frac{1}{137}$	∞	photon	Electric Charge	10^{-20} sec
Weak	10^{-5}	$\sim 10^{-3}$ fm	$W^{\pm}$ and Z	"Weak Charge"	10^{-8} sec
Gravity	10^{-38}	∞	graviton	Mass	∞

While developing QED, Richard Feynman invented a schematic method for representing the interaction between forces through their mediators and matter. These diagrams are extremely useful in understanding the physics of an interaction. Feynman showed that all electromagnetic phenomena are ultimately reducible to the process shown in figure 1.1 This diagram tells us that a charged particle (represented by X) enters, emits (or absorbs) a photon, γ, and exits. This vertex diagram contains information about the strength of the coupling between the charged particle and the photon. To describe more complicated processes, several vertices are connected. For example Compton scattering, $e + \gamma \rightarrow e + \gamma$, can be described by the Feynman diagrams in figure 1.2.

QED is the most successful of the physics theories. The magnetic moment of the electron, generated by the innate electron spin, has been calculated to infinitesimal precision. QED's description of the electromagnetic interaction has been verified over the range of distances from 10^{-18} meters to more than 10^{8} meters. QED sets the standard for the new theories that describe the interaction between fundamental particles.

In the 1960's Glashow, Weinberg, and Salam each proposed a new theory that

(*i.e.* have charge). Neutral particles have no electric charge associated with them

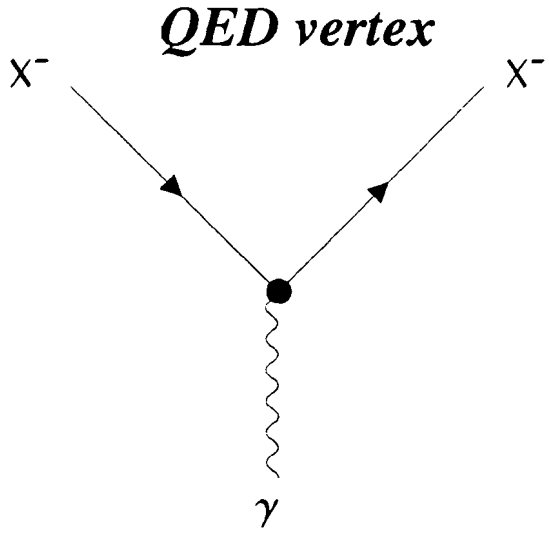

Figure 1.1: QED vertex: Time flows from left to right. An incident charged particle X^- emits (or absorbs) a photon, γ, then exits.

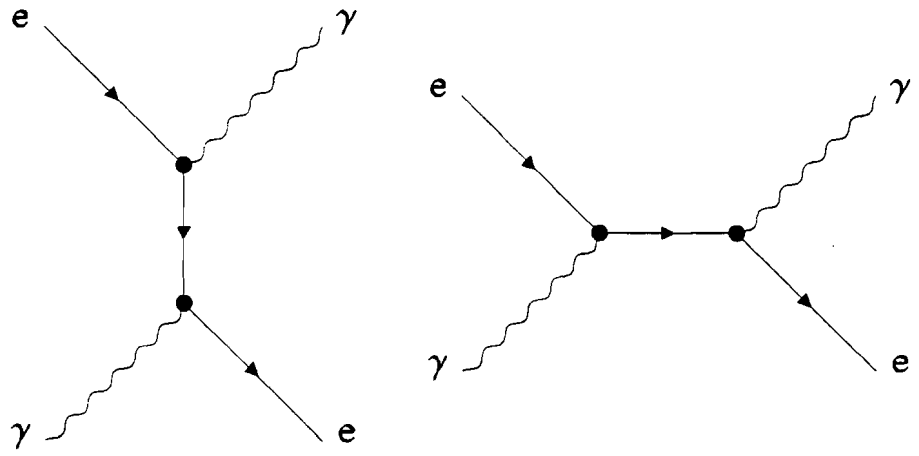

Figure 1.2: Compton Scattering: Time flows from left to right. An incident electron and photon scatter with a electron propagator. The resulting electron and photon exit with new energy and momenta. Fermion arrows pointing in the direction of increasing time indicate a particle. Reversed fermion arrows indicate an antiparticle (positron).

would unify the electromagnetic and weak forces. This theory, now called the Standard Model (SM) of electroweak interactions, unifies the electromagnetic and weak interactions into a single electroweak interaction [2]. Three intermediate vector bosons (massive particles with spin = 1), $W^{\pm}$ and Z°, and the photon serve as mediators (or "force particles") in this new theory. The Standard Model has to account for the fact that although the electromagnetic and weak forces are intimately related, these interactions do not look at all alike in the everyday world. In order to accomplish this feat, the underlying phenomena uniting the interactions are apparent at high energies and are concealed at lower energies. In this theory the charged vector bosons, W^{+} and W^{-}, mediate the charged current interactions [2]. Neutral current interactions are mediated by either the Z° boson or the photon [3].

Like any good theory describing the interactions between matter (*e.g.* QED), the Standard Model makes experimentally verifiable predictions. The intermediate vector bosons $W^{\pm}$ and Z° are predicted to be massive: [3]

$$M_{W^{\pm}} = \frac{37}{\sin\theta_W}\,\mathrm{GeV/c^2} \quad , M_{Z^{\circ}} = \frac{74}{\sin 2\theta_W}\,\mathrm{GeV/c^2} \quad :$$

where θ_W (the Weinberg angle) is a parameter in the theory. For comparison the proton mass is $M_p \sim 0.938\,\mathrm{GeV/c^2}$. Neutral weak currents are predicted by the Standard Model. The Standard Model also predicts that there are direct couplings of the $W^{\pm}$ and Z° to each other as shown in figure 1.3. Moreover, since the W boson has electric charge, it couples to photons (see figure 1.4). Experimental verification of these predictions confirms the model. The first experimental evidence for neutral weak currents came from a neutrino experiment conducted at CERN in 1973. [4] In 1983 the W [5] and Z [6] intermediate vector bosons were discovered at CERN.

Because the W and Z are so massive, their production presents some tricky

[2]Charged current interacts are interactions between particles where mediator must carry electric charge in order to conserve charge conservation: $W \rightarrow e\bar{\nu}_e$

[3]In neutral current interactions there is not change in electric charge between the interacting particles: $Z^{\circ} \rightarrow e^{+}\,e^{-}$

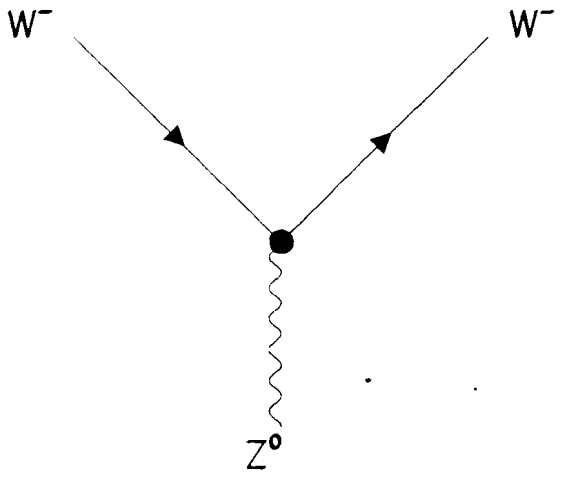

Figure 1.3: WWZ vertex: Feynman diagram showing the coupling allowed by the Standard Model of W^- intermediate vector boson to the Z° intermediate vector boson.

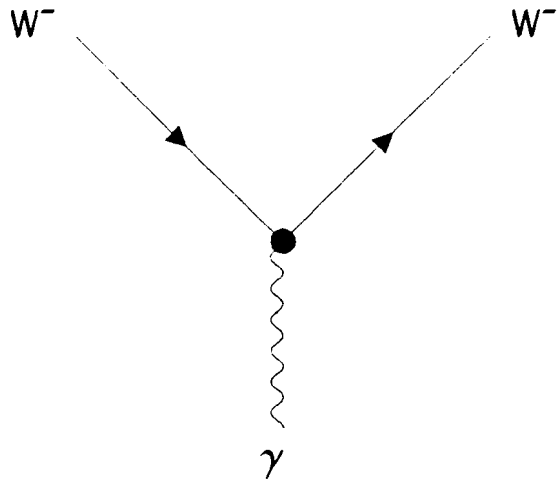

Figure 1.4: $WW\gamma$ vertex: Feynman diagram showing the coupling allowed by the Standard Model of W^- intermediate vector boson to the photon, γ since the W boson has electric charge.

problems. In order to get the energy required to produce the W and Z, particles (like protons) must be collided together to release the required amount of energy needed to produce these very heavy particles. Figure 1.5 shows the amount of energy available for creation of new particles when a beam of particles with energy E strikes a stationary target or when two beams collide with each other. Particle detectors capable of detecting the production of the W and Z boson have to be large devices in order to accurately measure the energy released when the W and Z decay. These detectors must also be hermetic because one does not know *a priori* where the decay products of the W and Z (*i.e.* $W \rightarrow \ell\nu$; $Z \rightarrow \ell\ell$) will go. The Tevatron is a particle accelerator capable of colliding beams of large enough energy ($E_{\text{beam}} \sim 900\,\text{GeV}$) and high enough luminosity [4] to produce enough W's to be detected in a large multi-purpose detector like the Collider Detector at Fermilab (CDF). The CDF detector, first proposed in the late 1970's, is capable of accurately measuring the decay products of W and Z production. The CDF detector will be described in detail in chapter 3. The analysis described by this thesis used data from W's produced in the Tevatron and recorded by the CDF detector.

As mentioned previously, the Standard Model predicts that the W boson and the photon will couple (*i.e.* interact with each other). The experimental determination of the strength of this coupling provides another test of the model. The Standard Model prediction for the cross-section [5] of $W\gamma$ production is over 100 times smaller than that for inclusive W production. Unfortunately, this makes the detection of the $W\gamma$ coupling very difficult (see figure 1.4 for the Feynman diagram of this coupling). The rare process of W production ($\bar{p}p \rightarrow WX$) with a cross-section at the Tevatron

[4] Luminosity is an experimental quantity defined as the number of high energy particles per square centimeter per second passing through the interaction region. W production is a rare process. In order to observe enough W bosons; particle accelerators need to have luminosities in excess of 10^{30} particles per square centimeter per second.

[5] The quantity σ refers to the cross-section of a process. The cross-section is the basic measurement of the probability of particles interacting. It is expressed as an effective target area (in units of cm^2 or barns where $1\,\text{b} = 10^{-24}\,\text{cm}^2$; $1\,\text{nb} = 10^{-33}\,\text{cm}^2$)

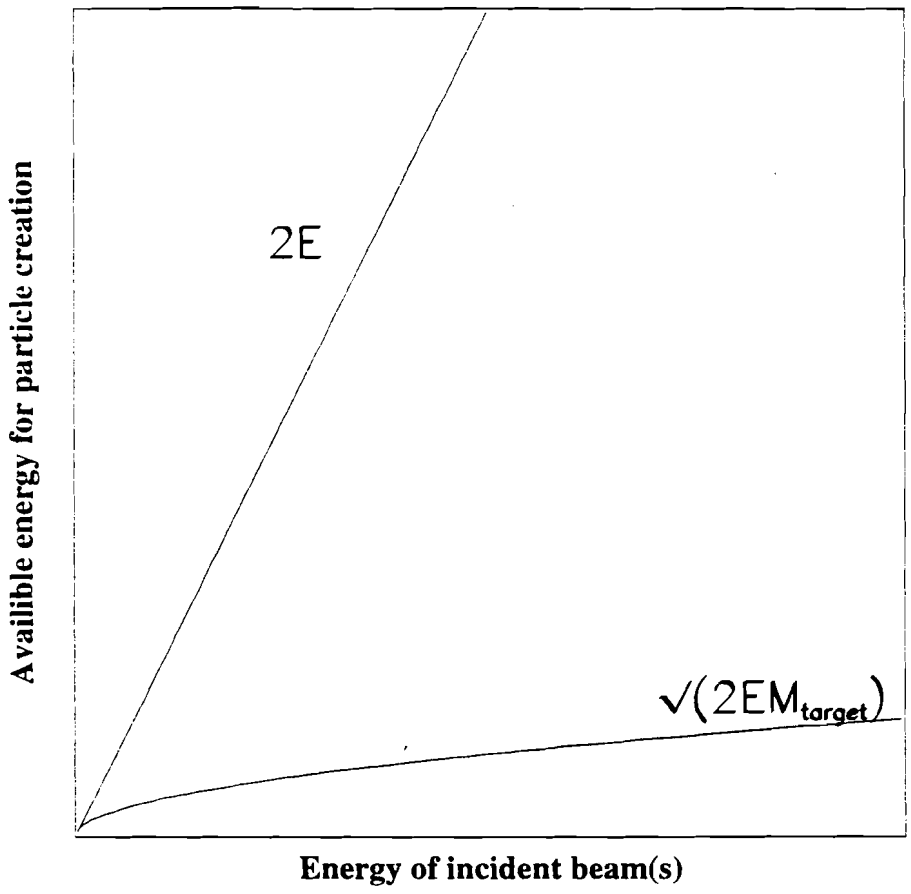

Figure 1.5: When a beam of particles of energy E in (GeV) strike a stationary target only $(2E \cdot M_{target})^{-1/2}$ is available for the creation of new particles; and increasing E does not produce a large increase in $(2E \cdot M_{target})^{-1/2}$, where M_{target} is the rest mass of the target particle. With colliding beams, each of energy E, a total of $2E$ is available for new particle creation. From reference [7]

of $\sigma_W \sim 22\,\mathrm{nb}$ [8] implies that the subprocess $W \rightarrow W\gamma$ is even more rare.

The measurement of the coupling strength of $W\gamma$ is further complicated by the presence of photons coming from other unrelated physics processes. These background processes will be discussed in detail in chapter 6.

In the Standard Model the W and Z bosons are fundamental particles in the same way that the photons and electrons are fundamental particles (*i.e.* fundamental particles have no internal substructure). From QED we see that the $ee\gamma$ coupling (figure 1.1) has a strength defined by $\alpha_{em} \sim \frac{1}{137}$. Large anomalous $WW\gamma$ couplings ($>> \alpha_{em}$) may be realized in nature only if the W has internal structure, *i.e.* if it is made up of still smaller, fundamental particles. In such a scenario, the W would then be viewed as a bound state of unknown particles, mediating the weak interactions. The W would take the role analogous to that of the $\rho-$mesons, which are mediators of the nuclear forces at low energy.

The experimental measurement of the $W^{\pm}\gamma$ di-boson production cross section and final-state decay kinematics provides a test of the predicted strength and nature of Standard Model $W\gamma$ coupling. This measurement also yields information on static electromagnetic multipole moments of the W bosons [9]. Composite models of the W bosons with large values of anomalous couplings predict cross sections for $W\gamma$ production well above those expected in the Standard Model. [11]

The inclusive electron W data sample obtained from the CDF 1988-89 collider run is used as a starting point for this analysis, since the $W\gamma$ events of interest are a subset of inclusive W boson production. The inclusive W data sample was used for measurements of the inclusive W and cross sections in the electron channel [12], and the W/Z cross section ratios [13]. In the analysis presented in this thesis, the same W event-selection criteria are used for defining the W boson in the $W\gamma$ event subsample. *Additionally*, the presence of an isolated, high energy photon accompanying the W boson is required in each event.

The small integrated luminosity presently available for studying $W\gamma$ process

leads us to anticipate that these measurements will have limited statistical precision. The detailed analysis presented here provides the foundation for a series of more powerful measurements which will be made over the next decade as more luminosity is acquired.

Chapter 2

Theory

2.1 Introduction

Within the Standard Model the photon is the mediator of the electromagnetic interaction and the $W^{\pm}$ and Z° intermediate vector bosons are the mediators of the weak force. Because the electromagnetic and weak forces are unified within the Standard Model [2], the gauge bosons (photons, W's and Z's) can interact with each other. In the Standard Model there are no three photon or three Z boson verticies. The $WW\gamma$ vertex is required in the Standard Model by the gauge structure of the theory. The observation of the $WW\gamma$ coupling is thus an important test of the Standard Model. This coupling can also be used to probe the structure of the W boson.

2.2 The $WW\gamma$ process

The tree level Feynman diagrams for $W\gamma$ production are shown in figure 2.1. Diagrams 2.1.c show the s-channel tri-linear gauge couplings of the $WW\gamma$ vertex. The Feynman diagrams in figures 2.1.a and 2.1.b describe the u and t channel processes associated with initial state radiation off the incoming quark /anti-quark lines. Diagram 2.1.d describes the final state inner bremsstrahlung radiation off the decay electron. Because of the finite width of the W boson, all of these diagrams must be included in the calculation of the $W + \gamma$ cross section in order to preserve electromagnetic gauge invariance [17].

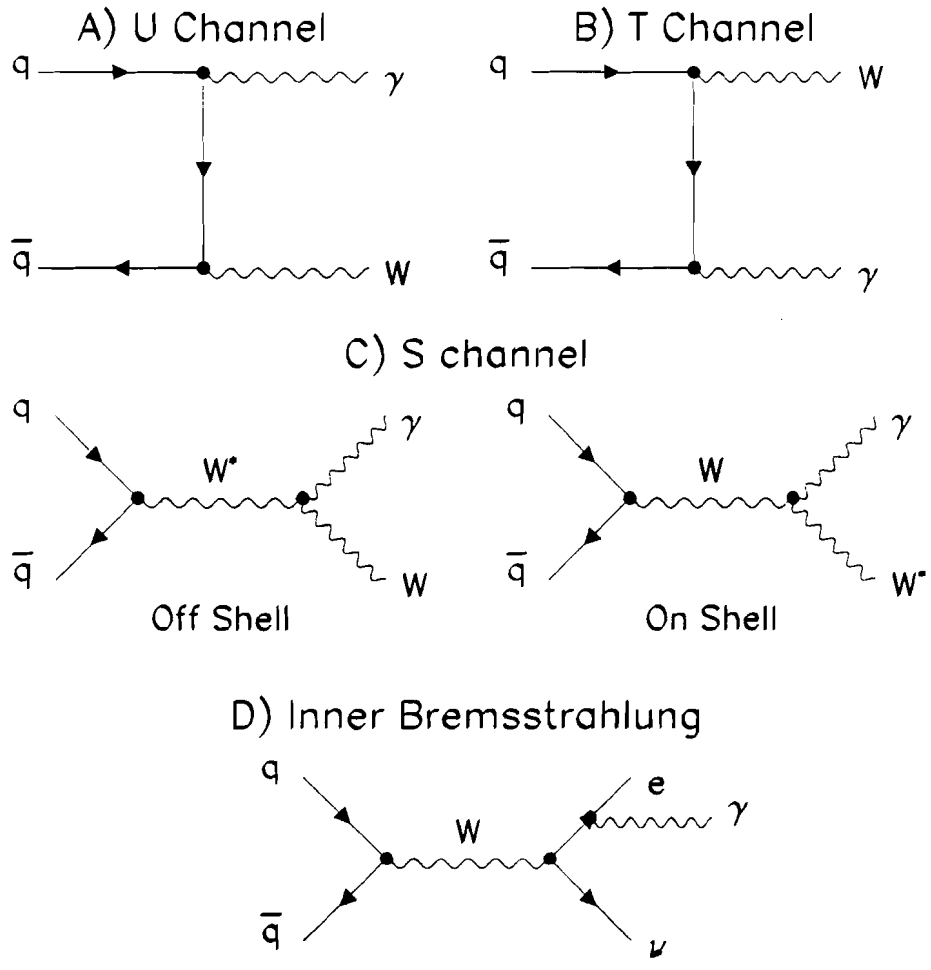

Figure 2.1: Tree-level $W + \gamma$ Feynman diagrams. (A) $u-$channel $W + \gamma$ initial-state bremsstrahlung diagram. (B) $t-$channel $W + \gamma$ initial-state bremsstrahlung diagram. (C) $s-$channel off-shell $W^* \rightarrow W + \gamma$ diagram. and $s-$channel on-shell $W \rightarrow W^* + \gamma$ diagram. (D) final-state inner bremsstrahlung diagram.

The subprocesses described in diagrams 2.1a-d occupy different regions of kinematic space. The initial state radiation is sharply peaked in angle along the incident quark/anti-quark direction. The photons from final state radiation tend to be collinear with the electron from $W \rightarrow e\nu$. The E_T spectra of photons from both initial and final state radiation are sharply peaked at low photon energy as in the case of radiation from the $WW\gamma$ vertex (2.1.d). The photons from $WW\gamma$ vertex are not strongly correlated with the decay lepton and are not bounded by the mass of the W boson.

The most general effective Lagrangian for anomalous $WW\gamma$ coupling for the tree-level processes shown in figures 2.1a-e is given by [18, 19]

$$\begin{aligned}
\mathcal{L}_{WW\gamma} \;=\; & -e\Big[ig_1\left(W^\dagger_{\mu\nu}W^\mu A^\nu - W^\dagger_\mu A_\nu W^{\mu\nu}\right) \\
& +\kappa_f W^\dagger_\mu W_\nu F^{\mu\nu} + \frac{\lambda_f}{M_W^2} W^\dagger_{\lambda\mu} W^\mu_\nu F^{\nu\lambda} \\
& -g_4 W^\dagger_\mu W_\nu \left(\partial^\mu A^\nu + \partial^\nu A^\mu\right) \\
& +g_5 \epsilon^{\mu\nu\rho\sigma}\left(W^\dagger_\mu \overleftrightarrow{\partial}_\rho W_\nu\right) A_\sigma \\
& +\tilde{\kappa}_f W^\dagger_\mu W_\nu \tilde{F}^{\mu\nu} + \frac{\tilde{\lambda}_f}{M_W^2} W^\dagger_{\lambda\mu} W^\mu_\nu \tilde{F}^{\nu\lambda}\Big]
\end{aligned} \tag{2.1}$$

where $A^\mu = (A^{\mu\dagger})$ and W^μ are the photon and W^- fields, respectively, and $W_{\mu\nu} = \partial_\mu W_\nu - \partial_\nu W_\mu$, $F_{\mu\nu} = \partial_\mu A_\nu - \partial_\nu A_\mu$, $\tilde{F}_{\mu\nu} = \frac{1}{2}\epsilon_{\mu\nu\rho\sigma}F^{\rho\sigma}$, $\left(A\overleftrightarrow{\partial}_\mu B\right) = A(\partial_\mu B) - (\partial_\mu A)B$, e is the charge of the proton, and M_W is the W mass. The terms g_1, g_4, g_5, κ_f, λ_f, $\tilde{\kappa}_f$ and $\tilde{\lambda}_f$ are momentum dependent couplings between the photon and W fields. The photon is taken to be on-shell and both the virtual and on-shell W couple to essentially massless fermions allowing $\partial_\mu W^\mu = 0$.

In the Lorentz gauge, $\partial_\mu A^\mu = 0$, $\partial_\mu W^\mu = 0$, the structure of the interaction is completely described by the above seven operators.

From angular momentum conservation only seven operators are needed. Only seven ($+-$, $-+$, $+0$, $0+$, -0, $0-$ and 00) of the nine possible helicity states of the W boson pair can be reached by s-channel vector boson exchange ($J = 1$ channel).

The other two helicity combinations ($++$ and $--$) have both W spins in the same direction and therefore have angular momentum $J \geq 2$. [19]

The renormalizability of the Standard Model provides a constraint on the form of the Lagrangian (2.1) and the form of the couplings. The Lagrangian (2.1) contains five operators of dimension four and two operators of dimension six. In order to maintain the renormalizability of the Standard Model the dimension of the couplings needs to be less than or equal to zero. The action ($S = \int d^4x\, \mathcal{L}$) is always dimensionless; thus, the Lagrangian density must have dimension equal to four. The couplings of the terms with operators of dimension equal to four are dimensionless. The presence of M_W^{-2} factors and operators of dimension equal to six in the other two terms of the Lagrangian (2.1) forces the couplings in those terms to be of dimension equal to zero for renormalizability to be maintained.

The terms g_4 and g_5 must vanish if the effective Lagrangian is to be gauge invariant for the photon [19, 18]. The value of the coupling g_1 is equal to one because of the minimal coupling of the photon to the $W^{\pm}$ fields, and is completely fixed by the charge of the W boson for the on-shell photons [18, 15].

Thus, the most general effective Lagrangian for anomalous $WW\gamma$ coupling compatible with the Lorentz structure of the Standard Model is

$$\begin{aligned} \mathcal{L}_{WW\gamma} \;=\; & -ie\Big[\Big(W^{\dagger}_{\mu\nu}W^{\mu}A^{\nu} - W^{\dagger}_{\mu}A_{\nu}W^{\mu\nu}\Big) \\ & +\kappa_f W^{\dagger}_{\mu}W_{\nu}F^{\mu\nu} + \frac{\lambda_f}{M_W^2}W^{\dagger}_{\lambda\mu}W^{\mu}_{\nu}F^{\nu\lambda} \\ & +\tilde{\kappa}_f W^{\dagger}_{\mu}W_{\nu}\tilde{F}^{\mu\nu} + \frac{\tilde{\lambda}_f}{M_W^2}W^{\dagger}_{\lambda\mu}W^{\mu}_{\nu}\tilde{F}^{\nu\lambda}\Big] \end{aligned} \tag{2.2}$$

where e is the charge of the proton, and M_W is the W mass.

The nature of the $WW\gamma$ process can be exploited to determine the form of the couplings (κ_f, λ_f, $\tilde{\kappa}_f$, $\tilde{\lambda}_f$). Tree-level unitarity of the process $e^+e^- \rightarrow W^+W^-$ restricts the $WW\gamma$ couplings to their Standard Model (gauge theory) values at asymptotically high energies [15, 16]. Because the effective Lagrangian in equation 2.2 describes both W^+W^- production via γ exchange and $W^{\pm}\gamma$ production via W

exchange, both processes $\gamma \rightarrow W^+W^-$ and $W^\pm \rightarrow W^\pm\gamma$ can be used to describe the couplings, κ_f, λ_f, $\tilde{\kappa}_f$ and $\tilde{\lambda}_f$. Any large deviation of the tree-level (Born level) couplings from their Standard Model values ($\kappa_f^{SM} = 1$, $\lambda_f^{SM} = 0$, $\tilde{\kappa}_f^{SM} = 0$, $\tilde{\lambda}_f^{SM} = 0$) must have the functional form $a_f(\hat{s}, q_W^2, q_\gamma^2)$ where a_f is any of the couplings $\Delta\kappa_f (= \kappa_f - 1)$, λ_f, $\Delta\tilde{\kappa}_f (\tilde{\kappa}_f - 1)$ or $\tilde{\lambda}_f$. This implies that the couplings vanish when the $W\gamma$ invariant mass $\sqrt{\hat{s}}$ or the square of the final state photon q_γ^2 or W boson four momentum $\bar{q}_W^2$ becomes large. The generalized dipole form factors a_f are assumed to be of the form [15]

$$a_f(P^2 = \hat{s},\, \bar{q}^2 = M_W^2,\, q^2 = 0) = \frac{a_o}{(1 + \frac{\hat{s}}{\Lambda^2})^n}, \tag{2.3}$$

where a_o is the dimensionless anomalous parameter $\Delta\kappa(= \kappa - 1)$, λ, $\tilde{\kappa}$, $\tilde{\lambda}$. The form factor scale Λ represents the scale at which new physics becomes important in the weak boson sector due to compositeness of the W boson. In the high energy limit ($\sqrt{\hat{s}} \gg M_W$) the terms in the $W\gamma$ production amplitude proportional to κ_f and $\tilde{\kappa}_f$ grow like $\sqrt{\hat{s}}/M_W$; while terms proportional to λ_f and $\tilde{\lambda}_f$ grow like $\hat{s}/M_W^2$ [15]. For unitarity to be maintained at the high energy limit in $q\bar{q} \rightarrow W\gamma$, the exponent n in equation (2.3) must be greater than one half for the anomalous parameters κ_f and $\tilde{\kappa}_f$, and for λ_f and $\tilde{\lambda}_f$ the exponent in equation (2.3) must be greater than one [15]. If the exponent n in equation (2.3) is sufficiently above the minimum value needed for unitarity to be maintained at high energies ($n > 1/2$ for κ_f and $\tilde{\kappa}_f$; $n > 1$ for λ_f and $\tilde{\lambda}_f$), then $W\gamma$ production is suppressed at energies $\sqrt{\hat{s}} \gg \Lambda \gg M_W$. At these energies multiple weak boson or resonance phenomena are expected to dominate [17]. The choice of $n = 2$ in equation (2.3) guarantees unitarity at high energies and will suppress $W\gamma$ production at energies, $\sqrt{\hat{s}} \gg \Lambda \gg M_W$ [15]. This choice of exponent also guarantees that the form factors stay *constant* for $\hat{s} \ll \Lambda^2$ and start to decrease only when the scale Λ is reached or surpassed, which is similar to the well known nucleon form factors. In the Standard Model at tree-level the dimensionless anomalous parameters have the values $\kappa = 1$, $\lambda = 0$, $\tilde{\kappa} = 0$, $\tilde{\lambda} = 0$.

Table 2.1: Properties of anomalous $WW\gamma$ couplings under discrete symmetries $\mathcal{C}$, $\mathcal{P}$,$\mathcal{T}$ and $\mathcal{CP}$

	κ_f	λ_f	$\tilde{\kappa}_f$	$\tilde{\lambda}_f$
$\mathcal{C}$	+	+	+	+
$\mathcal{P}$	+	+	−	−
$\mathcal{T}$	+	+	−	−
$\mathcal{CP}$	+	+	−	−

The couplings κ_f and λ_f are $\mathcal{CP}$ conserving while $\tilde{\kappa_f}$ and $\tilde{\lambda}_f$ are $\mathcal{P}-$odd and violate $\mathcal{CP}$ (*i.e.* violate $\mathcal{T}$). Table 2.1 shows the behavior of the the couplings under discrete transformations. The symmetry properties of the couplings can be easily seen by using the following transformation properties of the fields, A^μ and W^μ:

$$\begin{aligned}
\mathcal{C}\, W_\mu\, \mathcal{C}^{-1} &= -W_\mu^\dagger \\
\mathcal{C}\, A_\mu\, \mathcal{C}^{-1} &= -A_\mu \\
\mathcal{P}\, B(\vec{x},t)_\mu\, \mathcal{P}^{-1} &= B^\mu(-\vec{x},t) \text{ where } B_\mu = A_\mu \text{ or } W_\mu \\
\mathcal{T}\, B(\vec{x},t)_\mu\, \mathcal{T}^{-1} &= B^\mu(\vec{x},-t)
\end{aligned} \tag{2.4}$$

on the effective Lagrangian (2.2).

The $\mathcal{CP}-$conserving parameters $(\kappa\,,\lambda)$ are expected to receive small non-zero contributions at the one loop level of order $\alpha_{em} = \frac{e^2}{2hc}$ [15, 17]. The current experimental upper limit on the electric dipole moment (EDM) of the neutron, $d_n < 12\times10^{-26}\ e-\text{cm}$ @ 95% CL [20], imposes severe restrictions on the $\mathcal{T}$ violating (*i.e.* $\mathcal{CP}$ violating) $WW\gamma$ anomalous couplings, $\tilde{\kappa}$ and $\tilde{\lambda}$ [15, 24]:

$$|\tilde{\kappa}|,\ |\tilde{\lambda}| < 10^{-3}. \tag{2.5}$$

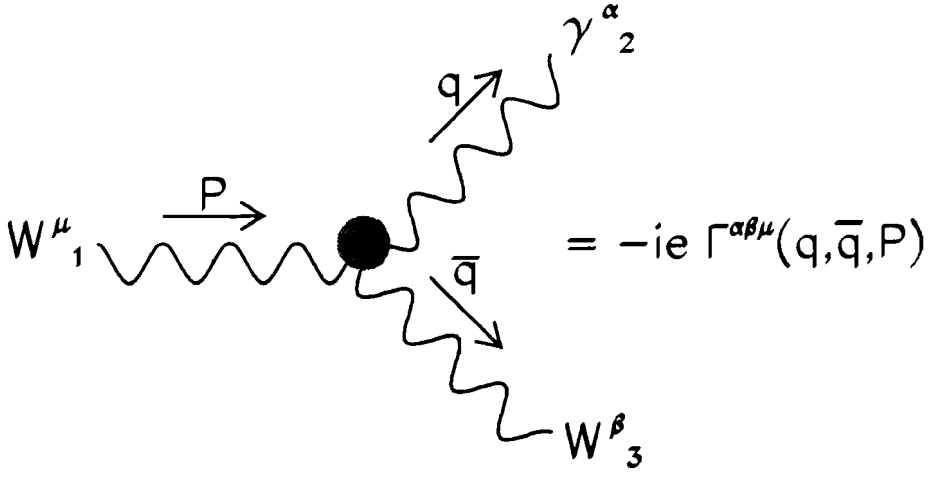

Figure 2.2: Feynman rule for the general $WW\gamma$ vertex. The vertex function Γ is given by equation 2.7.

Table 2.2: Form factors f_i to be used in the vertex function $\Gamma^{\alpha\beta\mu}$ for $\gamma \to W^+W^-$ and $(W^\pm)^* \to W^\pm\gamma$. From reference [18]

	$\gamma \to W^+W^-$	$(W^\pm)^* \to W^\pm\gamma$
f_1	$1 + \left(\frac{P^2}{M_W^2}\right)\lambda_f$	$\mp\frac{1}{2}\left(1 + \kappa_f + \frac{P^2}{M_W^2}\lambda_f\right)$
f_2	λ_f	$\mp\lambda_f$
f_3	$1 + \kappa_f + \lambda_f$	$\mp\frac{1}{2}(1 + \kappa_f + \lambda_f)$
f_4	0	$\pm\frac{i}{2}(1 + \kappa_f + \lambda_f)$
f_5	0	$\mp\frac{i}{2}(\tilde{\kappa}_f + \tilde{\lambda}_f)$
f_6	$\tilde{\kappa}_f - \tilde{\lambda}_f$	$\pm\frac{1}{2}(\tilde{\kappa}_f + \tilde{\lambda}_f)$
f_7	$-\frac{1}{2}\tilde{\lambda}_f$	$\pm\frac{1}{2}\tilde{\lambda}_f$

The function for the $WW\gamma$ vertex shown in figure 2.2 is given by [18]:

$$\begin{aligned}\Gamma^{\alpha\beta\mu}(q,\bar{q},P) &= f_1(q-\bar{q})^\mu g^{\alpha\beta} - \frac{f_2}{M_W^2}(q-\bar{q})^\mu P^\alpha P^\beta + f_3(P^\alpha g^{\mu\beta} - P^\beta g^{\mu\alpha}) \\ &\quad + if_4(P^\alpha g^{\mu\dot{\beta}} + P^\beta g^{\mu\alpha}) + if_5\epsilon^{\mu\alpha\beta\rho}(q-\bar{q})_\rho \\ &\quad - f_6\epsilon^{\mu\alpha\beta\rho}P_\rho - \frac{f_7}{M_W^2}(q-\bar{q})^\mu\epsilon^{\alpha\beta\rho\sigma}P_\rho(q-\bar{q})_\sigma \qquad (2.6)\end{aligned}$$

The momentum of the incoming W boson is denoted by P, the momentum of the outgoing W is $\bar{q}$, the photon momentum is q. The form factors f_i are Lorentz invariant dimensionless functions of q^2, $\bar{q}^2$ and P^2. The vertex function (2.6) can be used to describe the $\gamma \to W^+W^-$ process as well. Table 2.2 shows the relationship between the form factors f_i and the anomalous couplings in the effective Lagrangian (2.2) for W^+W^- production via γ exchange and for $W^\pm\gamma$ production via W exchange.

The gauge structure of the $W\gamma$ process produces an interesting effect in the $W\gamma$ center of mass. At large photon scattering angles θ^* (where θ^* is defined as the

angle between the photon and the incoming quark in the $W\gamma$ rest frame) the $u-$ and $t-$channel diagrams cancel the $s-$channel diagram, resulting in a radiation zero in the overall $W\gamma$ invariant amplitude, $\mathcal{M}_{W\gamma}$ [21]. The $W\gamma$ differential cross section $d\sigma/d\cos\theta^*$ will have a zero at $\cos\theta^* = \mp\frac{1}{3}$ for $W^{\pm}\gamma$ production. However, the radiation zero is expected to be at least partially filled in due to higher-order QCD corrections [22], finite W-width effects, background processes, event misreconstruction associated with the two-fold ambiguity of the longitudinal component of the neutrino momentum, as well as by possible non-gauge theory values of $\Delta\kappa$, λ, $\tilde{\kappa}$ and/or $\tilde{\lambda}$ [21]. For large-statistics samples, measurement of the *depth* of the dip in the differential cross section at $\cos\theta^* = \mp\frac{1}{3}$ and the *shape* of the $cos\theta^*$ distribution provides a sensitive measurement of the values of these anomalous parameters.

Another method for observing the radiation zero, which does not require reconstruction of the $W\gamma$ center-of-mass system and hence is not subject to smearing effects due to event mis-reconstruction is to study the photon$-$lepton pseudo-rapidity correlations in $W^{\pm}\gamma$ production [23]. $(\eta_\gamma - \eta_{\ell^\pm})$ In the SM, the $\Delta\eta_{\gamma\ell^\pm} = \eta_\gamma - \eta_{\ell^\pm}$ distribution ($\eta = -\ln(\tan\theta/2)$), exhibits a pronounced dip at $\Delta\eta_{\gamma\ell^\pm} \sim \mp\ 0.4$ for $W^{\pm}\gamma$ production. The dip in the $\Delta\eta_{\gamma\ell^\pm}$ distribution is a remnant of the radiation amplitude zero in the $\cos\theta^*$ angular distribution and corresponds to a "valley" in the three-dimensional "surface" associated with the $d^2\sigma/d\eta_\gamma d\eta_{\ell^\pm}$ distribution.

However, the use of either of these two methods is not feasible for small-statistics $W\gamma$ data samples. In this regime, the measurement of the absolute $W\gamma$ production cross section $\times$ decay branching ratio, or equivalently the integral number of isolated photons above a minimum photon E_T cut is also sensitive to anomalous $\Delta\kappa$ and λ values, and is the method used in this analysis. Figure 2.3 shows the variation of the total $p\bar{p} \rightarrow W^-\gamma X$ cross section versus the energy in the $p\bar{p}$ center of mass $\sqrt{S}$.

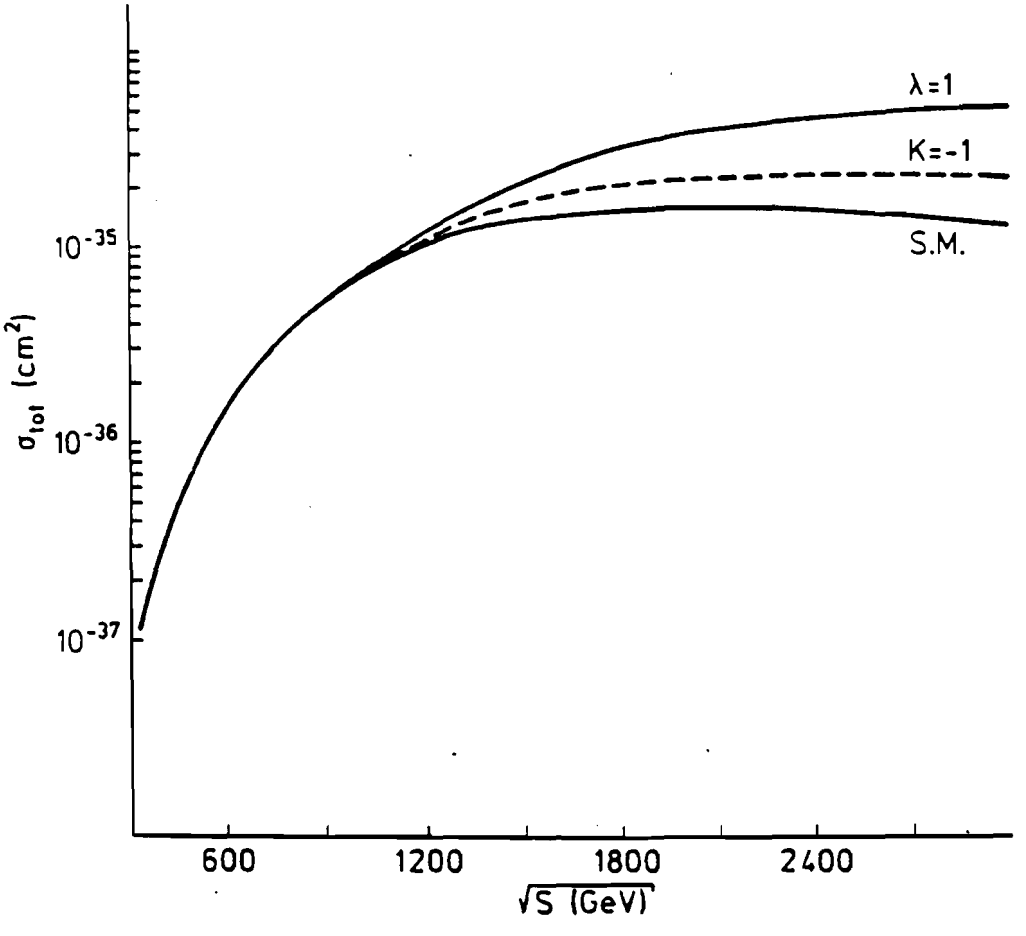

Figure 2.3: Total cross section for $p\bar{p} \to W^{-}\gamma X$ versus the energy in the $p\bar{p}$ center of mass energy. The $p\bar{p}$ center of mass energy $S^{1/2}$ at the Tevatron is 1800 GeV. The photon transverse energy is $E_T^{\gamma} > 10\,\mathrm{GeV}$. In the Standard Model at tree-level $\kappa = 1$, $\lambda = 0$, $\tilde{\kappa} = 0$, $\tilde{\lambda} = 0$.

2.3 Electromagnetic moments of the W boson.

The anomalous parameters are related to the W boson classical electromagnetic parameters in the static (photon energy $\rightarrow$ 0) limit (with $\hbar = c = 1$) via:

$$\mu_W = \frac{e}{2M_W}(2 + \Delta\kappa + \lambda) \quad \text{Magnetic Dipole Moment} \tag{2.7}$$

$$Q_W = -\frac{e}{M_W^2}(1 + \Delta\kappa - \lambda) \quad \text{Electric Quadrupole Moment} \tag{2.8}$$

$$d_W = \frac{e}{2M_W}(\tilde{\kappa} + \tilde{\lambda}) \quad \text{Electric Dipole Moment} \tag{2.9}$$

$$\tilde{Q}_W = -\frac{e}{M_W^2}(\tilde{\kappa} - \tilde{\lambda}) \quad \text{Magnetic Quadrupole Moment} \tag{2.10}$$

$$< R_W^2 > = \frac{1}{M_W^2}(1 + \Delta\kappa + \lambda) \quad \text{Mean} - \text{Squared Charge Radius} \tag{2.11}$$

Note that for an arbitrary spin-S particle, $2S + 1$ electromagnetic moments are allowed [25]. Thus, the W vector boson is expected to have *both* a magnetic dipole moment *and* an electric quadrupole moment in the Standard Model [26]. The W electric dipole and magnetic quadrupole moments (the terms in the effective Lagrangian involving the $\tilde{\kappa}$ and $\tilde{\lambda}$ parameters) are $\mathcal{P}-$odd and violate $\mathcal{CP}$ (i.e. violate $\mathcal{T}$).

The tree-level Standard Model predictions for the values of the anomalous parameters are $\Delta\kappa = \kappa - 1 = 0$, $\lambda = 0$, $\tilde{\kappa} = 0$, $\tilde{\lambda} = 0$. The numerical values expected for these Standard Model parameters are:

$$\mu_W^\circ = \frac{e\hbar c}{2M_W c^2} = 3.691 \pm 0.012 \times 10^{-16} \text{ MeV/T}$$

$$(\mu_e^\circ = \frac{e\hbar c}{2M_e c^2} = 5.788 \pm 0.000 \times 10^{-11} \text{ MeV/T})$$

$$Q_W^\circ = -e\left(\frac{\hbar c}{M_W c^2}\right)^2 = -e\,\lambda\!\!\!^{-2}_W = 6.063 \pm 0.041 \times 10^{-6} \text{ e fm}^2$$

$$\lambda\!\!\!^{-}_W = \frac{\hbar c}{M_W c^2} = 2.462 \pm 0.008 \times 10^{-3} \text{ fm}$$

Table 2.3: Comparison of Dirac magnetic moment of the proton and neutron with their observed values

	μ(Dirac)	μ(observed)
Proton	$\frac{e\hbar}{2M_{proton}c} = 1$ n.m.	+2.79 n.m.
Neutron	0	−1.91 n.m.

where $\lambda\!\!\!^{-}_W$ is the (reduced) Compton wavelength of the W boson. The Standard Model predicts a g factor for the W boson of $g_W = 2$. Note that the uncertainties on these quantities are due primarily to the uncertainty on the W boson mass, $M_W = 80.14 \pm 0.27$ GeV/c^2 (the combined CDF+UA2 result) [27, 28].

Anomalies in the electromagnetic moments of a particle can indicate some internal structure. For example, in the Dirac theory protons and neutrons are point-like particles with predicted magnetic moments summarized in table 2.3. The magnetic moments of the proton and neutron are anomalous indicating the compositeness of each particle. Thus, anomalies in the magnetic dipole moment and/or the electric quadrupole moment of the W boson would suggest the compositeness of the W boson. Additionally the electric quadrupole moment of the W boson is related to the Compton wavelength of the W boson by the relationship:

$$Q_W = -e \cdot \lambda\!\!\!^{-2}_W \cdot (1 + \Delta\kappa - \lambda) \tag{2.12}$$

Because the cross section of the $WW\gamma$ process, $\sigma(W + \gamma)$, is a function of the anomalous coupling parameters κ, λ, $\tilde{\kappa}$ and $\tilde{\lambda}$, experimental upper limits for these anomalous parameters can be derived from experimental $\sigma \cdot B(W(\rightarrow e\nu) + \gamma)$ measurement in the existing CDF $W \rightarrow e\nu$ data sample. The experimental upper limits on anomalous parameters ($\tilde{\kappa}$ and $\tilde{\lambda}$) derived from the experimental $\sigma \cdot B(W + \gamma)$ measurement of the existing data sample are within 10 % of those for $\delta\kappa$ and λ The experimental limits on the anomalous parameters, $\tilde{\kappa}$ and $\tilde{\lambda}$, will not be presented in

this analysis. The limits on the anomalous couplings κ and λ will be used with the aid of equations 2.7 and 2.8 to determine the magnetic dipole moment and electric quadrupole moment of the W boson.

Chapter 3

Experimental Apparatus

3.1 The Tevatron

The Tevatron is a superconducting synchrotron designed to store and collide bunches of protons and anti-protons. There are several smaller particle accelerators used to create the protons and anti-protons and accelerate them for injection into the Tevatron. Figure 3.1 shows the layout of the different accelerators at Fermi National Accelerator Laboratory (FNAL).

Prior to injection into the Tevatron, the protons must undergo many different stages of acceleration. The protons are created from hydrogen gas which is ionized and accelerated to 750 keV in a Cockroft-Walton electrostatic accelerator. A linear accelerator is used to increase the proton energy to 200 MeV. The protons are then accelerated to 8 GeV by the Booster Ring, a synchrotron located behind Wilson Hall at FNAL. The protons from the Booster Ring are injected into the Main Ring. The Main Ring (which is located in the same tunnel as the Tevatron) accelerates the protons up to 120 GeV; some of the protons are extracted from the Main Ring to be used for the creation of anti-protons.

The anti-protons are created by protons striking a tungsten target. The anti-protons are focused using a lithium electromagnet. The anti-protons are then sent to the Debuncher Ring where the spread in longitudinal momentum is reduced in order to increase their transfer efficiency into the anti-proton Accumulator. The anti-protons are stored in the Accumulator until there are enough in the "stack" to be transferred to the Main Ring. Both the protons and the anti-protons are

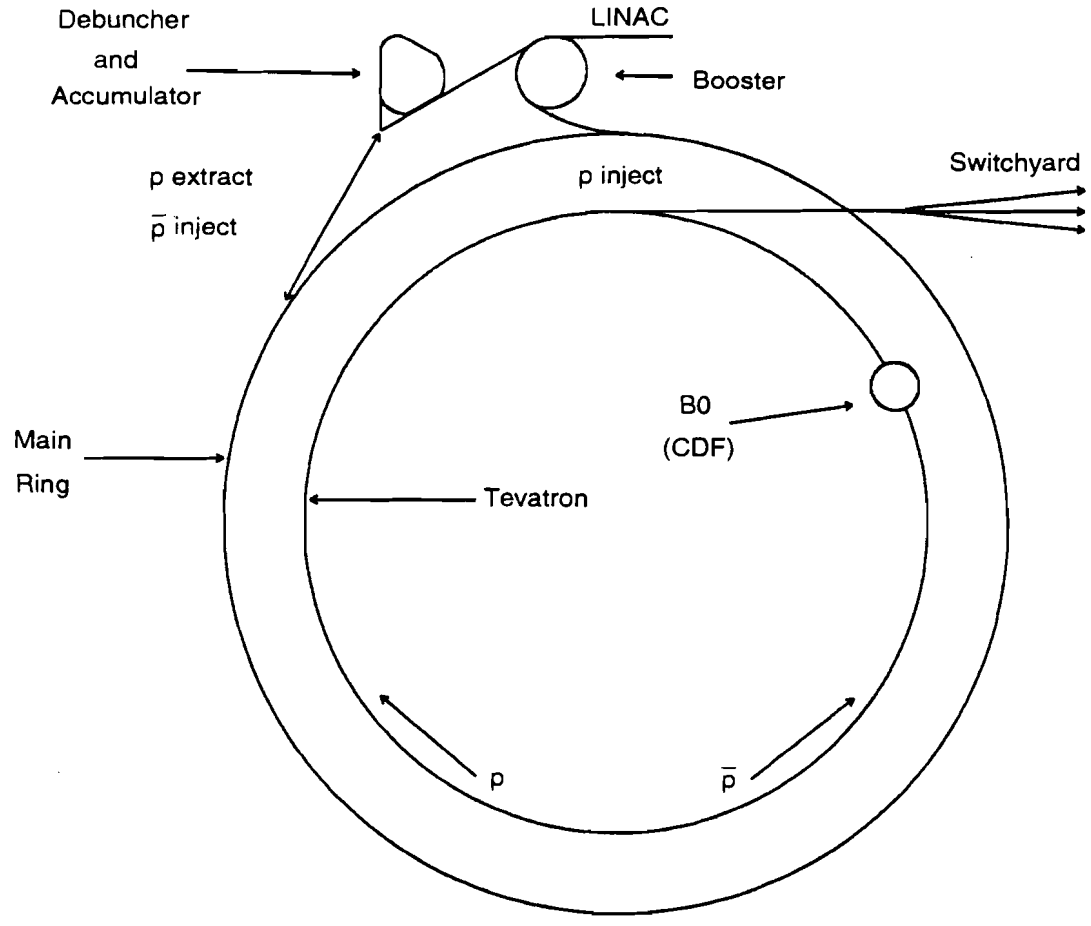

Figure 3.1: Overview of the different accelerators at the Fermi National Accelerator Laboratory (FNAL).

accelerated to 150 GeV by the Main Ring before being injected into the Tevatron in at present, six bunches. Once in the Tevatron the protons and anti-protons are accelerated to 900 GeV. Quadrupole magnets are used to focus the beams at the $B0$ collision point (CDF).

During the 1988-1989 Tevatron run, approximately 10^{11} anti-protons were required for a typical store. During a typical run six bunches of approximately $5-10 \times 10^{10}$ protons and six bunches of approximately $1-3 \times 10^{10}$ anti-protons were collided with a typical luminosity of $10^{30}\text{cm}^{-2}\,\text{sec}^{-1}$. The average store lasted 20 hours.

3.2 CDF DETECTOR

The Collider Detector at Fermilab (CDF) is a nearly hermetic general purpose detector designed to provide good lepton and jet identification originating from $p\bar{p}$ collisions at a center of mass energy of 1.8 TeV. The z axis in the CDF coordinate system was defined to be parallel to the beam line with the positive z axis pointing in the same direction as the proton beam system. The positive y axis was defined to be pointing up vertically and the positive x axis pointed away from the center of the Tevatron. The θ was defined as the polar angle with respect to the proton beam direction (positive z axis). The angle ϕ was defined as the azimuthal angle around the beam and $\phi = 0$ along the positive x axis. Another variable used to determine the location of a particle in the CDF detector was its pseudorapidity :

$$\eta = \frac{1}{2}\ln\left(\frac{1+\cos\theta}{1-\cos\theta}\right) \tag{3.1}$$

It was observed that in collisions at hadron colliders that the average particle density is roughly flat in $\frac{dn}{d\phi}$ over all angles ϕ and $\frac{dn}{dy}$ over some rapidity range $|y| < X$. The rapidity (y) palteau widens with increasing energy. [29] For a given

particle(s) the variable y , rapidity, is defined as:

$$y = \frac{1}{2}\ln\left(\frac{1+\beta\cos\theta}{1-\beta\cos\theta}\right)$$

where $\beta = v/c$ and θ is the polar angle. At high energies, $\beta \approx 1$, the pseudorapidity of a particle is approximately equal to its rapidity. Hence at high energies the average particle density is approximately flat in the experimentally measured quantity η.

Figures 3.2 and 3.3 show the layout and major subsystems of the CDF detector in its 1988-1989 configuration. The CDF detector is comprised of a 2000 ton movable cylinder whose axis lies along the Beam line. The Vertex Time Projection Chambers (VTPC) are closest to the nominal interaction point. Surrounding the VTPC is a wire drift chamber used for measuring tracks (CTC). Both of these devices are inside a 1.4 Tesla superconducting solenoidal magnet used for charge and momentum determination. Outside the magnet are electromagnetic and hadronic calorimeters. The calorimeters in the central region have an angular coverage in θ of $30° < \theta < 150°$. Surrounding the calorimeters in the central region of the CDF detector are the muon chambers. The end-caps of the central cylinder are filled with plug calorimeters which provide calorimetry coverage at angles shallower ($10° < \theta < 36°$ and $144° < \theta < 170°$) than the central calorimeters. In the forward regions of the collision hall are the 3000 ton forward calorimeters. These fixed calorimeters provide coverage at angles shallower ($2° < \theta < 10°$ and $170° < \theta < 178°$) than the plug or central calorimeters. Also in the forward direction are toroidal magnets and devices for muon detection. The analysis presented in this thesis makes use of the tracking and calorimeter subsystems.

3.2.1 Tracking Detectors

Closest to the beam pipe the Vertex Time Projection Chamber (VTPC) was designed to track charged particles in the $r-z$ plane (r is the radial distance from the beam). It was used to find the location of the primary interaction point (vertex) along the

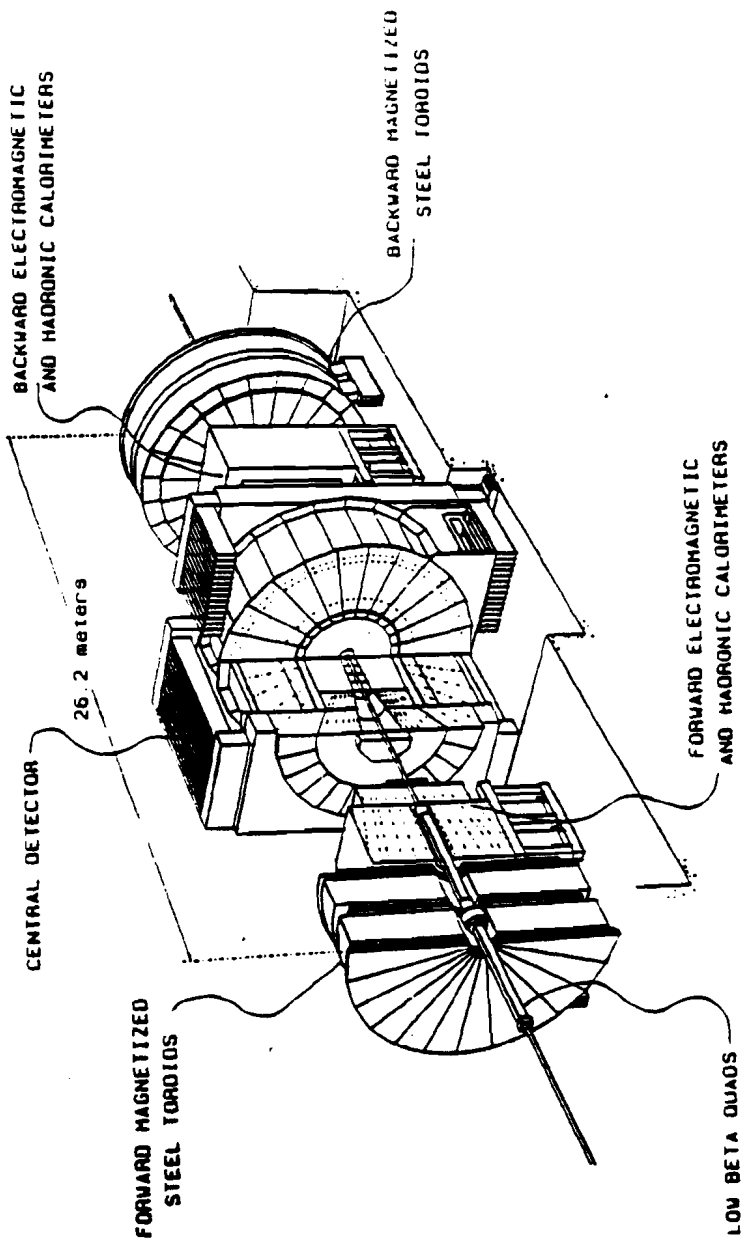

Figure 3.2: Perspective view of CDF showing both the forward and central components of the detector.

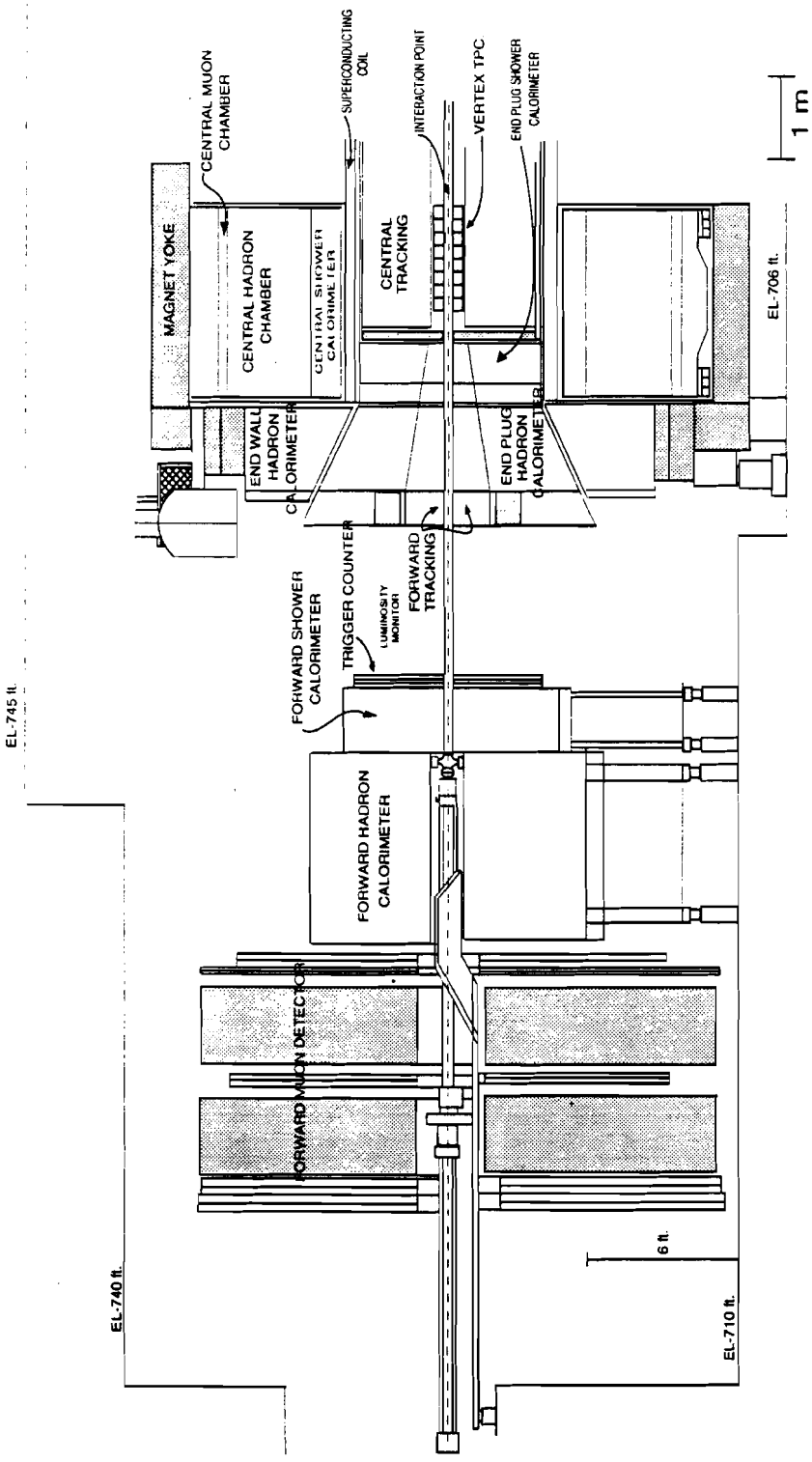

Figure 3.3: Cut away view of one half the CDF detector.

z axis.

The VTPC consisted of a set of eight individual time projection chambers each subdivided azimuthally into octants (figure 3.2.1). Particles passing through the chambers ionized the gas (50% argon 50% ethane) within the chambers; the resulting electrons drifted toward anode wires and cathode pads for subsequent readout. The radial and beam-line location of each wire together with the drift time of the charge to the wire allowed the reconstruction of tracks in the $r - z$ plane.

Reconstructed tracks in the VTPC were parameterized by the polar angle and the intercept with the z axis. Primary vertices were located by identifying clusters of z intercepts from several tracks. The z resolution of the VTPC was approximately 2 mm. Figure 3.5 shows the distribution of primary vertices in the 2662 candidate W events in the inclusive electron W sample.

The Central Tracking Chamber (CTC) was a large 1.3 meter radius cylindrical drift chamber surrounding the VTPC. Like the VTPC, the CTC was inside of the 1.4 Tesla superconducting solenoidal magnet. The CTC provides charged particle tracking in three dimensions (Figure 3.2.1).

The CTC covered the region $|\eta| < 1.0$ at its outer radius and was cylindrically symmetric, allowing full azimuthal coverage. The CTC included both axial and stereo wires. Because of the magnetic field, charged particles moved in helical trajectories. The sense wires of the CTC were grouped into nine super-layers and within each super-layer the wires were further grouped. The sense wires of the five axial super-layers were parallel to the z axis. The remaining four stereo super-layers consisted of wires with a 3° tilt to provide z information. The axial and stereo super-layers alternated with an axial super-layer being the inner most super-layer.

Each cell within a super-layer consisted of field, sense, potential, guard and shaper wires. The field wires provided an electrostatic potential of approximately 1350 V/cm. The charged particles ionized the 50-50 argon/ethane gas and the electrostatic and magnetic fields caused the charge to drift towards the sense wires.

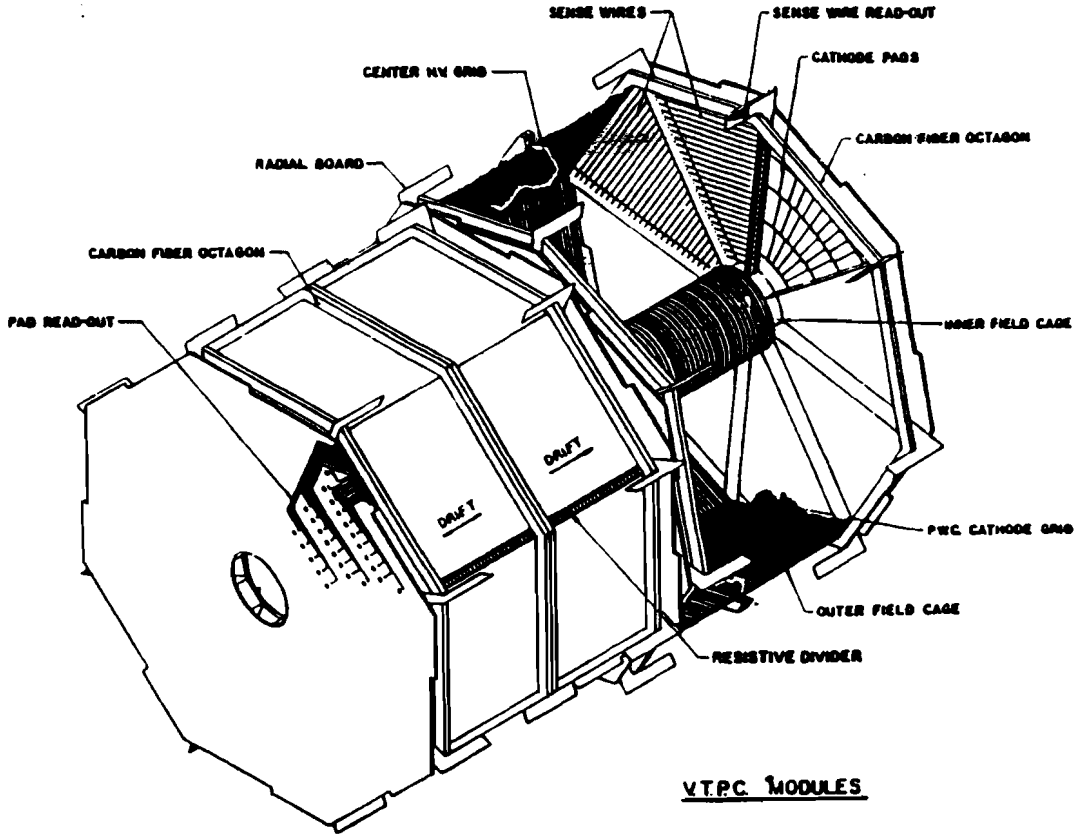

Figure 3.4: Isometric view of two VTPC modules.

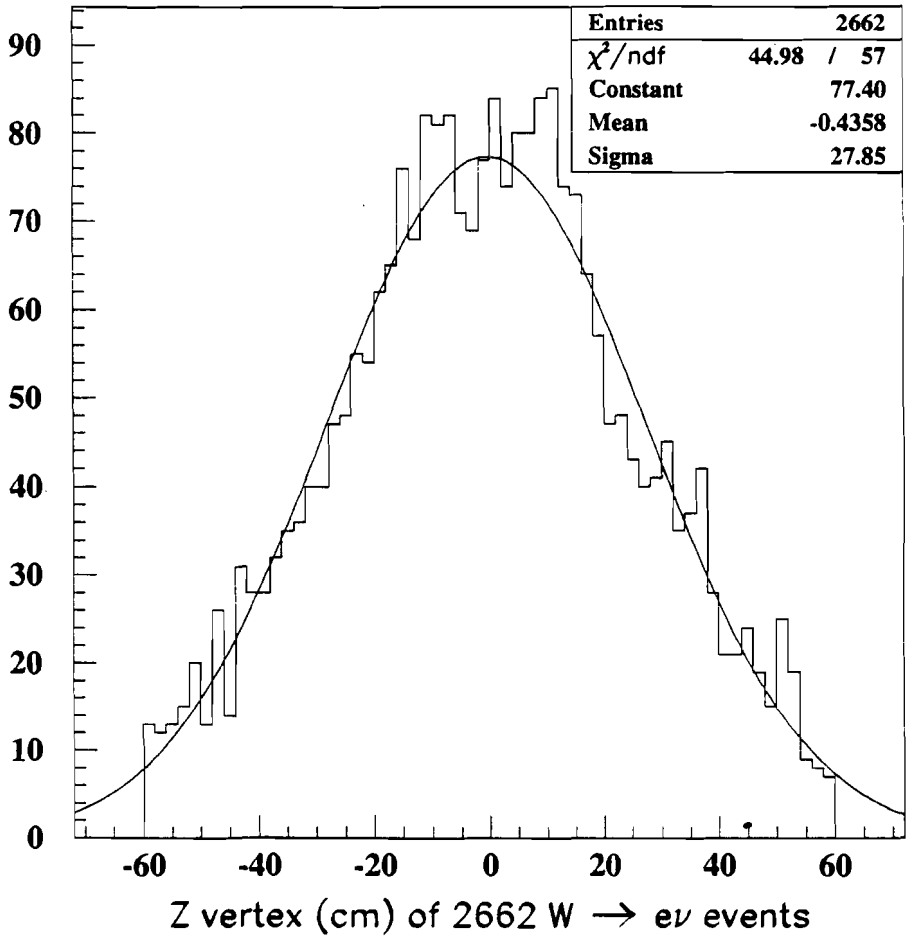

Figure 3.5: Z vertex of inclusive electron W events.

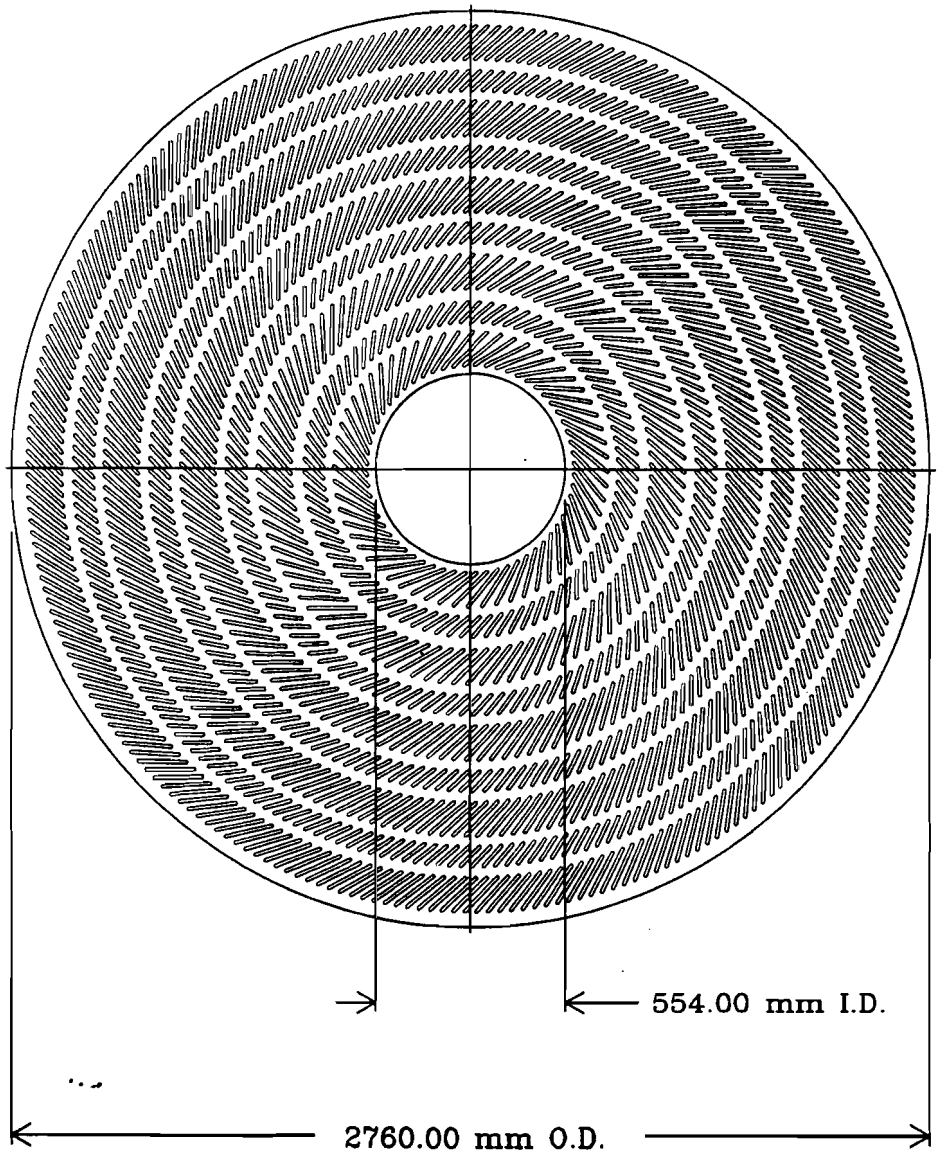

Figure 3.6: Cross sectional view of the CTC end-plate showing both the axial and stereo wire locations.

In the region of the sense wires the gain of the gas was controlled by the potential wires. The electric field was "fine tuned" through the use of guard and shaper wires.

All wire cells were inclined at a 45° angle (see figure 3.2.1) relative to the radial direction from the beam axis to compensate for the subtleties of drifting charge. In magnetic and electrostatic fields, the drift velocity of charged particles is both parallel to the electrostatic field and parallel to $\vec{E} \times \vec{B}$ [30]. The net drift velocity forms an angle relative to the electrostatic field given by [31]:

$$\tan\beta = \frac{v \cdot B}{k \cdot E}, \tag{3.2}$$

where β is the Lorentz angle, v is the drift velocity with no magnetic field, B is the magnetic field strength and k is a parameter that depends on the particular gas being used in the drift chamber. For the CTC k was approximately 0.7 resulting in a Lorentz angle $\beta \approx 45°$. The 45° tilt was decided to allow the drift trajectories to be approximately azimuthal. This simplified the track reconstruction ensuring that the maximum drift time to the nearest wire in a given super-layer was 40 nsec. Multiple rows within a super-layer were used to resolve the left-right drift time ambiguity and for redundancy in the case of wire failure. The sense wire positions were used for the measurement of the radial position r of a track. The drift time was used to determine the ϕ position. Since the axial magnetic field bent the charged particles in the axial direction (ϕ) and did not alter the z trajectory, the curvature of the track was used to determine the sign of the particle's charge and its momentum. The RMS momentum resolution of the CTC was $\delta P_T/P_T = P_T/500\,\mathrm{GeV/c}$ (P_T is in GeV/c) for isolated tracks. Imposing the constraint that individual tracks originate from the interaction point (vertex), extended the effective track fitting range from 1.0 m to 1.3 m, thus improving the momentum resolution to $\delta P_T/P_T = P_T/900\,\mathrm{GeV/c}$. In this analysis the CTC was used to identify electrons from the decay of the W boson and to veto events with charged particles pointing at the electromagnetic cluster associated with a photon. The CTC was also used to veto events that failed a tracking isolation cut (in order to reduce the QCD-jet background).

3.2.2 Central Calorimeters

The CDF calorimeters are finely segmented in the $\eta - \phi$ directions and are organized into projective towers pointing towards the interaction point. The calorimeters covered all of phi and extended to $|\eta| < 4.2$. Each calorimeter tower consisted of an electromagnetic calorimeter element in front of a hadronic calorimeter element. In the central region the calorimeters have an angular coverage (in η) of $|\eta| < 1.1$. The calorimeters in the plug have coverage of $1.1 < |\eta| < 2.4$. The forward calorimeters cover $2.4 < |\eta| < 4.2$.

The central electromagnetic calorimeters (CEM) contained 31 layers of polystyrene scintillator interspersed with lead sheets into towers of dimensions (in η - ϕ space) of 0.11 in η by 15° in ϕ. The CEM was 18 radiation lengths (0.6 absorption lengths) thick and had a pseudo-rapidity coverage of $0 < |\eta| < 1.1$. Each calorimeter tower was read out through wavelength shifters coupled via light guides to two conventional photo-multiplier tubes (one on each phi edge of the tower). This redundancy protected against failures due to a single faulty photo-multiplier tube. Since each photo-multiplier tube read out light at the phi edge of the calorimeter tower, the phi position of an electromagnetic shower could be determined using both of the photo-multiplier tubes. Figure 3.7 shows a schematic view of a central calorimeter wedge and the placement of the photo-multiplier tubes.

Embedded approximately six radiation lengths deep in the lead-scintillator sandwich of the CEM was a electromagnetic shower maximum detector. This detector called the Central Electromagnetic Strip chambers (CES) was a multi-wire proportional chamber with finer segmentation than the CEM. This finer segmentation allowed for excellent measurement of electromagnetic shower profiles in both z through the cathode pads and $r - \phi$ through anode wires. Figure 3.8 shows a schematic drawing of the CES. The CES cathode pads (aligned along the z direction) varied in width from 1.67 cm to 2.01 cm. The anode wires (oriented along $r - \phi$ (x) direction (r is the radial distance from the beam line)) were spaced 1.45 cm apart. The position

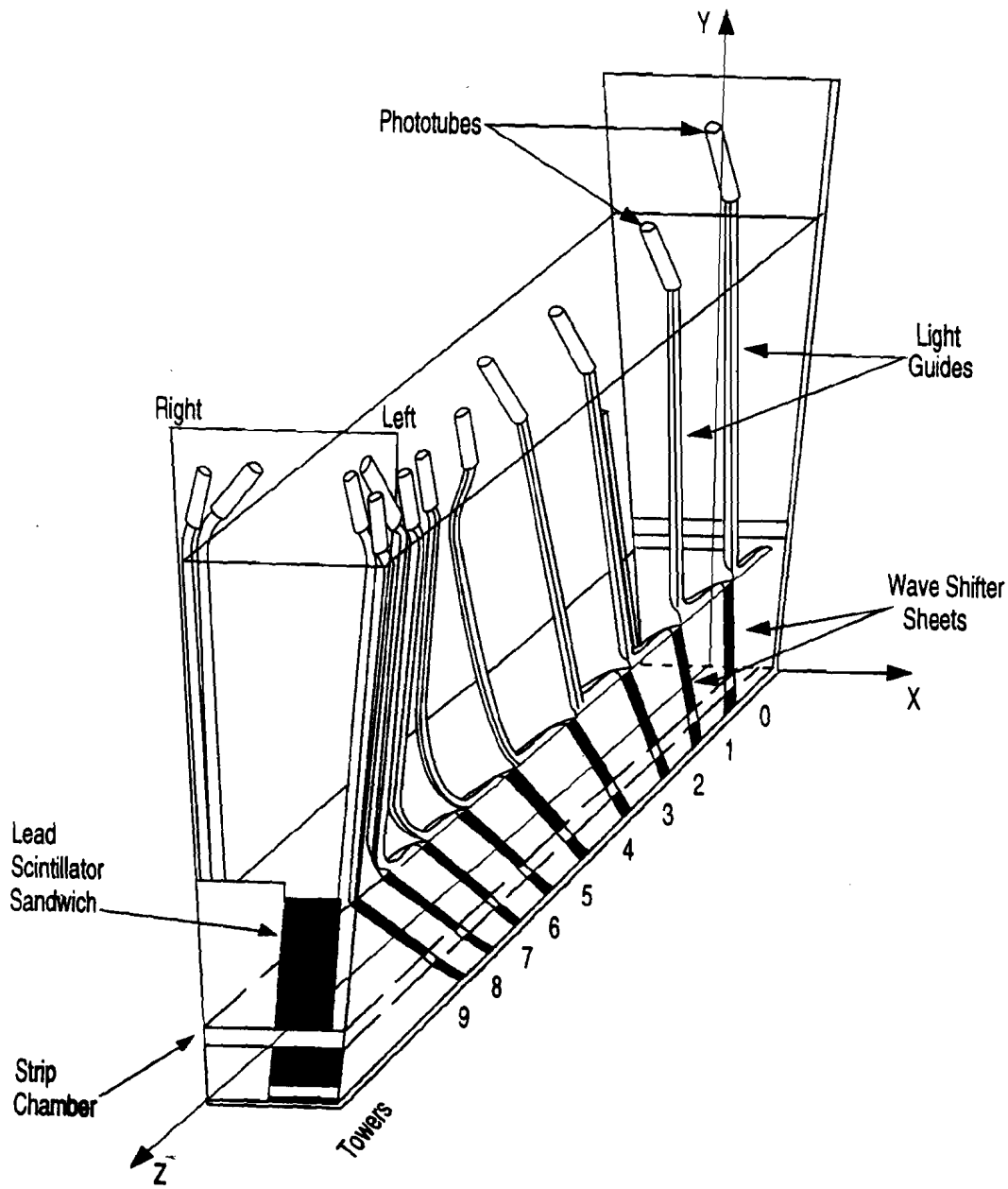

Figure 3.7: Schematic of Central Calorimeter and location of CES.

resolution in each view was 0.2 cm.

Located behind the CEM in the same tower configuration, the Central Hadronic Calorimeter (CHA) consisted of 32 layers of steel absorber interspersed with acrylic scintillator, totaling 4.5 absorption lengths. Also located behind the CEM, the End-wall Hadron Calorimeter (WHA) consisted of 15 layers of steel absorber interspersed with acrylic scintillator (each layer had double the thickness of the CHA) totaling 4.5 absorption lengths. The pseudo-rapidity coverage for the CHA was $0.0 < |\eta| < 0.9$ and for the WHA the corresponding coverage was $0.7 < |\eta| < 1.3$. The WHA completed the hadron calorimeters coverage for the interface region between the central and plug calorimeters.

The CEM,CHA and WHA were calibrated with test-beam electrons and pions at various energies using a sample wedge. The CEM had an energy resolution of $\delta E/E = 13.5\%/\sqrt{E} + 2.0\%$ where E is in GeV. Both the CHA and WHA had energy resolutions of $\delta E/E = 75\%/\sqrt{E} + 3.0\%$ where E is in GeV.

In the analysis the central calorimeters were used to identify electrons by the energy deposition (nearly entirely in the electromagnetic portion of the calorimeter) of an incident track. These calorimeters were also used to identify photons by their energy deposition in the CEM when no track was present. The EM shower maximum detector (CES) was crucial to this analysis and was used to determine the position and the transverse development of an electromagnetic shower at shower maximum.

3.2.3 Plug and Forward Calorimeters

The plug and forward calorimeter components were gas proportional wire chambers that were filled with 50/50 Argon/Ethane. These calorimeters had the projective geometry like the CEM,CHA and WHA calorimeters and had finer segmentation than the central calorimeters (CEM,CHA and WHA) of 0.09 in η and 5° in ϕ. The actual chamber stacks form a quadrant on one side of the plug electromagnetic calorimeter (PEM), forward electromagnetic (FEM) and hadronic (FHA) calorimeters and a 30°

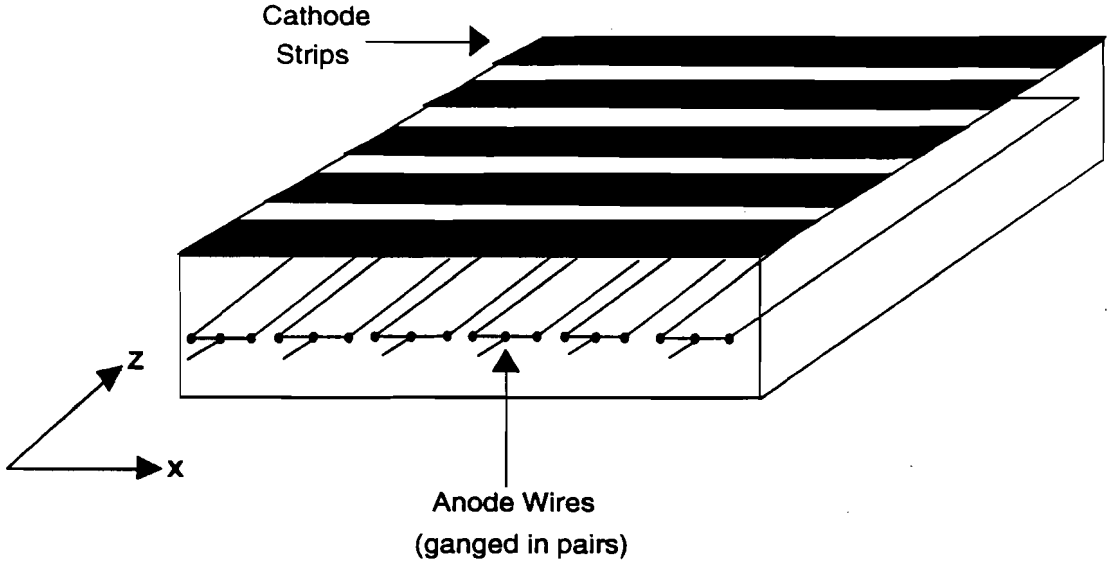

Figure 3.8: Schematic for the CES detector.

slice in plug hadronic calorimeters (PHA). The plug calorimeters (PEM,PHA) fill in the end-caps on either side of the central barrel (see figure 3.3). The PEM consisted of four 90° quadrants. Each quadrant had 34 layers of wire chambers interspersed with thin sheets of lead absorber. The PEM had a pseudo-rapidity coverage of $1.1 < |\eta| < 2.4$; a position resolution of 2 mm $\times$ 2 mm and is $18 - 21$ radiation lengths thick depending on position within the PEM. The PHA had $12 - 30°$ (in ϕ) sections. Each section contained 20 layers of wire chambers sandwiched between 21 layers of steel. The PHA was 5.7 absorption lengths thick and had a pseudo-rapidity coverage of $1.3 < |\eta| < 2.4$.

The forward calorimeters were not located on the movable cylindrical section of the CDF detector,but instead were in fixed positions at larger pseudo-rapidities than the central or plug calorimeters. The FEM was divided into four quadrants each containing 30 layers of proportional wire chambers and lead sheets. The FEM was 25 radiation lengths thick and had a pseudo-rapidity range of $2.2 < |\eta| < 4.2$. Similar to the FEM the FHA was divided into quadrants; each quadrant had 27 layers of proportional wire chambers and steel absorbers. The FHA was 7.7 absorption lengths thick and had a pseudo-rapidity coverage of $2.3 < |\eta| < 4.2$.

The energy resolution was larger for the gas calorimeters (plug or forward) than it was for the scintillator based calorimeters in the central region. The PEM had energy resolutions of $\delta E/E = 28\%/\sqrt{E} + 2\%$ where E is in GeV. For the FEM the energy resolution was $\delta E/E = 25\%/\sqrt{E} + 2\%$. The PHA had an energy resolution of $\delta E/E = 90\%/\sqrt{E} + 4\%$ and in the FHA $\delta E/E = 130\%/\sqrt{E} + 4\%$.

In this analysis the plug and forward calorimeters were used in the determination of the missing transverse energy $\not\!\!E_T$ (see chapter 4 for definition).

3.3 Luminosity Monitors

The beam-beam counters (BBC) were a plane of scintillation counters immediately in front of the forward/backward calorimeters at a distance of 5.8 m from the nominal interaction point and covering the beam fragmentation region in pseudo-rapidity range $3.2 < |\eta| < 5.9$ These counters provided a minimum bias trigger for the detector and were also used as the primary luminosity monitor for CDF. The minimum-bias BBC trigger required at least one counter in each plane to fire within a 15 ns time window centered on the beam crossing time.

3.4 Triggering

The interaction rate during the 1988-1989 collider run was 10^5 times higher than the capacity of the CDF data acquisition system. In order to select interesting events to process and maximize the amount of time that the CDF detector could take data (i.e. reduce the dead-time), CDF used a four level trigger system. A description of the triggers relevant to the collection of inclusive electron W data follows.

The lowest level trigger selected inelastic (minimum-bias) $p\bar{p}$ collisions by requiring an in-time coincidence of the BBC planes on either side of the interaction region. The trigger decision was available in time to inhibit data taking during the next beam crossing 3.5 μsec later.

The level-1 trigger decision was made within 7.0 μsec as allowed by level-0. If an event failed in the level-1, the front end electronics were reset in time for a second beam crossing after the initial level-0 decision. The maximum allowed level-1 accept rate was 1 kHz. The level-1 calorimeter trigger system computed transverse energy in both the electromagnetic and hadron compartments of the calorimeter. Trigger towers had a width of $0.2 \times 15^\circ$ in $\eta \times \phi$, mapping the detector into two 42×24 $(\eta \times \phi)$ arrays, one for electromagnetic and the other for hadronic energy deposition. Central electron W candidates were required to have at least 6 GeV in a single trigger tower

(= two physical towers) of the central electromagnetic calorimeter.

In level-2, two-dimensional tracking information from the central fast tracker [32] (CFT), a hardware track processor, was associated with level-1 electron information to form level-2 electron triggers. Fast timing information from the CTC was used to detect high transverse momentum tracks in the central region. The track finder analyzed prompt hits from the axial sense wires of the CTC to identify tracks by comparing hits in the CTC to predetermined hit patterns for the range of transverse momenta allowed by the CFT trigger threshold. The CFT relied upon the fact that stiff tracks have ionization drift times of less than 40 *nsec* for at least one wire in each super-layer of the CTC to determine track momentum. The track processor covered the P_T range from 2.5 to 15 GeV/c with a momentum resolution of $\delta P_T/P_T = 3.5\%$ (P_T in GeV/c). The list of two-dimensional tracks found was presented to the rest of the CDF level-2 trigger system.

The level-2 trigger was used to reduce the rate of accepted events to less than 10 Hz. The level-2 central electron trigger made use of both calorimeter and tracking information. The hardware cluster finder was designed to make use of the projective nature of the calorimeter towers; the cluster finder searched the electromagnetic tower array forming clusters around seed towers. The seed towers were required to have at least 4 GeV of transverse energy (E_T), assuming the vertex position to be $Z = 0$. Each of the four nearest neighbors to a given seed tower were then included in the cluster if the tower had $E_T > 3.6$ GeV. Again, each of the nearest-neighbor were checked and if they were above the E_T threshold of $E_T > 3.6$ GeV then the towers were added to the cluster. This algorithm repeated until the cluster could not be extended. The hadronic E_T of the towers in the cluster was added to the electromagnetic E_T to give the total cluster E_T. These clusters were then matched in azimuth with high-transverse momentum tracks from the CFT [13].

The level-2 electron trigger required that: the cluster have transverse electromagnetic energy ($EM\ E_T$) of more than 12 GeV, assuming the event vertex to be $Z = 0$;

the ratio of total cluster E_T to EM E_T be less than 1.125 and that there be a CFT track associated with the cluster with transverse momentum of $P_T > 6.0$ GeV/c. The efficiency of the level-2 electron trigger for electrons with transverse energy $E_T > 15$ GeV was 98%.

A level-3 trigger system was also implemented during the running period, which consisted of a "farm" of 60 ACP (Advance Computer Project at FLAB) microcomputers based on Motorola 68020 coprocessors. The event data read out from the entire detector after a level-2 accept was available for use in level-3 trigger algorithms and level-3 trigger decisions. Because of constraints on the execution time per event, the level-3 trigger algorithms used streamlined versions of the complete off-line CDF event reconstruction code. The level-3 central electron filter required that the level-2 central electron cluster have EM $E_T > 12$ GeV and a two-dimensional track with $P_T > 6$ GeV/c as reconstructed by the level-3 software.

During the 1988-1989 collider run the level 3 trigger reduced the event acceptance rate from 10 Hz to $1-2$ Hz. The overall (level 1,2,3) trigger efficiency for central electrons associated with the inclusive W data sample was $97.3 \pm 0.5\%$.

3.5 Data Collection

The data samples used in this analysis were collected over a 12 month period. The peak machine luminosity was over 2×10^{30} cm^{-2}sec^{-1}. The overall trigger rate was limited to $1-2$ Hz by the speed at which data could be transferred to tape. A typical event record contained $\sim$ 120 kbytes of information. The total 4.4 pb^{-1} data sample consisted of 4×10^6 events recorded on 5500 magnetic tapes.

Chapter 4
Event Selection

This chapter describes the selection of $W \rightarrow e\nu + \gamma$ events. As mentioned in Chapter 2, $W\gamma$ represents a subsample of inclusive W production. This analysis used the inclusive electron W data sample (the same one used in the W cross section $\times$ branching ratio measurement and the electron W/Z cross section ratios [13, 8]) as a starting point. The event selection was divided into two parts: the W selection and the photon selection.

4.1 W Selection

In the 1988-1989 Tevatron collider run, CDF collected $\int \mathcal{L}dt = 4.05 \pm 0.28\ \mathrm{pb}^{-1}$ of high transverse momentum p_T electron data (note: this momentum is transverse to the beam direction). The uncertainty in the integrated luminosity was 6.8%, due primarily to the uncertainty associated with the total inelastic $p\bar{p}$ cross section as observed by the Beam-Beam Counters with $\sigma_{\mathrm{BBC}} = 46.8 \pm 3.2\ \mathrm{mb}$.

The W candidate events required an isolated well measured electron and large missing transverse energy (the signature of a neutrino in the CDF detector). These events came from the high p_T electron level-3 trigger. Since high p_T electron identification is crucial, to the selection of W candidate events. In this section the CDF electron identification is described.

4.1.1 Offline Clustering

Isolated electrons at CDF were found from energy clusters found in the electromagnetic calorimeters. These clusters were formed around seed towers with transverse electro-magnetic energy ($EM\ E_T$)[1] greater than 3 GeV. In the CEM calorimeter the clustering was limited to nearest neighbors (in η). Because the nature of the ϕ cracks between adjacent wedges in the CEM is larger than a typical electromagnetic shower in the CEM electrons do not deposit much energy across the phi cracks in the CEM calorimeter. This fact was confirmed by test-beam studies. [33] A cluster was formed when ratio of hadronic energy and electromagnetic energy from the towers in the cluster was less than $E_{HAD}/E_{EM} < 0.125$ and the total transverse electromagnetic energy $E_T^{EM} > 5.0$ GeV.

The inclusive electron W sample was obtained from the large transverse energy central ($|\eta_e| < 1.1$) electron sample. A brief description of the selection of the inclusive electron W sample is given below; a more complete description can be found in reference [13].

The inclusive W sample required a candidate central electron with the following properties:

- The event vertex was within $|z_{\rm vtx}| < 60.0$ cm of the nominal $z = 0.0$ position. As mentioned in the previous chapter, for a typical run during the 1988-1989 collider run, the vertex position varied about $z_{\rm vtx} = 0$ with a $\sigma_{\rm vtx} = 30$cm.

- The electron cluster was in the central portion of the detector $|\eta_e| < 1.1$, and was within the good fiducial region of the CEM calorimeter, as determined from CES shower centroid information.

The CDF detector is constructed to be symmetric in η and ϕ space. The

[1] the transverse energy E_T in a given calorimeter was defined as $E_T = E \sin\theta_i$. E is the energy measured in the calorimeter tower. The polar angle θ_i is angle between the center position in the tower and the event vertex.

fiducial region in the central part of the detector was selected to avoid the edges of the calorimeter where the electron response is erratic.

- Transverse energy of the cluster $E_T^{\text{cluster}} > 20.0$ GeV.

- Isolation $I \equiv (E_T^{\text{cone}} - E_T^{\text{cluster}})/E_T^{\text{cluster}} < 0.1$, in an angular cone of size $\Delta R = \sqrt{\Delta\eta^2 + \Delta\phi^2} = 0.4$ (in the $\eta - \phi$ plane) centered on the electromagnetic cluster (location defined from CES shower centroid information). E_T^{cone} is the sum of the transverse energy in the cone. This variable provided a measure of the energy deposition of other particles in the region of $\eta - \phi$ space directly surrounding the electromagnetic cluster.

- A hadronic (HAD) to electromagnetic (EM) energy ratio for the towers in the central electromagnetic cluster of Had/EM $< 0.055 + 0.00045 * \text{E}$, where E was the total energy of the EM cluster in GeV. An energy-independent efficiency for this cut was obtained using this functional form.

- A CES strip chi-square of $\chi^2_{\text{strip}} < 15$ from a fit of the cluster profile in the strip view to test-beam electron shower profiles.

- Lateral shower-shape chi-squared variable $L_{\text{shr}} < 0.2$, which is a chi-squared comparison of the observed lateral shower profile to test-beam electron lateral shower profile data. L_{shr} was defined as

$$L_{\text{shr}} = 0.14 \cdot \sum_i \frac{E_i^{\text{meas}} - E_i^{\text{pred}}}{\sqrt{0.14 \cdot E^2 + (\Delta E_i^{\text{pred}})^2}} \tag{4.1}$$

where the sum is over the towers in EM cluster (excluding the seed tower); E_i^{meas} is the measured energy in tower i; E_i^{pred} is the predicted energy in the tower i calculated from the seed tower energy, impact point from the CES shower centroid and event vertex using parameterized shower profiles from test-beam data; E is the EM energy of the cluster; and ΔE_i^{pred} is the uncertainty in E_i^{pred} associated with an 1 cm uncertainty in the impact point measurement. All energies are in GeV.

- A single reconstructed three-dimensional track associated with the EM cluster must have had a track position which matched the CES shower position to within $|\Delta z| < 3.0$ cm and $|\Delta r - \phi| < 1.5$ cm. The CES had a position resolution of 1.7mm for 50 GeV electrons at normal incidence.

- The ratio of electromagnetic energy (E) of the EM cluster to the momentum (P) of the track associated with the EM cluster must have been $E/P < 1.5$.

There were 5012 events that passed these requirements.

For central electrons the fiducial cuts in the η direction were made using the z coordinate of the electron shower centroid. (The CES measured the shower centroid in two coordinates: x (which corresponded to the $r - \phi$ direction) and $|z|$ (which corresponded to the η direction). The active CES region in the $|z|$ direction was $6.2\,\text{cm} < |z| < 239.4\,\text{cm}$ and the active CEM region was $4.2\,\text{cm} < |z| < 246.0\,\text{cm}$. [34] The fiducial cut in $z(\eta)$ required that $9.0\,\text{cm} < |z| < 217.0\,\text{cm}$. This cut removed electrons in Tower 9 of the CEM calorimeter. This was the smallest tower in the CEM in terms or radiation lengths and physical size.

The fiducial cuts in the ϕ direction for central electrons were made using the x coordinate from the CES detector. At the CES depth (184.15 cm) in the CEM calorimeter the wedge was 48.5 cm wide with an active width of 46.2 cm. The CES had an active width of 45.1 cm. The fiducial cut required that the CES position of the shower (in the x coordinate) $x_{\text{ces}} < 21.0\,\text{cm}$ from the center line of the wedge.

In addition to the symmetric cuts, there was a small region (one CEM tower) that was excluded due to the cable runs and cryostat lines required from the operation of the track chambers and solenoidal magnet. This excluded the region from $0.77 < \eta < 1.0$ and $75° < \phi < 90°$.

The measured energy in the CEM calorimeter tower was corrected in three ways: 1) by a correction based on position in the tower; 2) tower to tower corrections; and 3) overall energy scale correction. The response map correction used the CES

shower centroid (in order to accurately determine the position of the shower) and response function of a typical tower as a function of azimuthal (x) and z positions. This response map function was derived from test-beam electron data. Figure 4.1 shows the relative response in a central calorimeter tower as a function of azimuthal and z position. The response map correction had an accuracy of 1.1% within the fiducial region of the CEM. The tower to tower correction was derived from a sample of $\sim$ 17000 electrons with $E_T > 12\,\mathrm{GeV}$. The tower to tower response was then determined from the E/P distribution of these electrons. The overall scale was derived from the inclusive W sample using the E/P distribution of the electrons from the decay of the W boson with all other energy corrections applied. This E/P distribution from the inclusive W data was compared to calculations from a radiative W Monte Carlo event generator and complete detector simulation. The tracking chamber momentum scale was derived from the $J/\Psi \rightarrow \mu^+\mu^-$ invariant mass distribution. [13]

The candidate W events required the presence of an electron and neutrino. In CDF neutrinos from W decay were identified by a large transverse energy imbalance (missing E_T - $\not\!\!E_T$). Missing transverse energy ($\vec{\not\!\!E}_T$) was defined as,

$$\vec{\not\!\!E}_T = -\sum_i E^i \hat{\mathbf{n}}_i, \qquad \text{i = calorimeter tower number with } |\eta| < 3.6 \tag{4.2}$$

where E^i is the energy and $\hat{\mathbf{n}}_i$ is a unit vector perpendicular to the beam axis and pointing at the i^{th} calorimeter tower. For a tower to have been included in the sum, it must have passed a location dependant energy threshold of: 0.1 GeV in the CEM and CHA; 0.3 GeV in the PEM; 0.5 GeV in the PHA and PEM; and 0.8 GeV in the FHA. In the calculation of $\not\!\!E_T$ no energy corrections were applied.

Events passing both the Z and W selection criteria were excluded from the sample. The precise definition for Z^0 events can be found in the reference [13]. There were 2664 events that passed all W requirements.

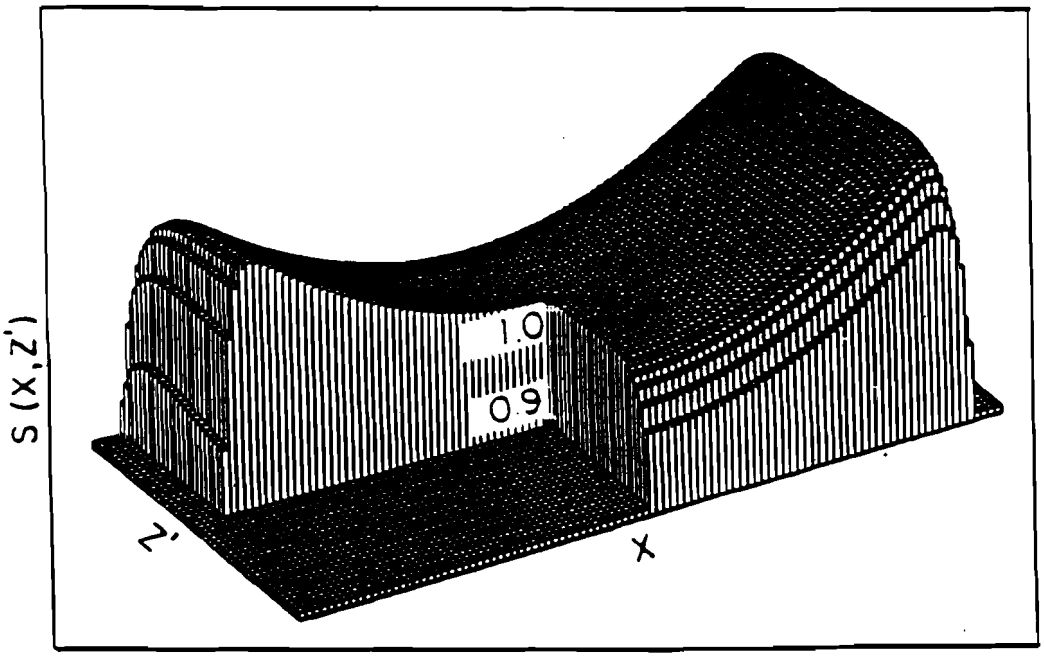

Figure 4.1: Relative response in a central calorimeter tower. The Z' axis in the beam direction and the X axis is in the azimuthal direction. The vertical scale gives the relative response across the tower face. The point labeled 1.0 is the point at which the tower is calibrated. The point labeled 0.9 has a relative response ten percent less than the 1.0 (calibration) point.
[13]

4.2 W γ Event Selection

As mentioned previously, the $W\gamma$ data sample for this analysis was selected from the CDF inclusive electron W data sample.

The photons were identified by the presence of a second electromagnetic cluster well separated from the electron from the decay of the W boson. As described in chapter 2, the E_T spectrum for photons from $W(\rightarrow e\nu)\ \gamma$ is a very steeply falling one . In order to have a measurable signal, this analysis looked for photons with E_T^γ as low as 5.0 GeV. As with the search for electrons from W decay, the photons were first identified by electromagnetic clusters in the CEM calorimeter. The default electromagnetic clustering E_T thresholds could not be used because of the efficiency "turn on" curve of the clustering near the threshold of 5 GeV (see figure 4.2). The η range was limited because the low-β quadrupoles of the Tevatron obscured part of the azimuthal regions of the forward calorimeters, $3.6 < |\eta| < 4.2$.

In order to insure that the electromagnetic clustering was fully efficient at $E_T^{\rm cluster} = 5.0\,{\rm GeV}$, the seed tower E_T threshold was lowered to $E_T^{\rm seed} \geq 1.0\,{\rm GeV}$ from the default of 3.0 GeV and the total transverse electromagnetic energy of the cluster threshold was lowered from 5.0 GeV (default) to 1.5 GeV.

A photon candidate was defined as:

- A 1-3 tower cluster of electromagnetic energy deposited in the CEM calorimeter with $E_t \geq 5.0$ GeV, after position response and CEM energy scale corrections, with a seed calorimeter tower energy of $E_t \geq 1.0$ GeV.

- A candidate CEM cluster was required to be in a good fiducial region of the central calorimeter, as defined by the position determined from CES shower centroid information. The fiducial region of the central calorimeter is described in the previous section.

- An angular separation between the W decay electron and the photon of $\Delta R_{e\gamma} =$

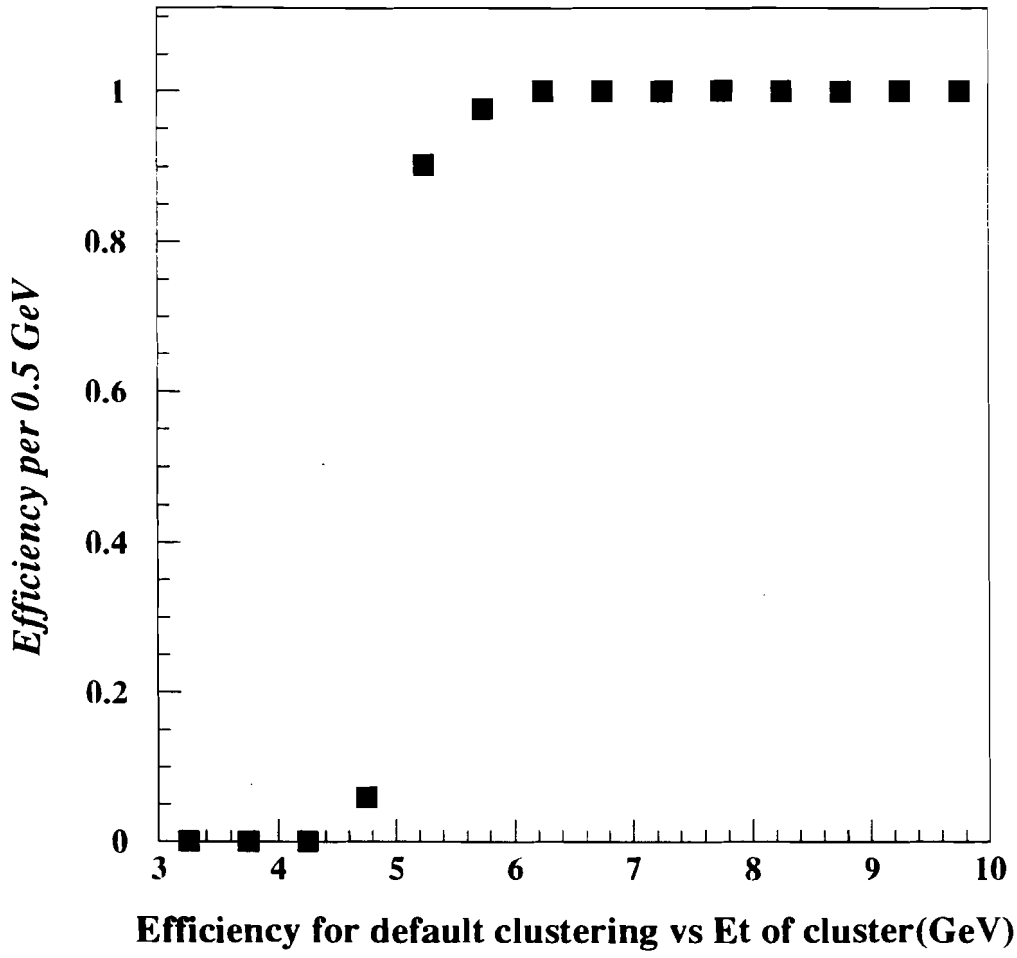

Figure 4.2: Clustering Efficiency "turn on" for default electromagnetic clustering in the CEM.

$\sqrt{\Delta\eta^2 + \Delta\phi^2} > 0.7$. This cut was designed to suppress the contribution from radiative W decay. $\Delta R_{e\gamma} = 0.7$ corresponds to an opening angle of $\Delta\phi \simeq 40°$ in the $r - \phi$ plane.

- A calorimeter isolation "$ET4$" cut, requiring that the excess transverse energy deposited in a cone of $\Delta R = 0.4$ centered on the CEM cluster, but not including the EM cluster energy must have been $ET4 < 2.0$ GeV.

$$ET4 \equiv E_T^{\text{cone}} - E_T^{clust} < 2.0 \text{ GeV} \tag{4.3}$$

- A tracking isolation "$\Sigma PT4$" cut, requiring that the summed transverse momentum due to charged tracks within a cone of $\Delta R = 0.4$ centered on the CEM cluster must be less than $\Sigma PT4 < 2.0$ GeV. The tracks participating in the sum must have originated within $\Delta z < 10$ cm of the event vertex, and be reconstructed in three dimensions.

- No tracks,originating from *any* vertex, pointed at the EM cluster. The tracks must be reconstructed in three dimensions. ($N3D = 0$ cut).

- A hadronic to electromagnetic energy ratio for the central EM cluster of $Had/EM < 0.055 + 0.00045 * E$, where E is the total energy of the EM cluster in GeV.

- A lateral shower-shape for the CEM cluster of $L_{shr} < 0.5$. The variable, L_{shr}, is defined in the previous section.

- The CES strip and wire chi-squares for the electron shower profiles of the leading cluster in each of these views, must be $\chi^2_{strip} < 20.0$ and $\chi^2_{wire} < 20.0$.

- A "no 2^{nd} CES" cut, requiring that no additional CES strip/wire clusters with $E_{CES\ 2^{nd}} > 1.0$ GeV be present within the CEM cluster. This cut was made to further suppress π^0 and multi-photon backgrounds.

The isolation cuts were made to reduce the background from QCD jets. The HAD/EM, L_{shr} and CES χ^2 cuts were made to remove jets and identify photons or electrons. The "no-track" cut differentiated photons from electrons. The "no 2^{nd} CES" cut suppressed the multi-photon background. Table 4.1 summarizes the effects of these cuts on the inclusive W and the QCD data sample used to estimate the background. The background estimate will be discussed further in chapter 6.

For $W\gamma$ candidates, a transverse mass cut of $M_T^W > 40$ GeV/c^2 was made to suppress the high$-P_T^{W\gamma}$ component of the $(W \rightarrow \tau\ \bar{\nu}_\tau)+\gamma,\quad \tau \rightarrow e\ \bar{\nu}_e\ \nu_\tau$ background. The W transverse mass is defined as $M_T^W \equiv \sqrt{2P_T^e\ P_T^{\bar{\nu}_e}\ (1-\cos\Delta\phi_{e-\bar{\nu}_e})}$, where $\Delta\phi_{e\bar{\nu}_e}$ is the opening angle between the $W-$decay electron and neutrino in the $r-\phi$ plane. The cluster transverse mass (also known as the minimum invariant mass) of the $W+\gamma$ system is defined as:

$$M_{CT}^W \equiv \sqrt{\left[\left(M_{e\gamma}^2 + |\vec{\mathbf{P}}_T^{\gamma} + \vec{\mathbf{P}}_T^{e}|^2\right)^{\frac{1}{2}} + |\vec{\mathbf{P}}_T^{\bar{\nu}_\ell}|\right]^2 - |\vec{\mathbf{P}}_T^{\gamma} + \vec{\mathbf{P}}_T^{e} + \vec{\mathbf{P}}_T^{\bar{\nu}_e}|^2} \qquad (4.4)$$

where $M_{e\gamma}$ is the invariant mass of the electron-photon system.

After all cuts, there were 8 candidate $W\gamma$ events.

Figures 4.3 and 4.4 show the effect of the cuts on the inclusive electron W data sample. Figures 4.5, 4.6 and 4.7 show some of the kinematic properties of the electron $W\gamma$ candidate events, overlaid with the Monte Carlo expectations for the signal and background. (These will be discussed in greater detail in the next two chapters.) Table 4.2 contains the salient kinematic properties of the electron $W\gamma$ candidate events.

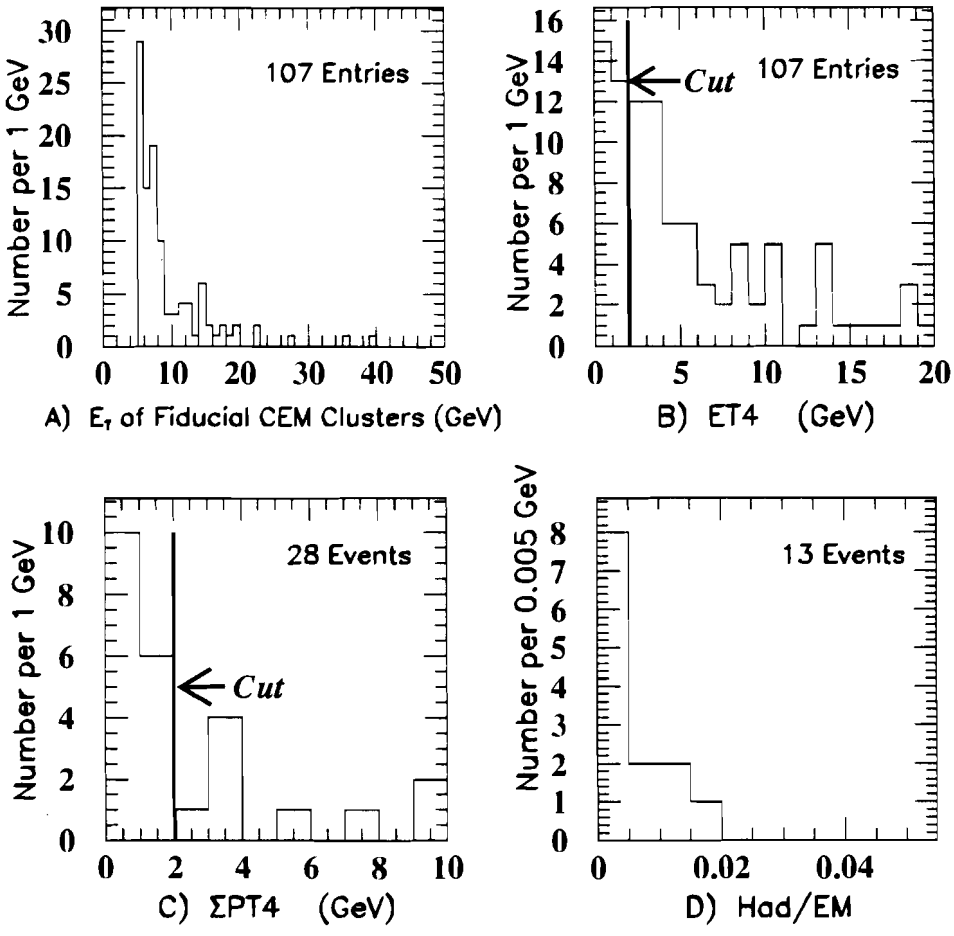

Figure 4.3: Photon variables as a function of photon cuts, for the electron $W\gamma$ data sample. (A) E_T distribution of fiducial CEM clusters passing the $E_T^\gamma > 5.0$ GeV cut and the $\Delta R_{\ell\gamma} > 0.7$ angular separation cut. (B) The calorimeter isolation distribution before the $ET4 < 2.0$ GeV cut is applied. (C) The tracking isolation distribution before the $\Sigma PT4 < 2.0$ GeV/c cut is applied. (D) The Had/EM distribution before the Had/EM cut is applied.

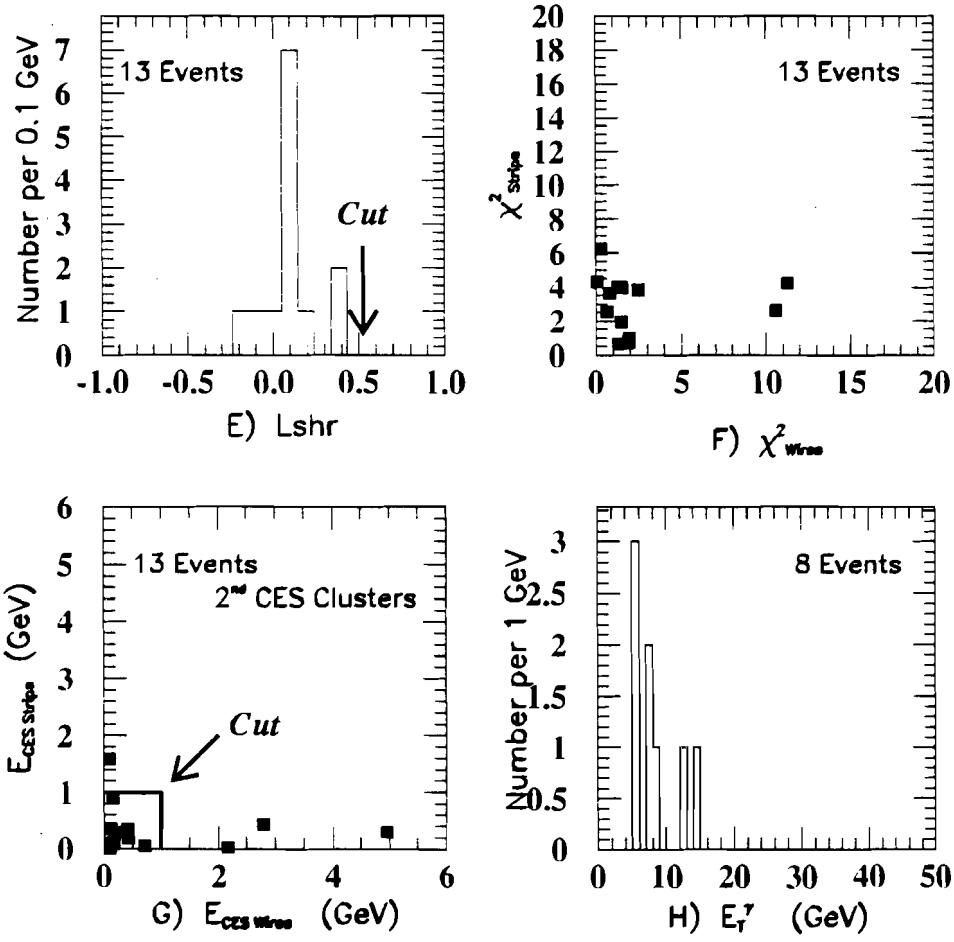

Figure 4.4: Photon variables as a function of photon cuts, for the electron $W\gamma$ data sample. (E) The L_{shr} distribution before the $L_{shr} < 0.5$ cut is applied. (F) A scatterplot of CES χ^2_{strips} *vs.* χ^2_{wires} before the $\chi^2_{strips} < 20.0$ and $\chi^2_{wires} < 20.0$ cut is applied. (G) A scatterplot of CES E_{strips} *vs.* E_{wires} before the no 2^{nd} CES cluster $E > 1.0$ GeV cut is applied. (H) The E_T^γ distribution after all photon cuts have been applied, including the no 2^{nd} high$-P_T$ track cut for suppression of background from mis-identified electron $Z + \gamma$.

Table 4.1: Summary of electron $W\gamma$, and QCD Background Passing Successive Photon Cuts. The entries in the first row in the first columns are the number of inclusive electron W events; the entries in the other rows of the first column are the number of W events with fiducial CEM clusters surviving the application of successive photon cuts. In the last column, the entry in the first row is the number of central, non-leading jets passing the jet selection criteria. The other entries in this column are the number of fiducial CEM clusters surviving the application of successive photon cuts. See text for further details.

	electron $W\gamma$	QCD background
Inclusive W or QCD Data Samples	2664	11726
Pass FidCEM, $E_T^\gamma > 5.0$ GeV, $\Delta R_{e\gamma} > 0.7$ Cuts	107	266
Pass $ET4 < 2.0$ GeV Cut	28	107
Pass $\Sigma PT4 < 2.0$ GeV Cut	16	64
Pass $N3D = 0$ Cut	13	57
Pass Had/EM Cut	13	55
Pass $L_{shr} < 0.5$ Cut	13	42
Pass $\chi^2_{strip} + \chi^2_{wire}$ Cut	13	32
Pass no 2^{nd} $CES > 1$ GeV Cut	9	20
Pass no 2^{nd} Isolated Track Cut ($W\gamma$ only)	8	–

Table 4.2: Kinematic Properties of Electron $W\gamma$ Candidates. $\Delta R_{e\gamma}$ is the angular separation in the η-ϕ plane between the decay electron and the photon. M_T^W is the W transverse mass. M_{CT}^W is the cluster transverse mass.

	Run # Event #	E_T^γ (GeV)	Q_W (e)	M_T^W (GeV)	M_{CT}^W (GeV)	$\Delta R_{e\gamma}$
1	16801 – 6582	5.17	−1	68.3	80.5	1.28
2	16807 – 4706	8.65	+1	63.8	74.0	0.84
3	17467 – 15981	14.43	−1	59.2	79.1	0.80
4	17529 – 442	5.04	−1	60.8	68.5	2.01
5	17886 – 1796	5.04	−1	83.2	88.5	2.53
6	18720 – 20145	12.29	+1	68.8	96.4	0.76
7	19430 – 20694	7.44	−1	78.4	86.3	0.87
8	19882 – 38400	7.04	+1	85.6	86.7	1.10

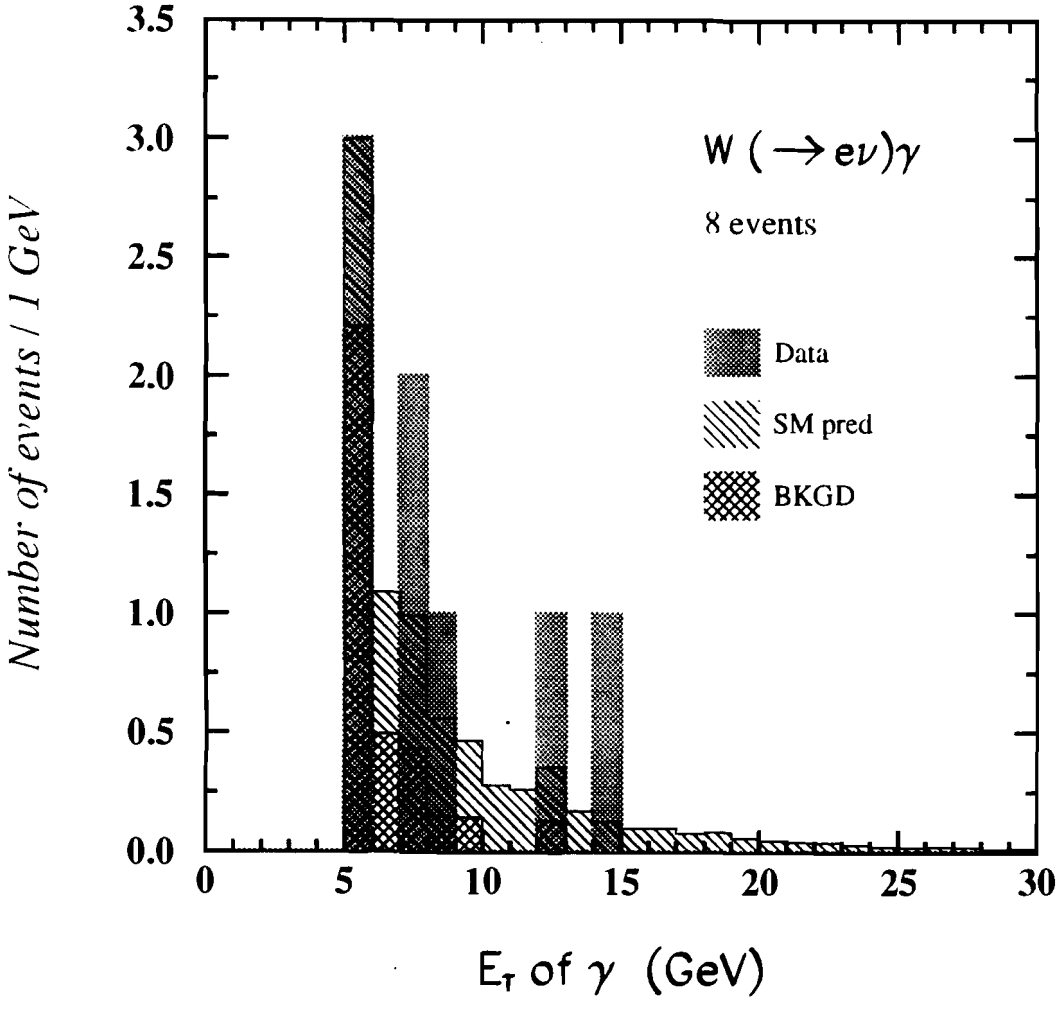

Figure 4.5: E_T of the photon for the 8 $W\gamma$ candidate events

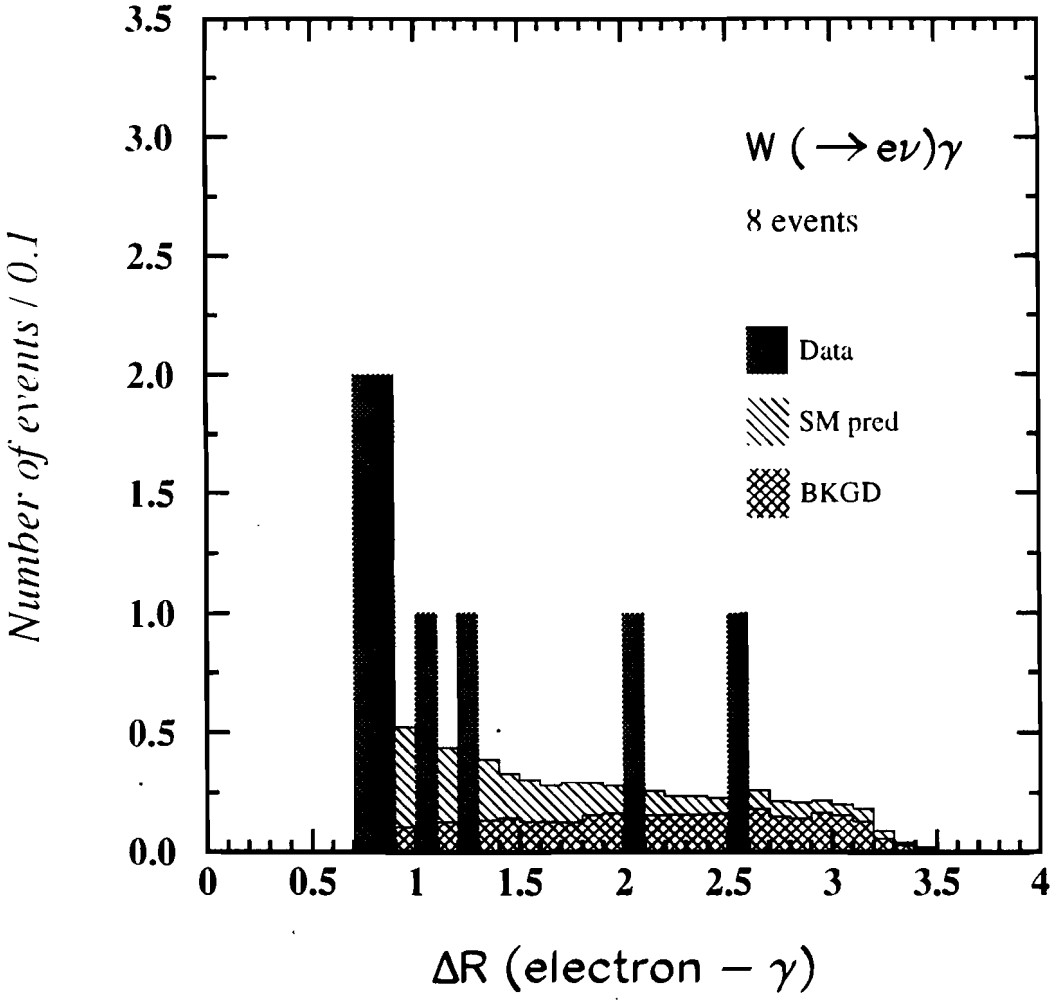

Figure 4.6: Angular separation ($\Delta R_{e\gamma}$) between the electron from the decay of the W boson and the photon for the 8 $W\gamma$ candidate events

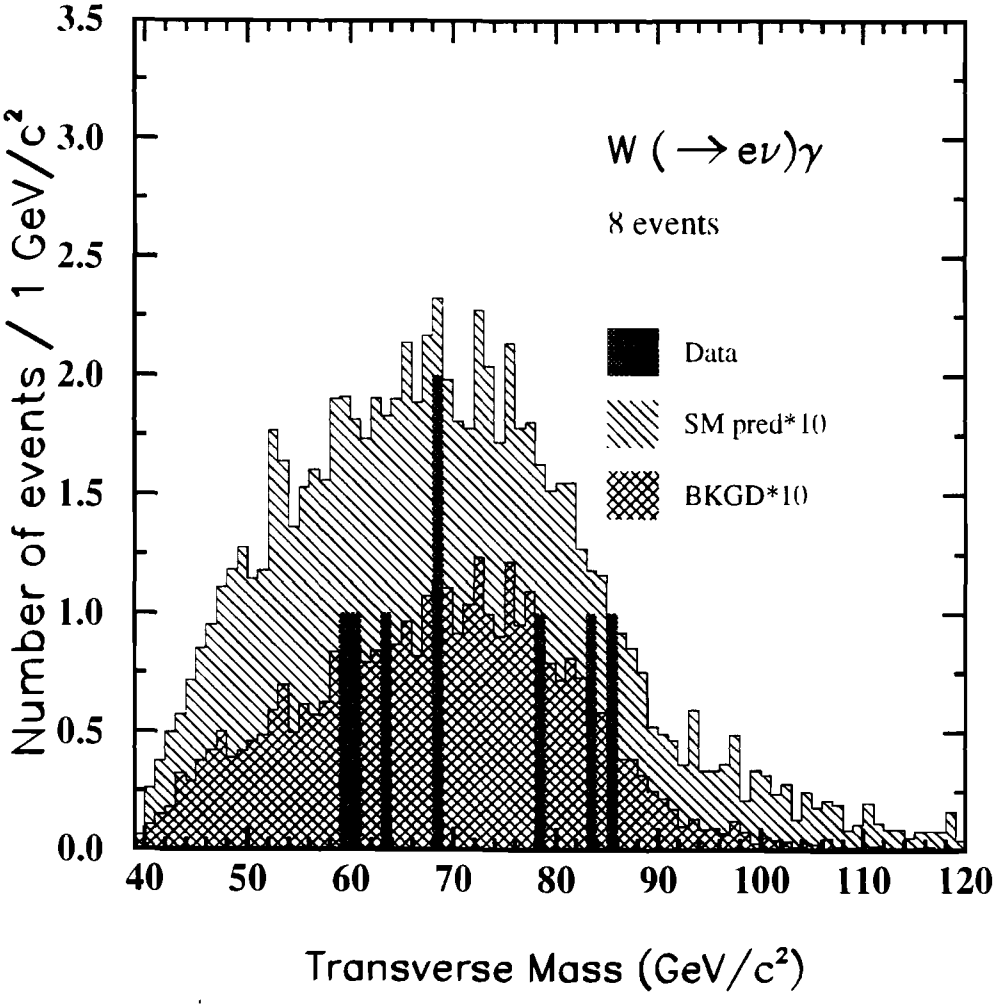

Figure 4.7: Transverse Mass (M_T^W) of the W for the 8 $W\gamma$ candidate events

Chapter 5

Acceptances and Efficiencies

The efficiency for selecting $W\gamma$ events and the overall acceptance factors for $W\gamma$ events are required in order to determine the cross section $\times$ branching ratio for the process $W\,(\rightarrow\, e\nu)\,\gamma$. The overall acceptance $\times$ efficiency for selecting $W\gamma$ events can be written as:

$$A_{W\gamma}\cdot\epsilon_{W\gamma}\;=\;(\epsilon_{zvx}\cdot T\cdot\epsilon^{e}\cdot\epsilon^{\gamma})\cdot\left(A_{M_W^T}\cdot A_W\cdot f^{\gamma}\cdot A^{\gamma}\right) \tag{5.1}$$

The terms in this equation will be defined in subsequent sections.

The kinematic and geometrical acceptances of $W\gamma$ events were obtained from detailed Monte Carlo simulations of this process. The electron and photon efficiencies were determined from various $p\bar{p}$ and test-beam data samples and cross-checked with various detailed Monte Carlo simulations.

5.1 Baur $W\gamma$ Monte Carlo Event Generator

The Baur $W\gamma$ Monte Carlo event generator [17] was used to simulate the production and decay of $W\gamma$ events. The Baur $W\gamma$ event generator program generates weighted events using the helicity-amplitude formalism, adding together the contributions of the Feynman graphs of figure 2.1. The kinematic phase space calculations are done using the VEGAS adaptive multi-dimensional integrating code [37]. The Baur $W\gamma$ Monte Carlo was modified to use the CERN library of parton distribution functions [38] and include *all* parton-parton luminosities and the Cabbibo-Kobayashi-Maskawa [CKM] quark mixing matrix elements [38]. The HMRS-B [40] structure functions

are the structure functions used in this analysis; these structure functions were also used in the determination of the CDF electron W and Z cross sections [12] and the CDF electron W/Z cross section ratio [13]. The cross section output from the Baur $W\gamma$ Monte Carlo includes a "K-factor" of $\left[1 + \frac{8\pi}{9}\alpha_s(M^2_{W\gamma}\right] \approx 1.35$ to approximate higher order QCD processes such as $q + \bar{q} \rightarrow g + W + \gamma$ and $q + q \rightarrow q + W + \gamma$. [41] The Standard Model results predicted by the Baur Monte Carlo event generator were compared with several other $W\gamma$ Monte Carlo event generators, such as ISAJET [35], VVJET [41], PAPAGENO [42], PYTHIA [43] and the CDF radiative W decay Monte Carlo event generator WZRAD [44]. The cross section results are in good agreement between the various Monte Carlo event generators for the various different regimes of comparison. The systematic uncertainties associated with the BAUR $W\gamma$ Monte Carlo results were also studied by:

- varying the shape of the $p_T(W\gamma)$ distribution
- using several different structure function choices
- studying the Q^2 scale dependence of the calculation.

These systematic uncertainties are discussed in greater detail in chapter 7.

A large sample ($> 500,000$ events) of Baur $W\gamma$ Monte Carlo events were generated with extremely loose cuts on the electron momentum and pseudo-rapidity of the electrons and photons ($|\eta_e|$, $|\eta_\gamma| < 6$); however a minimum photon transverse energy $E_T^\gamma > 1.0\,\mathrm{GeV}$ and minimum angular separation between the decay electron and photon of $\Delta R_{e\gamma} > 0.3$. were imposed to avoid divergences in the Monte Carlo calculation. These loose cuts maximized the total $W\gamma$ cross section while minimizing the potential biases associated with finite detector resolution and smearing effects on the steeply-falling kinematic distributions (most importantly the photon E_T^γ distribution).

5.2 Monte Carlo Detector Simulations

The four vector information for the final-state particles in each $W\gamma$ Monte Carlo event was then input into either: a "fast" Monte Carlo detector simulation detector which parameterized the detailed response of the CDF detector; or a more detailed simulation of the CDF detector which included the QCD-evolution/fragmentation of the underlying event through ISAJET [35] and then through the QFL [36] detector simulation, which also simulated the detailed response of the CDF detector using the parameterization method.

The purpose of the "fast" $W\gamma$ detector simulation program was threefold:

1. determine all kinematic and geometric acceptance factors;

2. obtain predicted cross sections $\sigma \cdot B(W+\gamma)$ for events passing all $W\gamma$ event selection cuts. These cross sections, $\sigma \cdot B(W+\gamma)$, can be used to predict the number of $W\gamma$ events.

The QFL detector simulation program was used to check the results from the "fast" detector simulation program.

5.3 Geometric and Kinematic Acceptances

The overall acceptance for $W\,(\rightarrow e\nu)\,\gamma$ events is

$$A_{W\gamma} \;=\; A_{M_W^T} \cdot A_W \cdot f^\gamma \cdot A^\gamma \tag{5.2}$$

$A_{M_W^T}$ is the acceptance of the transverse mass cut $M_W^T > 40$ GeV/c^2 for $W\gamma$ events passing all other cuts.

The overall acceptance for $W \rightarrow e\nu$ events is written as $A_W = A^W_{E_T} \cdot A^W_{fid} \cdot A^{\nu}_{\not\!\!E_T}$ where $A^W_{E_T}$ is the kinematic acceptance for central fiducial electrons with $E_T >$ 20 GeV, A^W_{fid} is the geometrical acceptance for fiducial central electrons and $A^{\nu_e}_{W\ \not\!\!E_T}$ is the kinematic acceptance for the $\not\!\!E_T > 20$ GeV cut.

The term f^{γ}_{Wcem} is defined as the fraction of all photons that are central ($|\eta_{\gamma}| < 1.1$) which are produced in $W\gamma$ events where the W decay electrons pass the W selection requirements and the photon has already satisfied the $E^{\gamma}_T > 5.0$ GeV and $\Delta R_{e\gamma} > 0.7$ requirements.

The overall photon acceptance is given by:

$$\begin{aligned} A^{\gamma} &= A^{\gamma}_{E^{\gamma}_T} \cdot A^{\gamma}_{fid} \cdot A^{\gamma}_{\Delta R_{e\gamma}} = 1.0 \cdot A^{\gamma}_{fid} \cdot 1.0 \\ &= A^{\gamma}_{fid} \end{aligned} \tag{5.3}$$

A^{γ}_{fid} is the geometrical acceptance for photons (from $W\gamma$ events) in central ($|\eta_{\gamma}| < 1.1$) region satisfying $E^{\gamma}_T > 5.0$ GeV and $\Delta R_{e\gamma} > 0.7$.

Since we are measuring only that portion of the (total) production cross section $\times$ branching ratio, associated with photons above $E^{\gamma}_T > 5.0$ GeV, the kinematic acceptance factor, $A^{\gamma}_{E^{\gamma}_T} = 1.0$ by definition.

Similarly, the lepton-photon angular separation acceptance factor for central photons is $A^{\gamma}_{\Delta R_{e\gamma}} = 1.0$. The product $f^{\gamma} \cdot A^{\gamma}$ is therefore the acceptance factor for central fiducial photons from $W\gamma$ events that have already satisfied the W selection and $E^{\gamma}_T > 5.0$ GeV and $\Delta R_{e\gamma} > 0.7$ requirements.

The Baur $W\gamma$ Monte Carlo and the "fast" Monte Carlo detector simulation were used to determine the overall acceptance factors for the W boson and the photons for the nominal set (HMRS-B) set of structure functions. These acceptance factors are listed in table 5.1.

The term A^{γ}_{gen} represents the overall kinematic $\times$ geometric acceptance factor for photons in $W\gamma$ events *generated* by the BAUR Monte Carlo and simulated with the "fast" Monte Carlo detector simulation to pass the $E^{\gamma}_T > 5.0\,\mathrm{GeV}$ and $\Delta R_{e\gamma} > 0.7$ cuts. These photons were generated with $E^{\gamma}_T > 1.0\,\mathrm{GeV}$ and $\Delta R_{e\gamma} > 0.3$. Also, f^{γ}_{gen} represents the fraction of $W\gamma$ events generated where the W boson passes all selection criteria and the photon satisfies: $E^{\gamma}_T > 5.0\,\mathrm{GeV}$ and $\Delta R_{e\gamma} > 0.7$.

Table 5.1: W boson and photon overall acceptance factors from $W\gamma$ Monte Carlo

Acceptance factor	
A_W	$27.6 \pm 0.01\%$
$A_{M_W^T}$	$94.3 \pm 0.8\%$
A^γ	$77.9 \pm 0.2\%$
f^γ	$48.2 \pm 0.3\%$
A^γ_{gen}	$13.5 \pm 0.1\%$
f^γ_{gen}	$47.0 \pm 0.1\%$

The individual acceptances required to compute $A_{W\gamma}$,A_W and A^γ are summarized in table A.1 of Appendix A.

5.4 Efficiencies

The overall selection efficiency for $W\ (\rightarrow e\nu)\ \gamma$ can be written as:

$$\epsilon_{W\gamma} \ = \ \epsilon_{zvx} \cdot T \cdot \epsilon_e \cdot \epsilon_\gamma \tag{5.4}$$

The factor ϵ_{zvx} is the efficiency of the $|z_{\rm vertex}| < 60$ cm cut.

The overall W electron trigger efficiency for the central electron selection is $T \ = \ \epsilon_{L1} \cdot \epsilon_{L2} \cdot \epsilon_{L3}$, where the ϵ_{Li}, $i = 1-3$ are the individual level-1 - level-3 electron trigger efficiencies, respectively.

The overall electron and photon selection efficiencies are ϵ_e and ϵ_γ, respectively.

5.4.1 Electron Efficiency

The overall central fiducial electron selection efficiency from the decay of the W boson is given by:

$$\epsilon_e = \epsilon_{iso}^{cem} \cdot \epsilon_{(Had/EM)}^{cem} \cdot \epsilon_{\chi^2_{strip}}^{cem} \cdot \epsilon_{Lshr}^{cem} \cdot \epsilon_{(E/P)}^{cem} \cdot \epsilon_{trk}^{cem} \cdot \epsilon_{\Delta z}^{cem} \cdot \epsilon_{\Delta x}^{cem} \quad (5.5)$$

where the individual efficiencies for the central electron selection are the isolation $I < 0.1$ cut, ϵ_{iso}^{cem}; the Had/EM cut, $\epsilon_{(Had/EM)}^{cem}$; the CES strip $\chi^2 < 20$ cut, $\epsilon_{\chi^2_{strip}}^{cem}$; the $L_{\rm shr} < 0.2$ cut, ϵ_{Lshr}^{cem}; the $E/P < 1.5$ cut, $\epsilon_{(E/P)}^{cem}$; CTC electron track reconstruction, ϵ_{trk}^{cem} and the CTC-CES $\Delta z < 3.0$ cm and $\Delta r - \phi < 1.5$ cm track match cuts, $\epsilon_{\Delta z}^{cem}$ and $\epsilon_{\Delta x}^{cem}$, respectively.

Since W selection cuts for this sample were the same as those used in the determination of the inclusive electron W $\sigma \cdot B$ cross section [8] and the W/Z cross section ratios [13], the W decay electron efficiencies determined in those analysis are applicable here. These efficiencies are summarized in table B.1 of Appendix B.

The overall electron efficiency is:

$$\epsilon_e = 84.0 \pm 3.0\% \quad (5.6)$$

5.4.2 Photon Efficiency

The central fiducial photon selection efficiency is given by

$$\epsilon_{cem}^{\gamma} = \epsilon_{ET4}^{\gamma} \cdot \epsilon_{\Sigma PT4}^{\gamma} \cdot \epsilon_{N3D}^{\gamma} \cdot \epsilon_{Had/EM}^{\gamma} \cdot \epsilon_{Lshr}^{\gamma} \cdot \epsilon_{\chi^2_{stp}+\chi^2_{wir}}^{\gamma} \cdot \epsilon_{no\ 2^{nd}\ CES}^{\gamma} \cdot \mathcal{P}_{conv}^{\gamma} \cdot \mathcal{S}_{e\to\gamma}^{cem} \quad (5.7)$$

where the individual terms are the central fiducial photon efficiencies for passing the calorimeter isolation $ET4 < 2.0$ GeV cut, ϵ_{ET4}^{γ}, followed in sequence by the tracking isolation $\Sigma PT4 < 2.0$ GeV cut, $\epsilon_{\Sigma PT4}^{\gamma}$; the $N3D = 0$ cut, ϵ_{N3D}^{γ}; the Had/EM cut, $\epsilon_{Had/EM}^{\gamma}$; the $L_{shr} < 0.5$ cut, ϵ_{Lshr}^{γ}; the CES $\chi^2_{strip} < 20$ and χ^2_{wire} cuts, $\epsilon_{\chi^2_{stp}+\chi^2_{wir}}^{\gamma}$ and the no 2^{nd} CES strip or wire clusters with $E_{2^{nd}}^{ces} > 1$ GeV cut,

$\epsilon^{\gamma}_{no\ 2^{nd}\ CES}$. The factor $\mathcal{P}^{\gamma}_{\overline{conv}}$ is the survival probability for a photon to traverse the material of the inner central detector without converting to an e^+e^- pair. The factor $\mathcal{S}^{cem}_{e\to\gamma}$ is a small correction to account for differences in EM shower development for electrons *vs.* photons, since electron test beam data was used to determine some of the individual photon efficiencies.

The calorimeter isolation (ϵ^{γ}_{ET4}) and tracking isolation ($\epsilon^{\gamma}_{\Sigma PT4}$) efficiencies were determined from studies of the underlying event in the inclusive electron W data sample. The Baur/ISAJET/QFL $W\gamma$ Monte Carlo simulation was used to check these efficiencies. Both sets of results were comparable though the efficiencies determined from Monte Carlo data were larger than those determined from the data. The ISAJET Monte Carlo simulation appears to have added a "quieter" under-lying event in terms of charged and neutral particle multiplicities and p_T spectra of tracks than the comparable quantities in the inclusive W data set.

The efficiencies :ϵ^{γ}_{N3D}; $\epsilon^{\gamma}_{Had/EM}$; ϵ^{γ}_{Lshr}; $\epsilon^{\gamma}_{\chi^2_{strp}+\chi^2_{wire}}$ and $\epsilon^{\gamma}_{no\ 2^{nd}\ CES}$ were determined from electron test-beam data taken in the energy range $5\,\mathrm{GeV} < E^e_T < 50\,\mathrm{GeV}$. Data from the Baur/ISAJET/QFL $W\gamma$ Monte Carlo simulation was used as cross-check and found to be comparable.

The photon survival probability factor $\mathcal{P}^{\gamma}_{\overline{conv}}$ is known from the average amount of material in the inner portion of the CDF detector, $\langle \Delta T \rangle = 4.6 \pm 0.3\%$ of a radiation length, χ^e_0 ($3.6\pm0.2\%$ of a conversion length χ^{γ}_0) [27, 45]. The Monte Carlo simulations provided a cross-check on $\mathcal{P}^{\gamma}_{\overline{conv}}$ by determining the fraction of $W\gamma$ Monte Carlo events where the photon, had it not converted into an e^+e^- pair, would have passed all photon cuts. The Monte Carlo $W\gamma$ result is in good agreement with the calculation; the difference between the two methods is used to define the systematic uncertainty associated with $\mathcal{P}^{\gamma}_{\overline{conv}}$. Another check on $\mathcal{P}^{\gamma}_{\overline{conv}}$ was to explicitly look for isolated conversion pairs in the $W\gamma$ data sample; no such pairs were found.

The photon *vs.* electron electromagnetic shower development factor $\mathcal{S}^{cem}_{e\to\gamma}$ was determined by comparing QFL photon *vs.* electron Monte Carlo simulations.

Table B.3 in appendix B summarizes the individual CEM photon selection efficiencies, photon survival probability, electromagnetic shower correction factor for showers due to electrons vs photons and the overall CEM photon selection efficiency. The statistical and systematic uncertainties associated with each quantity are also included.

The overall central photon *selection* efficiency is

$$\epsilon^{\gamma}_{cemsel} = 85.0 \pm 1.0(stat) \pm 2.0(syst)\% \tag{5.8}$$

The overall CEM photon efficiency, *including* the photon survival probability, $\mathcal{P}^{\gamma}_{\overline{conv}}$ and the $e \rightarrow \gamma$ electromagnetic shower development correction factor, $\mathcal{S}^{cem}_{e\rightarrow\gamma}$ is

$$\epsilon^{\gamma}_{cem} = 82.0 \pm 1.2(stat) \pm 2.4(syst)\% \tag{5.9}$$

5.5 Theory Predictions for $W\gamma$ signal

The Standard Model prediction for the number of expected electron $W\gamma$ events for an integrated luminosity $\int \mathcal{L}dt = 4.05 \pm 0.28$ pb^{-1} was obtained from the Baur $W\gamma$ Monte Carlo event generator and the "fast" Monte Carlo detector simulation programs. In excess of 500,000 $W\gamma$ events were generated and $\sim$ 50,000 Monte Carlo events passed all the event selection cuts.

The overall acceptance $\times$ efficiency term ($A_{W\gamma} \cdot \epsilon_{W\gamma}$) and the predicted number of $W\gamma$ events as determined by the Baur $W\gamma$ Monte Carlo event generator and the "fast" Monte Carlo detector simulation were cross-checked internally, as well as analytically and by comparing the results from the Baur/ISAJET/QFL $W\gamma$ Monte Carlo programs. Several hundred Baur/ISAJET/QFL $W\gamma$ Monte Carlo events passed all cuts. Table 5.2 contains the predicted number of events from the Baur/"fast" detector simulation and Baur/ISAJET/QFL simulation for an integrated luminosity of $\int \mathcal{L}dt = 4.05 \pm 0.28$ pb^{-1}.

Table 5.2: Standard Model Monte Carlo predicted number of events

Monte Carlo programs	Number of events
Baur + "fast" $W\gamma$ MC	4.56 ± 0.43
Baur/ISAJET/QFL $W\gamma$ MC	4.27 ± 0.57

5.6 Overall Acceptances $\times$ Efficiencies for $W\gamma$

From equation 5.1 the overall acceptance $\times$ efficiency for selecting a $W\gamma$ event can be written as:

$$A_{W\gamma} \cdot \epsilon_{W\gamma} = (\epsilon_{zvx} \cdot T \cdot \epsilon^{e} \cdot \epsilon^{\gamma}) \cdot \left(A_{M_W^T} \cdot A_W \cdot f^{\gamma} \cdot A^{\gamma}\right) \tag{5.10}$$

The overall acceptance $\times$ efficiency and the acceptances and efficiency are summarized in table 5.3.

Table 5.3: Summary of acceptances and efficiencies for $W\gamma$

$A_{W\gamma} \cdot \epsilon_{W\gamma}$	$6.0 \pm 0.4\%$
ϵ_{zvx}	$95.4 \pm 0.1\%$
T	$97.3 \pm 0.5\%$
ϵ^e	$84.0 \pm 3.0\%$
ϵ^γ	$82.1 \pm 2.7\%$
$A_{M_W^T}$	$94.3 \pm 0.8\%$
A_W	$27.6 \pm 0.1\%$
f^γ	$48.2 \pm 0.3\%$
A^γ	$77.9 \pm 0.2\%$

Chapter 6

Backgrounds

In order to determine the cross section $\times$ branching ratio for the process: $W(\rightarrow e\bar{\nu})\gamma$, the number of signal events $\mathcal{N}^{W\gamma}_{\mathbf{signal}}$ is needed:

$$\mathcal{N}^{W\gamma}_{\mathbf{signal}} = \mathcal{N}^{W\gamma}_{\mathrm{cand}} - \mathcal{N}^{W\gamma}_{\mathrm{bkgd}} \tag{6.1}$$

In Chapter 4 it was shown that $\mathcal{N}^{W\gamma}_{\mathrm{cand}} = 8$ events. In this chapter the methods used for determining the background are discussed.

The backgrounds to the process $W\gamma$ come from several sources. In the first section the largest and most problematic background, coming from $W + jets$ production where the jet mimics a photon, is discussed. The processes $Z^0 + jets$ and $Z^0 + \gamma$ are also backgrounds to $W\gamma$ when one of the decay leptons from $Z \rightarrow e^+e^-$ is not reconstructed. These and the tau lepton backgrounds are discussed in section 6.2.

6.1 QCD Backgrounds

6.1.1 General Methodology

The largest photon background in the $W\gamma$ signal sample is due to mis-identified QCD jets, where a central jet ($|\eta_{jet}| < 1.1$) in W+Jet events fragments in such a way as to mimic a photon, as defined by the photon cuts. To a lesser extent, another background source is due to prompt, isolated photons from initial/final-state radiation (quark QED bremsstrahlung) processes. However, initial/final-state radiation

is technically considered part of the $W\gamma$ *signal*, since the Feynman diagrams for initial state radiation, as shown in figures 2.1 are included in the theory calculation for the $W\gamma$ signal; as mentioned in section 5.1. To account for contributions from final-state radiation diagrams, a $K-$factor has to be applied when using the Baur MC $W\gamma$ event generator.

Because the QCD background in $W\gamma$ events could not be estimated directly from the data itself, the QCD jet fragmentation probability function $\mathcal{P}_{Jet\rightarrow\text{"}\gamma\text{"}}^{Control\ Sample}(E_T)$ was used to estimate the QCD background in the $W\gamma$ data set. The QCD fragmentation probability function is defined as the probability as a function of E_T that a jet will fragment into a particle or particles that mimic a "photon" as defined by the photon selection cuts. This method used data from independent non-signal control data sample (this non-signal control sample will be discussed in section 6.1.2) to determine the jet fragmentation probability function and convoluted this probability distribution with the E_T distribution of central jets in the W data sample. This method assumed that the jet fragmentation probability is the same in the non-signal control data sample and the W data sample over the photon E_T range of interest, *i.e.* that

$$\mathcal{P}_{Jet\rightarrow\text{"}\gamma\text{"}}^{Control\ Sample}(E_T) \;=\; \mathcal{P}_{Jet\rightarrow\text{"}\gamma\text{"}}^{W}(E_T) \qquad (6.2)$$

By using the *inclusive* W+Jets data sample the *inclusive* QCD jet background from *all* such sources will automatically be taken into account. For example, the inclusive $W+$ QCD jet background for the $W\gamma$ data samples will consist of a contribution from (a) "direct" W+Jet background, with *additional* QCD jet background contributions from (b) mis-identified Z+Jet events, where one of the Z decay leptons is not detected, but satisfies the $W\gamma$ event selection criteria, and (c) $(W \rightarrow \tau\ \bar{\nu}_\tau)$+Jet events, where $\tau \rightarrow e\ \bar{\nu}_e\ \nu_\tau$, again satisfying the $W\gamma$ event selection criteria.

The background data set chosen had to be kinematically similar to the W data set and could not contain processes other than jet fragmentation that produced isolated photons. The control data sample also had to have a large number of jets

in order to accurately determine the rate at which a jet mimicked a photon. A sample of multi-jet QCD events was selected and could be used to measure the jet fragmentation probability. The jets in the QCD data used to determine the jet fragmentation function were similar to the jets in the W data. Their $E_T^{\rm jet}$ spectra were similar.

6.1.2 QCD non-signal control data sample

The QCD fragmentation probability function was obtained using a 4.2 $\rm pb^{-1}$ sample of inclusive QCD jet data taken concurrently with the inclusive W data during the 1988-1989 run. The trigger requirement for these QCD events was a localized cluster of energy deposited in the calorimeter with $E_T > 20\,\rm GeV$. The jet clustering cone size used in this data sample was $\Delta R_{clust}^{Jet} = \sqrt{\Delta\eta^2 + \Delta\phi^2} = 0.7$ [1]. There were 39361 events in this sample before any off-line cuts were made. In the off-line analysis of this data, jet energy corrections were applied to correct for non-linear calorimeter response effects, calorimeter energy scale corrections and energy corrections to account for losses in un-instrumented regions of the calorimeters, etc.

An off-line event selection was used to choose events in the QCD control sample kinematically similar to event from hadronic W decay. These events were required to have at least three jets: two leading "trigger" jets and a non-leading central jet. The two highest E_T (leading) jets [2] were required to have $E_T^{\rm jet} > 15\,\rm GeV$ (corrected) and one jet with ($|\eta_{\rm jet}| < 1.1$) and the other jet ($|\eta_{\rm jet}| < 2.4$) and a dijet invariant mass of $M_{jj} > 40\,\rm GeV/c^2$. A total of 18739 events passed the above cuts on the leading jets. These cuts on the leading jets produced a sample of events with approximately the same $\sqrt{\hat{s}}$ as the inclusive W sample. To avoid trigger biases in the trigger threshold region and remove QCD direct photon events, the leading jets in

[1] The CDF jet clustering is described in appendix C.

[2] the $E_T^{\rm jet}$ is determined by the sum of the transverse energies from the towers included in the jet cluster as determined by the CDF jet clustering algorithm. [61]

the control sample were not used to determine the QCD fragmentation probability. The non-leading jets were required to be in the central part of the CDF detector ($|\eta_{\rm jet}| < 1.1$); have $E_T^{\rm jet} > 5\,{\rm GeV}$ (corrected) and be well separated from either of the two leading jets ($\Delta R_{\rm jet\ jet} > 1.4$). The jets were required to be well separated so that the jet clustering cones did not overlap. A total of 11726 jets passed these requirements.

A total of 431 central electromagnetic clusters with $E_T > 5\,{\rm GeV}$ and $\Delta R > 1.4$ away from either of the two leading jets was obtained from the QCD control sample. Of these 431 CEM clusters, 266 were in a good fiducial region of the CEM detector. The CEM clusters in the QCD data were required to pass the same isolation cuts as the CEM clusters in the inclusive W data sample. A total of 64 events passed the isolation cuts. Twenty QCD events passed all of the photon selection cuts used in the selection of $W\gamma$ events.

The angular separation requirement for both the jets and the fiducial CEM clusters with respect to the leading jets ($\Delta R > 1.4$) was imposed because the size of the jet clustering cone was $\Delta R_{\rm clust}^{\rm jet} > 0.7$. Any smaller angular separation and the jet cones would have overlapped thereby biasing the number of non-leading jets. In order to accurately determine the fragmentation function of jets mimicking photons, the CEM clusters were required to have an angular separation of $\Delta R > 1.4$ with respect to the leading jets. A variation in the angular separation of $\delta(\Delta R) = \pm 0.4$ had less than a 10% impact on the overall estimate of the number of QCD fake photons in the $W\gamma$ sample. The QCD background will be calculated in the next section.

6.1.3 Determination of $W\gamma$ Background from QCD processes

The QCD jet fragmentation probability in the low-E_T region, $E_T > 5\,\mathrm{GeV}$ was determined from the use of fiducial CEM clusters passing all photon cuts and non-leading(extra) central jets ($|\eta_{\mathrm{jet}}| < 1.1$) from the QCD control sample. The QCD fragmentation probability for a given E_T bin is defined as the ratio of the number of CEM clusters passing *all* $W\gamma$ photon cuts and the number of non-leading central jets in that E_T bin. For the i^{th} E_T bin, this ratio can be written as:

$$\mathcal{P}_i^{\mathrm{QCD}}(Jet \rightarrow \text{“}\gamma\text{”}) = \frac{\mathrm{N}_i^{\text{CEM QCD}}}{\mathrm{N}_i^{\text{extra jet QCD}}} \tag{6.3}$$

The fragmentation probability distribution was quantized into discreet E_T bins due to the limited statistics associated with the number of CEM clusters in the QCD data passing all photon cuts.

Since the fragmentation probabilities in the QCD and the inclusive W samples sample are assumed to be equal, the amount of QCD fake photon background can be written as:

$$\mathrm{N}_{\gamma Bkgd}^{\text{CEM W }\gamma} = \sum_i \mathrm{N}_i^{\text{cent jet W}} \cdot \left[\frac{\mathrm{N}_i^{\text{CEM QCD}}}{\mathrm{N}_i^{\text{extra jet QCD}}}\right] \tag{6.4}$$

where the sum is over 1 GeV E_T bins from 5 GeV to 50 GeV. The total number of central jets with $E_T^{\mathrm{jet}} > 5\,\mathrm{GeV}$ in the inclusive electron W data sample is 2041. The E_T spectra for the central jets in the electron W sample is shown in the upper left histogram in Figure 6.1. The E_T spectra for the CEM clusters in the QCD control sample is in the upper right corner of Figure 6.1 and the E_T spectra for the non-leading jets in the QCD sample is in the lower right corner.

The E_T spectra for the inclusive QCD background is shown in Figure 6.2. The QCD background is sharply peaked at the threshold.

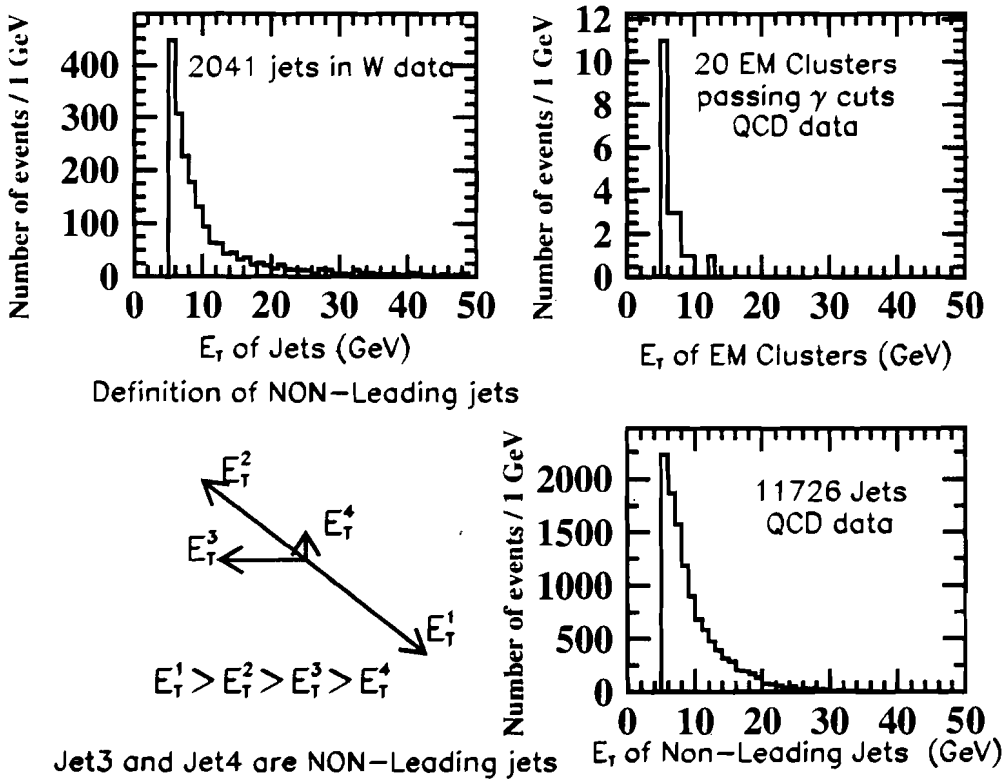

Figure 6.1: QCD fake photon background determination

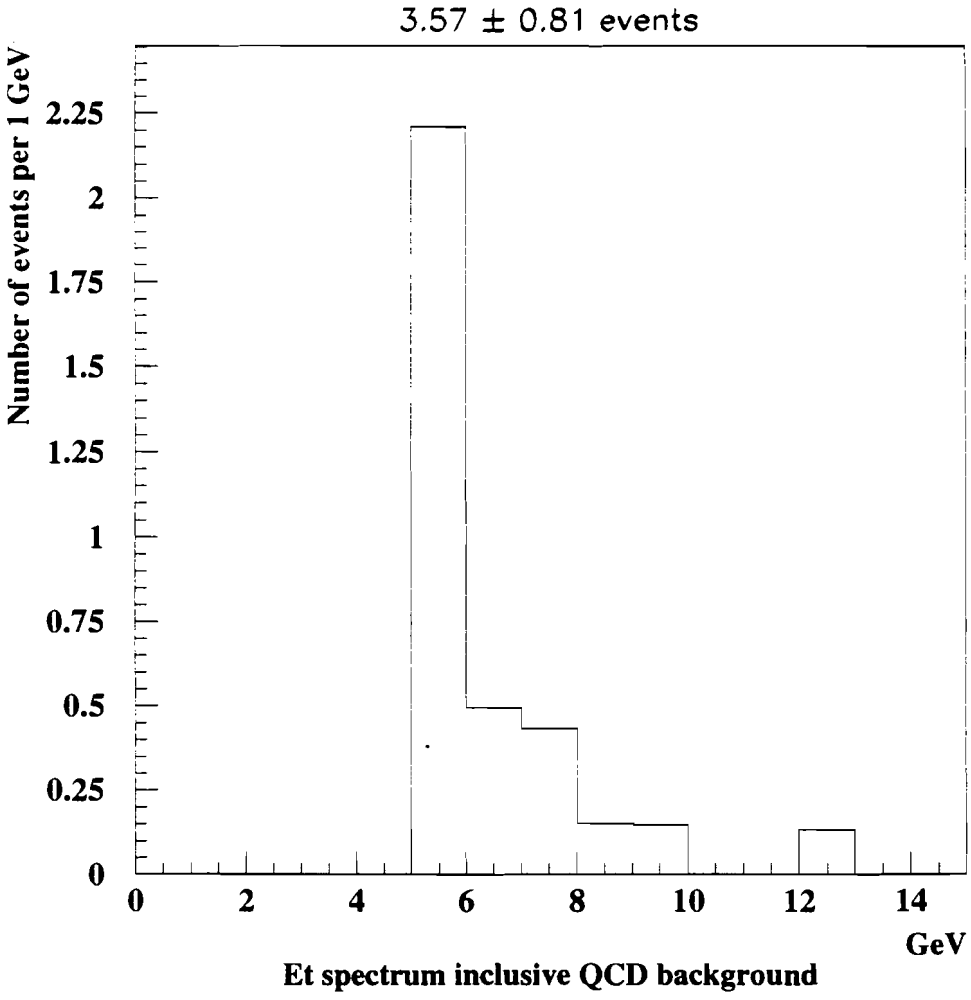

Figure 6.2: E_T spectra of QCD Background in $W\gamma$ data sample

Using equation 6.4, the QCD fake photon background for the process: $W(\rightarrow e\bar{\nu})\,\gamma$ is

$$N^{W\gamma}_{QCD\ bkgd} = 3.57 \pm 0.81 \text{ events} \tag{6.5}$$

The systematic effects on the photon background determination due to binning effects and jet energy corrections were investigated. To test binning effects, the background was calculated in two ways: 1) using 1 GeV E_T bins and 2) only *one* E_T bin. As a test of the jet energy corrections, the backgrounds were calculated using both corrected and uncorrected et energies. Table 6.1 summarizes how the background rate was affected by the E_T binning and jet energy correction systematic effects. The level of agreement between the four methods used in determining the QCD background is well within the statistical uncertainties of each method.

An independent cross-check on the level of $W(\rightarrow e\nu) + jet \rightarrow (\text{“}\gamma\text{”})$ background in the $W\gamma$ sample, was obtained from Monte Carlo simulations of inclusive electron $W + jets$ using VECBOS [46] + HERWIG [47] + the QFL Monte Carlo simulations. The VECBOS Monte Carlo program was used to generate $W(\rightarrow e\nu) + n$ Jets $(n = 0, 1, 2)$ events. The HERWIG Monte Carlo simulation was then used to generate an underlying event and to fragment the jets in events. In these events the CDF detector was simulated using QFL. The same $W\gamma$ selection criteria as the inclusive W data was applied on this properly normalized and luminosity weighted set of events. A total of 2.59 ± 0.65 events background are predicted from the VECBOS/HERWIG/QFL $W + jets(\rightarrow \text{“}\gamma\text{”})$ Monte Carlo data. The leading order calculation from the VECBOS/HERWIG/QFL Monte Carlo program agrees with the data from the electron W data sample up to a jet multiplicity of two. [10]

Table 6.1: Comparison of QCD Background Determination Methods for $W\gamma$

Method	Background Rate
Standard Method Jet Energy corrected; 1 GeV E_T bins	$N_{W+\text{Jets}}^{QCD\ bkgd} = 3.57 \pm 0.81$
Jet Energy corrected; only *ONE* E_T bin	$N_{\text{method 2}}^{QCD\ bkgd} = 3.48 \pm 0.87$
Jet Energy **NOT** corrected; 1 GeV E_T bins	$N_{\text{method 3}}^{QCD\ bkgd} = 2.92 \pm 0.67$
Jet Energy **NOT** corrected; only *ONE* E_T bin	$N_{\text{method 4}}^{QCD\ bkgd} = 3.42 \pm 0.85$
Maximum Difference between any TWO Methods	$\Delta N_{diff}^{QCD\ bkgd} = 0.65$

6.1.4 Test of QCD Fragmentation Probability

The assumption that the the QCD jet fragmentation probability is the same in the non-signal control sample *and* the inclusive electron $W/$ data sample *i.e.*

$$\mathcal{P}^{Control\ Sample}_{Jet\rightarrow\text{"}\gamma\text{"}}(E_T) \;=\; \mathcal{P}^{W}_{Jet\rightarrow\text{"}\gamma\text{"}}(E_T) \tag{6.6}$$

can be tested by comparing the QCD jet mis-identification probability distribution obtained from the QCD data sample with that obtained from the combined $e+\mu$ inclusive W data samples. The combined $e+\mu$ inclusive W data sample was used because of the limited statistics in either mode alone. The number of events from the Standard Model prediction was then subtracted from the number of observed events in the combined data sample. [3] The QCD jet fragmentation probability distribution, for the i^{th} E_T-bin, can be written as:

$$\mathcal{P}_{Jet\rightarrow\text{"}\gamma\text{"}}(E_T) \;=\; \left[\frac{\Delta N_i^{CEM\ passing\ cuts}}{\Delta N_i^{Extra\ jets}}\right] \tag{6.7}$$

The equation 6.6 is rewritten as :

$$\left[\frac{\Delta N_i^{CEM\ J20}}{\Delta N_i^{Extra\ Jet\ J20}}\right] \;=\; \left[\frac{\Delta N_{i\ \gamma\ Bkgnd}^{W}}{\Delta N_i^{Extra\ Jet\ W}}\right] \tag{6.8}$$

Table 6.2 contains the fragmentation probability for QCD jets to pass all photon cuts in both the combined $e+\mu$ inclusive W data and the QCD control sample. The QCD control sample had 20 events passing all photon cuts. The combined $e+\mu$ inclusive W data had 13 candidate events with a Standard Model prediction of 7.1 ± 0.7 events. Despite the limited statics, the agreement between the data sets is good. If a non-SM $W\gamma$ signal, as allowed by our experimental 95% CL upper limits on $\Delta\kappa$ and λ (these limits will be presented in Chapter 7), and within the E_T range $5 < E_T < 15$ GeV is subtracted out instead of the SM signal, the fractional change in the combined $e+\mu$ QCD jet fragmentation probability distribution over this E_T range is $\sim \pm 25\%$, well within statistical uncertainties.

[3] It was assumed that the $W\gamma$ signal in the data set was equal to the Standard Model prediction.

Table 6.2: QCD Jet Fragmentation Probability – All Photon Cuts

E_T Range (GeV)	$\mathcal{P}^{QCD}_{Jet\rightarrow\text{"}\gamma\text{"}}$	$\mathcal{P}^{W_{e+\mu}}_{Jet\rightarrow\text{"}\gamma\text{"}}$
$5-6$	$0.49 \pm 0.15\%$	$0.41 \pm 0.29\%$
$6-8$	$0.17 \pm 0.07\%$	$0.15 \pm 0.21\%$
$8-11$	$0.07 \pm 0.05\%$	$-0.10 \pm 0.16\%$
$11-15$	$0.06 \pm 0.06\%$	$0.58 \pm 0.53\%$
> 15	$0.00^{+0.08}_{-0.00}$ %	$0.09 \pm 0.21\%$
> 5	$0.17 \pm 0.04\%$	$0.19 \pm 0.11\%$

Another comparison of the fragmentation probability was also made. Instead of requiring the CEM clusters pass all the photon cuts; the photon selection criteria was relaxed to simply require isolated EM clusters in the QCD and combined $e + \mu$ data samples, using only the calorimeter isolation and tracking isolation cuts.

In the QCD data sample, 64 "loose" EM clusters were found. In the combined $e + \mu$ data sample there were 26 events with an expected Standard Model signal of 8.8 ± 0.8 events. Thus, any inaccuracy in the signal subtraction is diminished by approximately a factor of ~ 2, relative to the previous comparison with the full photon cuts applied. The results of the comparison using relaxed photon selection cuts are shown in Table 6.3. Again, the agreement between the two probability distributions is reasonably good.

Table 6.3: QCD Jet Fragmentation Probability – Loose Photon Cuts

E_T Range (GeV)	$\mathcal{P}^{QCD}_{Jet\rightarrow``\gamma"}$	$\mathcal{P}^{W_{e+\mu}}_{Jet\rightarrow``\gamma"}$
$5-6$	$1.35 \pm 0.27\%$	$0.97 \pm 0.53\%$
$6-8$	$0.76 \pm 0.16\%$	$0.97 \pm 0.48\%$
$8-11$	$0.18 \pm 0.10\%$	$0.19 \pm 0.40\%$
$11-15$	$0.17 \pm 0.13\%$	$1.04 \pm 0.87\%$
> 15	$0.00^{+0.07}_{-0.00}$ %	$0.07 \pm 0.21\%$
> 5	$0.55 \pm 0.07\%$	$0.57 \pm 0.11\%$

6.2 Additional Backgrounds in the $W\gamma$ Data Sample

There are two additional types of backgrounds in the $W\gamma$ data sample. The $Z\gamma$ and inclusive Z+Jet (where a QCD jet is mis-identified as photon) processes can contribute to the $W\gamma$ background. The processes $(W \rightarrow \tau\bar{\nu}_\tau) + \gamma$ and $(W \rightarrow \tau\bar{\nu}_\tau) + Jet$, where a QCD jet is mis-identified as a photon, can also contribute to the background in the $W\gamma$ data samples when the τ decays to an electron.

6.2.1 Z Backgrounds in the $W\gamma$

In order for the processes $Z(\rightarrow e^+e^-) + \gamma$ and Z+Jet (where a QCD jet is mis-identified as photon) to contribute to the $W\gamma$ background; one of the electrons from the $Z-$decay must not be detected and the event is subsequently misidentified as a W event. This can occur when one of the decay electrons passes through a non-fiducial region in the electromagnetic calorimeters (e.g. a crack).

The contribution from misidentified $Z\gamma$ events to the $W\gamma$ background was estimated by using the Baur $Z\gamma$ + "fast" Monte Carlo detector simulation programs and was cross-checked with the Baur/ISAJET/QFL $Z\gamma$ Monte Carlo simulation. The misidentified $Z\gamma$ background in the $W\gamma$ data with no other cuts applied is 0.55 ± 0.05 events.

The Z+Jet background in the $W\gamma$ data sample was determined from the "direct" QCD Z+Jet background in the electron $Z\gamma$ data sample. With no further cuts imposed, 0.11 ± 0.02 Z+Jet background events are expected in the $W\gamma$ data sample.

Contributions from $Z\gamma$ and Z+Jet backgrounds to the $W\gamma$ data sample can be additionally suppressed by making use of the track associated with the second decay electron. To reduce the Z background, events were rejected if they contained an additional, *isolated* three-dimensional track with $P_T > 10$ GeV/c with opposite charge sign to the W decay lepton and had a pair-mass (between a track and the electron) of $70 < M_{e\,track} < 110$ GeV/c^2. The tracks that are within $\Delta R < 0.7$ of a *hadronic* jet (EM fraction < 0.85) are not considered, since $W\gamma$+Jet events are *not* vetoed in this analysis. From studies using Baur/ISAJET/QFL $W\gamma$ Monte Carlo simulated data, no $W\gamma$ signal events were lost by these 2^{nd} track cuts. After making such cuts, 0.12 ± 0.02 $Z\gamma$ and 0.02 ± 0.01 Z+Jet background events remained in the $W\gamma$ data sample. This cut removed one misidentified $Z\gamma$ event in the $W\gamma$ data sample. The misidentified Z+jets data are *already* included in the inclusive QCD background determination. The misidentified Z backgrounds in $W\gamma$ are summarized in table 6.4.

6.2.2 τ Backgrounds in the $W\gamma$

The processes $(W \rightarrow \tau\bar{\nu}_\tau)+\gamma$ and $(W \rightarrow \tau\bar{\nu}_\tau)+Jet$, where a QCD jet is mis-identified as a photon, can also contribute to the background in the $W\gamma$ data sample when the τ decays to an electron. The corresponding processes $(Z \rightarrow \tau^+\tau^-) + \gamma$ and $(Z \rightarrow \tau^+\tau^-)+Jet$ can also contribute to the background in the $W\gamma$ data samples. However,

Table 6.4: Summary of Misidentified Z backgrounds in $W\gamma$ data sample

	no "2^{nd} track cut"	"2^{nd} track cut" applied
$Z + \gamma$	0.55 ± 0.05	0.12 ± 0.02
$Z +$ Jet ($\rightarrow$ "γ")	0.11 ± 0.02	0.02 ± 0.01

because of the additional tau branching ratio factor, $B(\tau \rightarrow e\ \bar{\nu}_e\ \nu_\tau) \simeq 17.8\%$ [48] and the three-body nature of the tau decay (softening the final-state lepton P_T and $\not\!\!E_T$ spectrum), these background contributions to $W\gamma$ are suppressed. The tau $W\gamma$ backgrounds were determined with the use of the Baur $W\gamma$ and "fast" Monte Carlo detector simulation programs, and the same methodology that was used for the determination of the $W\gamma$ signal.

The tau decay contribution to the $W\gamma$ background was found to be small; 0.11 ± 0.01 events. The tau decay contribution to the W+Jet background sample was also found to be small; 0.08 ± 0.01 events. This background is *already* included in the inclusive QCD background determination for the $W\gamma$ data samples.

The tau decay contribution to the $Z\gamma$ background in $W\gamma$ data sets was calculated via similar methods as those used for determining the "direct" $Z\gamma$ background. This non-QCD background contribution to the $W\gamma$ data samples was found to be extremely small ($<<$ 0.1 events), and is neglected.

The tau decay contribution to the inclusive Z+Jet background in the $W\gamma$ data set was calculated via similar methods as those used for determining the *direct* Z+Jet background. These background contributions were also found to be extremely small ($<<$ 0.1 events), and are also neglected.

Table 6.5: Comparison of QCD Background for $W\gamma$

Inclusive W + Jets data	$N_{W+\text{Jets}}^{QCD\,bkgd} = 3.57 \pm 0.81$	
VECBOS $W(\rightarrow e\nu)$ + Jets		$N_{\text{Vecbos}}^{QCD\,bkgd} = 2.59 \pm 0.65$
Z +Jet $\rightarrow$ "W" + "γ"		$N_{Z+\text{Jets}}^{QCD\,bkgd} = 0.02 \pm 0.01$
$W^{\tau\rightarrow e}$ +jet $\rightarrow W^{\tau\rightarrow e}$ + "γ"		$N_{\tau+\text{Jets}}^{QCD\,bkgd} = 0.08 \pm 0.02$
	Sub-total:	$N_{\text{subtotal}}^{QCD\,bkgd} = 2.69$
$\Delta N_{diff}^{W+\text{Jets}} = N_{W+\text{Jets}}^{QCD\,bkgd} - N_{\text{subtotal}}^{QCD\,bkgd} = 0.88$		

Table 6.6: Summary of Background for $W\gamma$

Background		
QCD:	Inclusive W + Jets data	3.57 ± 0.81
non-QCD:	$Z + \gamma \rightarrow$ "W" + γ	0.12 ± 0.02
	$W^{\tau\rightarrow e} + \gamma$	0.11 ± 0.01
Total:		$N_{bkgd}^{W\gamma} = 3.8 \pm 0.8(stat) \pm 1.1(syst)$

6.3 Summary of Backgrounds

Table 6.5 compares the inclusive W + jets background to the $W(\rightarrow e\nu)$+ jets derived from the VECBOS/HERWIG/QFL Monte Carlo simulation, Z + jet background in $W\gamma$ data sample and τ + jets background in the $W\gamma$.

The backgrounds for $W\gamma$ are summarized in table 6.6. The total background in the $W\gamma$ data sample is

$$N_{bkgd}^{W\gamma} = 3.8 \pm 0.8(stat) \pm 1.1(syst) \tag{6.9}$$

The first uncertainty in the total background in $W\gamma$ events is statistical. The

second uncertainty is the systematic uncertainty associated with the photon background.

The systematic uncertainty on the inclusive QCD jet background is (conservatively) defined as the quadrature sum of: (a) the *maximum* difference between the four different methods used in determining the inclusive QCD jet backgrounds, as summarized in Table 6.1 $\Delta\mathcal{N}_{diff}^{QCD\ bkgd}$, and (b) the *difference* between the inclusive QCD jet background and the sum of (1) the "direct" QCD jet background as determined by the VECBOS/HERWIG/QFL $W/Z+n-$jets MC simulations plus (2) the "indirect" QCD jet background contributions, which for $W\gamma$ are due to Z+Jet and tau W+Jet processes,$\Delta\mathcal{N}_{diff}^{W+\mathrm{Jets}}$. The "indirect" QCD jet background contribution for $Z\gamma$ is due to tau Z+Jet, which is negligible. This systematic uncertainty can be written as:

$$\Delta\mathcal{N}_{syst.\ error}^{W\gamma\ bkgd} = \sqrt{\left(\Delta\mathcal{N}_{diff}^{QCD\ bkgd}\right)^2 + \left(\Delta\mathcal{N}_{diff}^{W+\mathrm{Jets}}\right)^2} \qquad (6.10)$$

Chapter 7
Experimental results

This chapter is divided into three sections. The first section presents the experimental cross section times branching ratio results for $W\ (\rightarrow\ e\,\nu) + \gamma$. The next two sections give limits on the anomalous $W\gamma$ couplings , κ and λ and the electromagnetic moments of the W boson, respectively.

7.1 Experimental Cross Section times Branching Ratio Results

The experiment determination of the cross section times branching ratio is presented in this section. Section 7.1.1 contains the method for the determination of the cross section times branching ratio. The systematic effects of varying the diboson $P_T(W+\gamma)$ distribution, the structure function choice and Q^2 dependence of the nominal structure function (HMRS-B [40]) are described in section 7.1.2. The experimental cross section times branching ratio results are presented in section 7.1.3.

7.1.1 General Methodology

The experimental results for the production cross section times branching ratio for $W\gamma$ were determined using the equation

$$\sigma \cdot B(W+\gamma) \;=\; \frac{\mathcal{N}_{sig}^{W\gamma}}{\int \mathcal{L}dt \cdot (A_{W\gamma} \cdot \epsilon_{W\gamma})} \;=\; \frac{\mathcal{N}_{obs}^{W\gamma} - \Sigma\mathcal{N}_{bkg}^{W\gamma}}{\int \mathcal{L}dt \cdot (A_{W\gamma} \cdot \epsilon_{W\gamma})} \qquad (7.1)$$

The terms in equation 7.1, observed number of events, the total background, the

Table 7.1: Summary of $W\gamma$ Results

N_{obs}	8
ΣN_{bkgnd}	$3.8 \pm 0.8(stat) \pm 1.1(syst)$
N_{signal}	$4.2 \pm 2.9(stat) \pm 1.1(syst)$
N_{pred}^{SM}	4.6 ± 0.4
$\int \mathcal{L}dt$	$4.05 \pm 0.28\ pb^{-1}$
$(A_{W\gamma} \cdot \epsilon_{W\gamma})$	$6.0 \pm 0.2\%$

number of signal events, the number of events predicted by the Standard Model, overall acceptance times efficiency for selecting $W\gamma$ events and the integrated luminosity, were all derived in previous chapters. These terms are all listed in table 7.1 with one exception: the systematic uncertainty of the acceptance terms derived from the Baur $W\gamma$ Monte Carlo program due to variation of the $W\gamma$ P_T spectrum, choice of structure functions and Q^2 dependence of the nominal structure function. This systematic uncertainty will be discussed in section 7.1.2.

A Monte Carlo program was used to combine the statistical and systematic uncertainties associated with measurement of $\sigma \cdot B(W + \gamma)$ and thus determined the overall uncertainties (confidence levels) of the experimental $\sigma \cdot B(W + \gamma)$ result. The Monte Carlo $\sigma \cdot B(W + \gamma)$ program simulated 10^6 CDF "experiments". The number of observed events were fluctuated according to Poisson statistics. The integrated luminosity, acceptance and efficiency terms were all fluctuated according to Gaussian statistics. The statistical and systematic uncertainties associated with the individual backgrounds were Gaussian fluctuated and subtracted from the observed number of events on a "experiment by experiment" basis. The experimental cross section

$\sigma \cdot B(W+\gamma)_{exp}$ was calculated from a finely binned histogram with one entry per "experiment". The mean and $\pm 1\,\sigma$ (double sided) uncertainties for $\sigma \cdot B(W+\gamma)_{exp}$ were obtained from the histogram. Also the 68.3% , 90.0% and 95.0% single-sided CL upper limits of $\sigma \cdot B(W+\gamma)_{exp}$ were obtained using the Particle Data Group's (PDG) method for a bound physical region. [49] The experimental cross section times branching ratio result for $W\gamma$ is summarized in table 7.3. The first uncertainty is statistical. The second uncertainty is associated with the uncertainties in the integrated luminosity, acceptances and efficiencies. The systematic uncertainty associated with the QCD background determination is listed third.

Figure 7.1 shows the $\sigma \cdot B(W\gamma)$ probability distributions. These distributions are nearly Gaussian, but with a small high-side tail due mainly to small number Poisson statistics associated with the number of events observed.

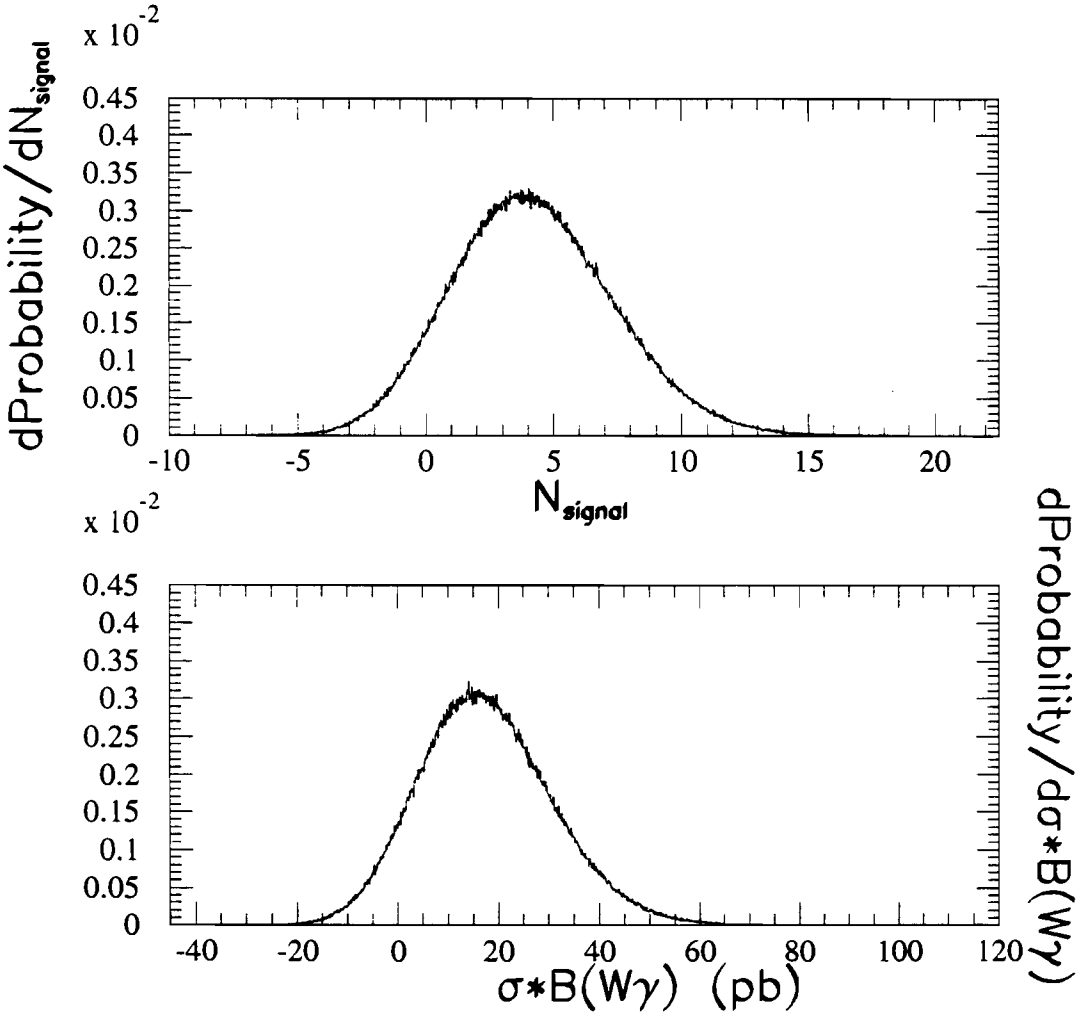

Figure 7.1: $N_{signal}^{W\gamma}$ and $\sigma \cdot B(W\gamma)$ probability distributions

7.1.2 Additional Systematic Uncertainties on $\sigma \cdot B(W+\gamma)$

The systematic effects of varying the diboson $P_T(W+\gamma)$ distribution, structure function (SF) choice and the Q^2-scale dependence for the nominal structure function (HMRS-B) choice on the determination of $\sigma \cdot B(W+\gamma)$ were studied and presented in table 7.3. These systematic effects on the calculation of $\sigma \cdot B(W+\gamma)$ are manifested by an uncertainty in the acceptance terms determined by the Baur $W\gamma$ Monte Carlo program. The systematic effects of varying the CEM energy scale and CEM energy resolution were also investigated and found to have negligible impact on the Monte Carlo acceptance determination.

Systematic Uncertainties due to $P_T(W+\gamma)$

Since there are as yet no experimental measurements of the diboson $P_T(W+\gamma)$ spectrum, and no theoretical prediction for the distribution in the low $P_T(W+\gamma)$ region (below $\sim$ 10 GeV/c), the measured CDF $P_T(W)$ distribution [50] was used to approximate the $P_T(W+\gamma)$ distribution in the Monte Carlo simulation program. The CDF $P_T(W)$ distribution was a reasonable assumption for the $P_T(W+\gamma)$ distribution because the shape of the $P_T(W+\gamma)$ distribution is expected to be similar to $P_T(W)$ for the $W\gamma$ event selection cuts used in this analysis. The measured $d\sigma/dP_T(W)$ distributions for inclusive W production is in good agreement with theoretical predictions [51]. The systematic effects of varying the shape of the assumed $P_T(W+\gamma)$ distribution on the W/photon acceptances were studied.

The Monte Carlo diboson $P_T(W+\gamma)$ distribution was varied within the $\pm 1\sigma$ limits allowed by the fit to the $d\sigma/dP_T(W)$ distribution. The method used the fast Monte Carlo detector simulation programs to obtain the Monte Carlo $\sigma \cdot B(W+\gamma)_{MC}$ and all kinematic/geometrical acceptances. The acceptance results for each $P_T(W+\gamma)$ choice, were then used, along with the efficiencies for all cuts, to determine the the experimental $\sigma \cdot B(W+\gamma)_{exp}$ result.

Four $P_T(W+\gamma)$ distributions for each decay channel were investigated to obtain acceptance factors used in the determination of both Monte Carlo and experimental $\sigma \cdot B(W+\gamma)$ results, associated with: (1) "no" P_T boost, (2) a "soft" (-1σ) P_T boost, (3) a "nominal" P_T boost and (4) a "hard" $(+1\sigma)$ P_T boost. The systematic error associated with variation in the P_T of the $W\gamma$ system is summarized in table 7.2. The "no" P_T boost study was included solely for relative comparison purposes, and is *not* used in the determination of the systematic uncertainty due to the $P_T(W+\gamma)$ spectrum.

Systematic Uncertainties due to Structure Function Q^2 Scale Dependence

The systematic uncertainties associated with the Q^2-scale dependence for the nominal structure function choice (HMRS-B) were studied by varying the Q^2-scale between the limits $\frac{1}{4}M^2_{W+\gamma} < Q^2 < 4M^2_{W+\gamma}$. The possible correlations between Q^2-scale dependence and the shape of the diboson $P_T(W+\gamma)$ distribution were neglected. The Q^2-scale dependence and the shape of the diboson $P_T(W+\gamma)$ are correlated with each other due to four-momentum conservation in the $W+\gamma$ production process. Hence treating these two effects as independent of each other will tend to over-estimate the sensitivity to these effects. The systematic error due to the structure function Q^2 - scale dependence is is summarized in table 7.2.

Systematic Uncertainties due to Structure Function Choice

The systematic uncertainty associated with the choice of structure functions was investigated using five different structure function (SF) choices (DFLM-260 [52], MRS-B [53], HMRS-B [40], MRS-S0 [54] and MT-B1 [55]). The Baur $W\gamma$ Monte Carlo events were analyzed using the fast Monte Carlo detector simulation programs to obtain Monte Carlo $\sigma \cdot B(W+\gamma)_{MC}$ and kinematic/geometrical acceptance results. This systematic uncertainty is summarized in table 7.2.

Systematic Uncertainties due to Energy Scale and Resolution

The calibration of the CEM energy scale over the energy range $5 < E_T < 40$ GeV is determined from E/P studies using inclusive electrons in the low-energy range and electrons from W decay in the high energy range. The CEM energy scale in the 5 GeV region is correct to within $\sim$ 1.0% and in the 40 GeV region it is correct to within $\pm 0.24\%$ [27]. This level of uncertainty has a negligible impact on the observed and/or predicted number of $W\gamma$ events, and the Monte Carlo predicted and/or experimental cross sections.

Similarly, the effect of $\pm 1\sigma$ variations of the stochastic and constant terms associated with the CEM calorimeter energy resolution,

$$\delta E/E \;=\; (13.5 \pm 1.5)\%/\sqrt{E_T} \;\ominus\; (2.0 \pm 0.3)\% \quad (E \text{ in GeV}) \tag{7.2}$$

also has a negligible impact on the observed and/or predicted number of $W\gamma$ events and the Monte Carlo predicted and/or experimental cross sections for $E_T^\gamma > 5$ GeV.

Summary of $P_T \ominus Q^2 \oplus SF$ Systematic Uncertainties

The Monte Carlo and experimental $\sigma \cdot B(W + \gamma)$ cross section results must include the contributions to the uncertainty in the acceptance from these three systematic uncertainties: P_T; Q^2 and structure function choice. These systematic uncertainties were added in quadrature to the systematic uncertainty of the acceptance terms determined by the Baur $W\gamma$ Monte Carlo program. The individual systematic uncertainties and the combined (in quadrature) systematic uncertainties for the Monte Carlo, experimental and Monte Carlo - experimental difference cross section results are summarized in table 7.2.

7.1.3 Summary of $W\gamma$ Cross Section Result

The $W\gamma$ cross section times branching ratio result and Standard Model prediction explicitly taking into account the $P_T(W + \gamma)$, Q^2- scale dependence and structure

Table 7.2: The variations (measured in pb) of the Monte Carlo and Experimental Cross Section times Branching Ratio values due to variations in the Diboson P_T spectrum, Structure Function choice and Q^2 dependence of the nominal structure function (HMRS-B)

Quantity	$\Delta\sigma \cdot B(W+\gamma)_{MC}$ (pb)	$\Delta\sigma \cdot B(W+\gamma)_{Exp}$ (pb)
P_T	$^{+2.2}_{-0.5}$	$^{+1.1}_{-0.7}$
Q^2	$^{+1.1}_{-0.3}$	$^{+0.8}_{-0.3}$
$StructureFunction$	$^{+3.3}_{-1.0}$	$^{+0.7}_{-0.6}$
$P_T \oplus Q^2 \oplus SF$	$^{+4.1}_{-1.2}$	$^{+1.5}_{-1.0}$

function systematic uncertainties are summarized below.

$$\sigma \cdot B(W\gamma) = 17.0^{+13.7}_{-13.4}\ (stat + syst)\ \text{pb} \tag{7.3}$$

$$\sigma \cdot B(W\gamma)_{SM} = 19.0\ ^{+3.3}_{-0.9}\ (stat + syst)\ \text{pb} \tag{7.4}$$

While the experimental cross section result is in good agreement with the Standard Model prediction, because of the non-negligible correlations between the Monte Carlo predicted $\sigma \cdot B(W+\gamma)_{MC}$ and the experimental cross section $\sigma \cdot B(W+\gamma)_{exp}$, the results presented in this section cannot be used for determination of limits on the $\Delta\kappa$ and λ anomalous parameters for $W\gamma$. The acceptance factors determined from the Baur $W\gamma$ Monte Carlo program are used in the calculation of **both** the Monte Carlo $\sigma \cdot B(W+\gamma)_{cuts}$ and the experimental $\sigma \cdot B(W+\gamma)_{exp}$ cross sections.

These results were cross-checked with a first principles analytical calculation of $\sigma \cdot B(W\gamma)$ and the associated $\pm 1\,\sigma$ uncertainties. There is good agreement between both results.

Table 7.3: Experimental $\sigma \cdot B(W\gamma)$ Results

	$\sigma \cdot B(W+\gamma)_{exp}$ (pb)	$\sigma \cdot B(W+\gamma)^{SM}_{pred}$ (pb)
68.3% $DS\ CL$	$17.0^{+12.0}_{-12.0}\ ^{+1.5}_{-1.3}\ ^{+4.5}_{-4.6} = 17.0^{+13.6}_{-13.4}$	$19.0^{+3.3}_{-0.9}$
68.3% $SS\ CL$	< 24.3	
90.0% $SS\ CL$	< 35.8	
95.0% $SS\ CL$	< 41.3	
where DS - double sided and SS - single sided		

7.2 Limits on Anomalous Couplings for $W\gamma$

7.2.1 General Methodology

If the W boson is a composite object, then large values of anomalous $WW\gamma$ couplings ($>> \alpha$) may be realized in nature. For $W\gamma$, the destructive interference between the various Feynman graphs associated with the $W\gamma$ process (see figure 2.1) rapidly disappears for such non-Standard Model couplings. Depending on the nature and magnitude of these non-standard couplings, an excess of isolated, high$-E_T$ photons accompanying the production of W bosons is expected, relative to SM $W\gamma$ prediction. The angular distribution for hard photons associated with non-standard anomalous couplings is more central ($|\eta_\gamma| < 1.1$) than for the Standard Model $W\gamma$ process [17]. The number of $W\gamma$ events predicted by the Baur + fast Monte Carlo $W\gamma$ simulation for several choices of the anomalous parameters, $\Delta\kappa$ andλ is summarized in table 7.4. The uncertainties in table 7.4 are statistical only.

Figure 7.2 shows the E_T^γ spectrum of the central ($|\eta_\gamma| < 1.1$) photons predicted by the Baur Monte Carlo program for several different choices of $\Delta\kappa$ and λ. The angular separation between the electron and photon ($\Delta R_{e\gamma}$) for various choices of $\Delta\kappa$ and λ is shown in figure 7.3. The experimental sensitivity to possible anomalous

Table 7.4: Monte Carlo prediction for Number of $W\gamma$ events

Anomalous Coupling	$E_T > 5$ GeV	$5 < E_T \leq 15$ GeV	$E_T > 15$ GeV
$\Delta\kappa = 0,\ \lambda = 0$ (SM)	4.6 ± 0.4	3.7 ± 0.3	0.9 ± 0.1
$\Delta\kappa = 7,\ \lambda = 0$	11.0 ± 1.0	4.6 ± 0.4	6.4 ± 0.6
$\Delta\kappa = 0,\ \lambda = 3$	12.6 ± 1.2	3.9 ± 0.4	8.7 ± 0.8
$\Delta\kappa = 5,\ \lambda = 5$	39.5 ± 3.6	5.5 ± 0.5	34.0 ± 3.2

$WW\gamma$ couplings for $W\gamma$ is determined by the *absence* of an excess of events at high E_T^γ, or, equivalently by obtaining an upper limit on the experimental cross section.

The experimental 68.3%, 90.0% and 95.0% CL upper limits on the ($\Delta\kappa$, λ) parameters for $W\gamma$ were determined by using the Baur $W\gamma$ Monte Carlo programs to step through a matrix of anomalous ($\Delta\kappa$, λ) parameters. The Baur Monte Carlo $W\gamma$ four-vector data for each pair of anomalous coupling parameters was then analyzed using the fast $W\gamma$ MC detector simulation program. The Monte Carlo $\sigma \cdot B(W + \gamma)_{MC}$ cross section, all kinematic/geometrical acceptances and the predicted number of Monte Carlo events passing all cuts for each cross section point in the $\Delta\kappa - \lambda$ plane were recorded. This included recording *all* statistical uncertainties associated with these variables. The Baur MC was run with non-zero values of anomalous parameters with a compositeness Λ_W scale of $\Lambda_W = 10$ TeV. The $W\gamma$ cross section results differ negligibly if a compositeness scale $\Lambda_W = 1$ TeV is chosen, simply because the parton SF luminosities (for Bjorken-x of $x \sim 0.5$) contribute negligibly to the overall $W\gamma$ cross section at our center-of-mass energy.

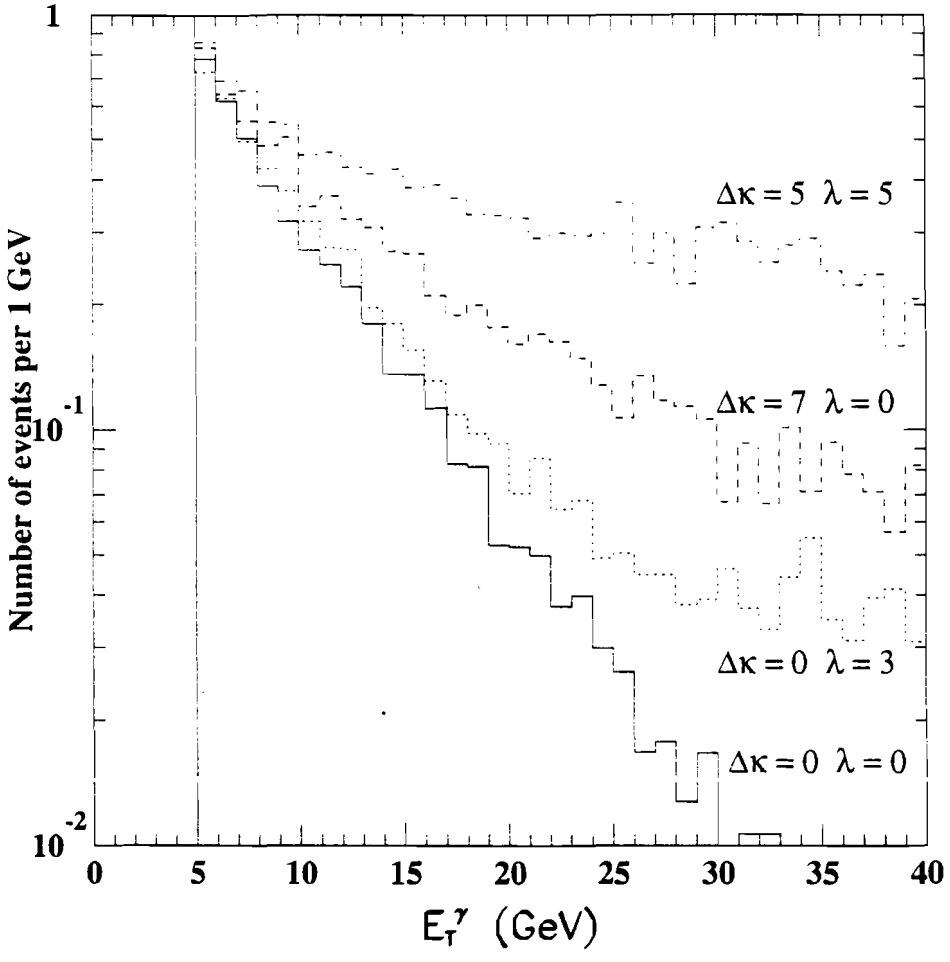

Figure 7.2: E_T^γ spectra for various $\Delta\kappa$ and λ choices

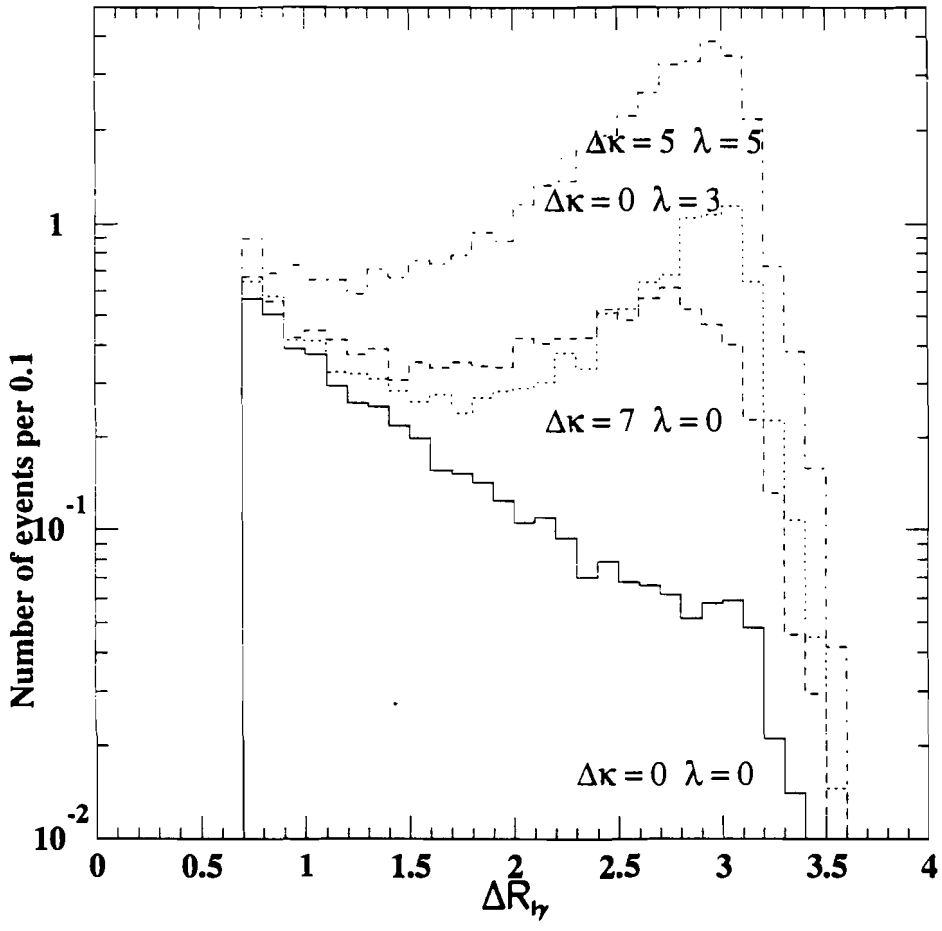

Figure 7.3: $\Delta R_{e\gamma}$ spectra for various $\Delta\kappa$ and λ choices

The matrix of Monte Carlo $\sigma \cdot B(W+\gamma)_{MC}$ data points was then fit using MINUIT [57] to obtain a three-dimensional analytic description of the $\sigma \cdot B(W+\gamma)$ cross section "surface" in the $\Delta\kappa - \lambda$ plane. The generic form of the parameterization used in fitting a particular cross section "surface" is given by:

$$\sigma(x,y) = \sigma_{SM} + ax + bx^2 + cy + dy^2 + exy \qquad (7.5)$$

where $x = \Delta\kappa$ and $y = \lambda$. No higher-order terms in x, y are needed, because the invariant amplitudes $\mathcal{M}_{W\gamma}$ containing the anomalous contributions to the $W\gamma$ processes are *linear* in their anomalous parameters: $\Delta\kappa$ and λ. The terms in the expression given above that are linear in x, y are due to interference between the various amplitudes associated with the $W\gamma$ processes. If there were no interference, the expression for the cross section would be an equation describing the surface of an elliptic paraboloid. The MINUIT fits to each data set returned the fitted values of the parameters σ_{SM}, $a-e$ and their uncertainties. The largest fit residuals were associated with the extreme values of anomalous parameters, well away from the region of interest - the SM and the 90-95% CL regions. The functional form of the cross section as derived from MINUIT is:

$$\begin{aligned} \sigma \cdot B(\Delta\kappa,\lambda)_{W\gamma} \quad &= 18.80 - 0.18\Delta\kappa + 0.41(\Delta\kappa)^2 \\ &+ 0.06\lambda + 1.90\lambda^2 + 0.88(\Delta\kappa\cdot\lambda) \quad \text{(pb)} \end{aligned} \qquad (7.6)$$

The systematic uncertainties associated with $\sigma \cdot B(W\gamma)$ must be used when determining the 68.3%, 90.0% and 95.0% CL upper limits on anomalous $WW\gamma$ couplings. These limits were derived by comparing the Monte Carlo prediction $\sigma \cdot B(W\gamma)_{MC}$ with the experimental result $\sigma \cdot B(W\gamma)_{exp}$. *However*, the Monte Carlo result is correlated with the experimental result; because the acceptance terms, used in the derivation of the cross section, are common to both results. Therefore,

in order to measure the upper limits on the anomalous parameters ($\Delta\kappa$,λ), it is important to use the *relative* overall systematic uncertainties associated with both the Monte Carlo cross section and the experimental cross section. This relative uncertainty, $\Delta\sigma \cdot B(E+\gamma)^{overall}_{MC-expt}$, is the quadrature sum of (a) the statistical uncertainty associated with the determination of the MC cross section prediction (typically $\sim$ 0.5%) and (b) the systematic uncertainty *differences* associated with (1) the diboson $P_T(W+\gamma)$ distribution, (2) Q^2-scale dependence of the nominal structure function and (3) Structure Function choice. These *relative* systematic uncertainties are summarized in table 7.5. In order to set conservative upper limits on the anomalous parameters, the analytic expression obtained from the MINUIT fit of the Baur $W\gamma$ Monte Carlo $\sigma \cdot B(W+\gamma)_{MC}$ cross section "surface" (equation 7.6) is then shifted relative to its nominal central value by $-\Delta\sigma \cdot B(W+\gamma)^{overall}_{MC-expt}$. The intersection of the *planes* containing the 68.3%, 90.0% or 95.0% CL upper limit on the experimental $\sigma \cdot B(W+\gamma)_{exp}$ with the -1σ shifted MC $\sigma \cdot B(W+\gamma)_{MC}$ "surface" determines the limits on $\Delta\kappa$, λ parameters for $W\gamma$. The intersection of the planes with the Monte Carlo cross section "surface" also form contours of $\Delta\kappa$, λ.

The *relative* systematic uncertainties due to: the $W\gamma$ P_T spectrum; structure function choice and Q^2 dependence of the nominal structure function (HMRS-B), were derived from the comparison of the the Monte Carlo and experimental cross section times branching ratio values. As an example of how the relative systematic uncertainties were determined, the uncertainty due to structure function choice will be described. As mentioned in section 7.1.2, the effect of five different structure functions (DFLM-260, MRS-B, MRS-S0, MT-B1 and the nominal structure function, HMRS-B) on the value of $\sigma \cdot B(W\gamma)$ for both the data and Monte Carlo was investigated. The $\sigma \cdot B(W\gamma)$ was calculated for both the Standard Model prediction (MC) and the experimental prediction using different structure functions. (Note - the $W\gamma$ acceptance differed with the structure function choice; see equation 7.1 in this chapter and section 5.1 in chapter 5). The difference between the Standard Model

$\sigma \cdot B(W\gamma)_{MC}$ and experimental $\sigma \cdot B(W\gamma)_{exp}$ using the nominal structure function choice was determined, $\Delta(\sigma \cdot B(W\gamma))^{\circ}_{MC-exp}$. This quantity, $\Delta(\sigma \cdot B(W\gamma))^{\circ}_{MC-exp}$, was subtracted from the difference, $\sigma \cdot B_{MC} - \sigma \cdot B_{exp}$, derived from the structure function i to determine $\Delta\sigma^{i}_{MC-exp}$. The relative systematic uncertainty was chosen to be the spread in the quantities $\Delta\sigma^{i}_{MC-exp}$ about 0.

Table 7.5: The *RELATIVE* variation (measured in *pb*) between the Monte Carlo and Experimental Cross Section times Branching Ratio values due to variations in the Diboson P_T spectrum, Structure Function choice and Q^2 dependence of the nominal structure function (HMRS-B)

Quantity	$\Delta\sigma \cdot B(W+\gamma)_{MC-Expt}$ (pb)
P_T	$^{+1.2}_{-0.2}$
Q^2	$^{+0.7}_{-0.4}$
SF	$^{+2.6}_{-0.3}$
$P_T \oplus Q^2 \oplus SF$	$^{+2.9}_{-0.5}$

7.2.2 Limits on Anomalous $WW\gamma$ Couplings

The 68.3%, 90.0% and 95.0% CL limits on the $\Delta\kappa = \kappa - 1$ and λ parameters are summarized in table 7.6.

The projection of the $W\gamma$ cross section on $\Delta\kappa$ axis is shown in figure 7.4; the projection on the λ axis is shown in figure 7.5. The central value of the curve (denoted by a solid line) represent the projection for the "surface" derived from the MINUIT fit; the dashed curves are the combined systematic and statistical uncertainties. The systematic uncertainty includes the overall systematic uncertainty *difference* between the Monte Carlo prediction and the experimental result, $\Delta\sigma \cdot B(E+\gamma)^{overall}_{MC-expt}$, as discussed previously. The central value of experimental cross section result is shown as a solid horizontal line in each figure. The $\pm 1\sigma$ (stat+syst) (68% double-sided CL)

Table 7.6: $W\gamma$ $\Delta\kappa$ and λ Limits

Parameter	CL Range	Limits
$\Delta\kappa$	68.3% *DS CL*	$0.0^{+5.0}_{-4.5}(stat) \pm 0.7(syst) = 0.0^{+5.7}_{-5.2}(stat+syst)$
	68.3% *SS CL*	$-3.5 < \Delta\kappa < +3.9$
$(\lambda = 0)$	90.0% *SS CL*	$-6.3 < \Delta\kappa < +6.7$
	95.0% *SS CL*	$-7.2 < \Delta\kappa < +7.7$
λ	68.3% *DS CL*	$0.0^{+2.2}_{-2.2}(stat) \pm 0.3(syst) = 0.0^{+2.5}_{-2.5}(stat+syst)$
	68.3% *SS CL*	$-1.7 < \lambda < +1.7$
$(\Delta\kappa = 0)$	90.0% *SS CL*	$-3.0 < \lambda < +3.0$
	95.0% *SS CL*	$-3.5 < \lambda < +3.4$

uncertainties are shown as dotted horizontal lines. The 90.0% and 95.0% single-sided CL upper limits to the experimental cross section are shown as a horizontal dashed line and a horizontal solid line, respectively.

The 68.3%, 90.0% and 95.0% single-sided CL contours in the $\Delta\kappa - \lambda$ plane are shown in figure 7.6. Note that there exist possible non-SM values of $\Delta\kappa$ and λ where the magnetic dipole moment μ_W and/or the electric quadrupole moment Q_W of the W boson vanish separately:

$$\mu_W = 0: \quad \lambda = -(\Delta\kappa + 2) \tag{7.7}$$

$$Q_W = 0: \quad \lambda = (\Delta\kappa - 1). \tag{7.8}$$

Also, there is one point, $(\Delta\kappa, \lambda) = (-\frac{3}{2}, -\frac{1}{2})$, where both quantities vanish simultaneously. This point is contained within the experimental 68.3% CL limit contour. Note also the displacement of the location of the minimum of the $\sigma \cdot B(W+\gamma)$ cross section "surface" relative to the SM value (and $\mu_W = 0$, $Q_W = 0$ point). Note further the relative orientation of the contour limits in the $\Delta\kappa - \lambda$

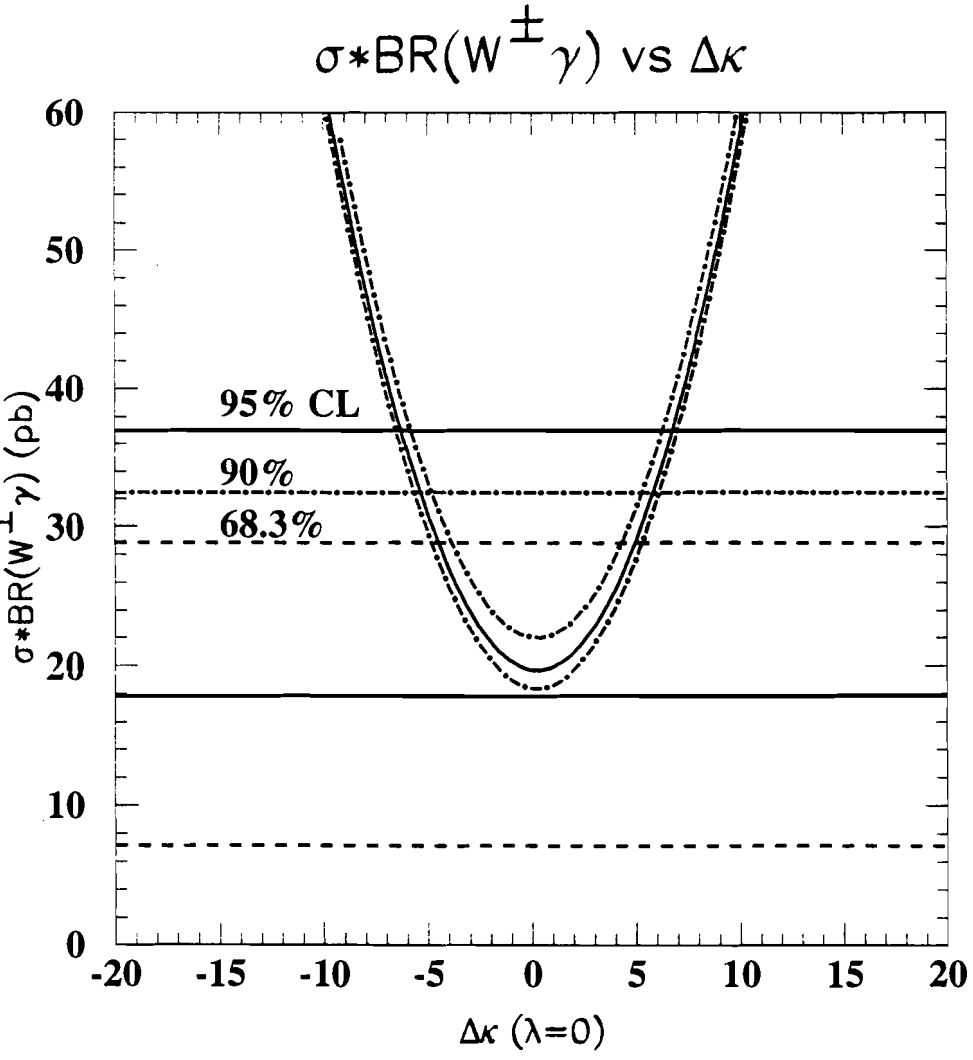

Figure 7.4: Projection of the $W\gamma$ cross section on the $\Delta\kappa$ axis

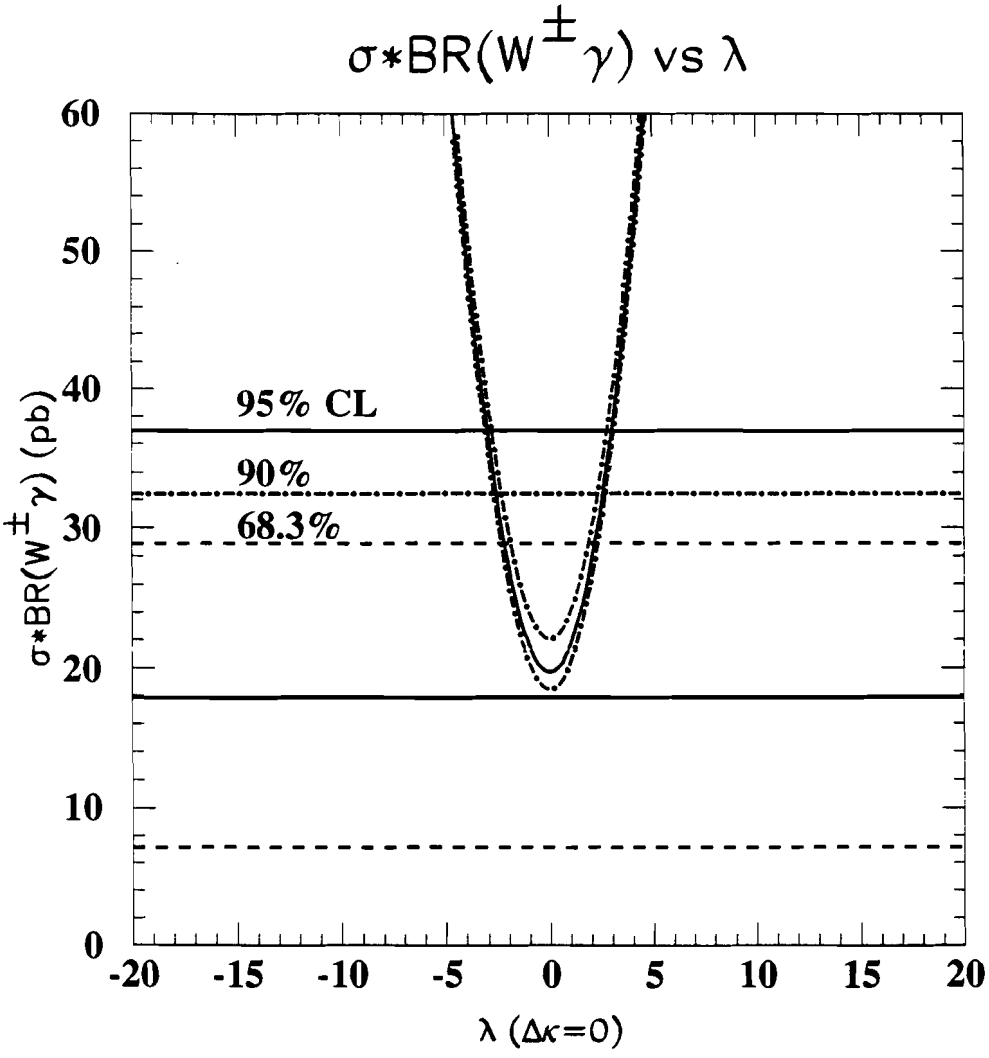

Figure 7.5: Projection of the $W\gamma$ cross section on the λ axis

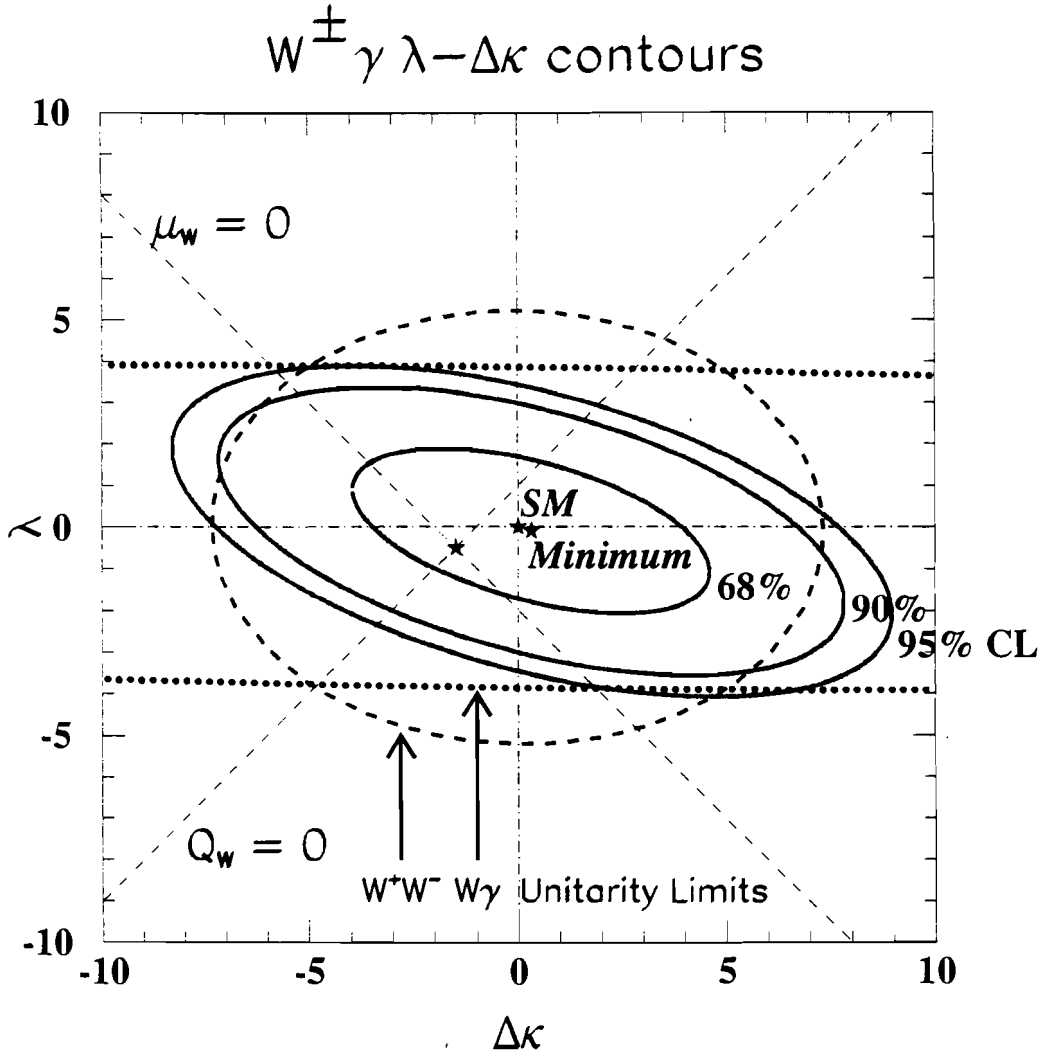

Figure 7.6: $W\gamma$ Cross Section Contours in $\Delta\kappa$ and λ plane

plane with respect to the $\Delta\kappa$ and λ axes, indicating the degree of interference effects present between these two anomalous parameters at our $\sqrt{s}$ CM energy.

7.3 Unitarity Constraints for $W\gamma$ – Compositeness Scale Λ_W Sensitivity

Partial wave unitarity places restrictions on the reduced amplitudes, $A^W_{\lambda_W\lambda_\gamma}$ for arbitrary values of $\Delta\kappa$ and λ for anomalous $WW\gamma$ couplings. There are two such unitarity restrictions, one associated with $W+\gamma$ production and another associated with W^+W^- production. For $W+\gamma$ production, the unitarity restriction is [15, 18]:

$$\sum_{\lambda_W\lambda_\gamma}\left|A^W_{\lambda_W\lambda_\gamma}\right|^2 < \frac{3\sin^2\theta_W}{\alpha^2(\hat{s})\left(1-\frac{M_W^2}{\hat{s}}\right)} \tag{7.9}$$

where λ_W, λ_γ are the final-state W boson and photon helicities, respectively. For the assumed generalized dipole form factor and form factor power ($n=2$), unitarity is violated in the $W+\gamma$ process if

$$\frac{(\frac{\hat{s}}{M_W^2}-1)}{(1+\frac{\hat{s}}{\Lambda_W^2})^4}\left[(\Delta\kappa+\lambda)^2+\left(\frac{\hat{s}}{M_W^2}\right)\left(\Delta\kappa\left(\frac{M_W^2}{\hat{s}}\right)+\lambda\right)^2\right] \geq \frac{6\sin^2\theta_W}{\alpha^2(\hat{s})} \tag{7.10}$$

over the $\sqrt{\hat{s}}$ range $M_W < \sqrt{\hat{s}} < 1.8$ TeV. For W^+W^- production, the unitarity restriction is [15, 18]:

$$\sum_{\lambda_{W+}\lambda_{W-}}\left|A^W_{\lambda_{W+}\lambda_{W-}}\right|^2 < \frac{3\left(3-6\sin^2\theta_W+8\sin^4\theta_W\right)}{5\alpha^2(\hat{s})\left(1-\frac{4M_W^2}{\hat{s}}\right)^{\frac{3}{2}}} \tag{7.11}$$

where λ_{W+}, λ_{W-} are the final-state W^+, W^- boson helicities, respectively. For the assumed form factor, unitarity is violated in the W^+W^- process if

$$\frac{(1-\frac{4M_W^2}{\hat{s}})^{\frac{3}{2}}}{(1+\frac{\hat{s}}{\Lambda_W^2})^4}\left[\left(\frac{\hat{s}}{M_W^2}\right)(\Delta\kappa+\lambda)^2+\frac{1}{2}\left(\frac{\hat{s}}{M_W^2}\right)^2\lambda^2 + \frac{1}{4}\left(\frac{\hat{s}}{M_W^2}\right)^2\Delta\kappa^2\right] \geq \frac{3\left(3-6\sin^2\theta_W+8\sin^4\theta_W\right)}{5\alpha^2(\hat{s})} \tag{7.12}$$

over the $\sqrt{\hat{s}}$ range $2M_W < \sqrt{\hat{s}} < 1.8$ TeV.

If only one anomalous coupling is assumed to be non-zero at a time, then for $\Lambda_W >> M_W$ and the assumed dipole form factor and form factor power, the unitarity limits are:

$$W\gamma: \quad |\Delta\kappa| < \frac{37.1 \text{ TeV}}{\Lambda_W} \quad (\lambda = 0)$$

$$|\lambda| < \frac{3.9 \text{ TeV}^2}{\Lambda_W^2} \quad (\Delta\kappa = 0)$$

$$W^+W^-: \quad |\Delta\kappa| < \frac{7.3 \text{ TeV}^2}{\Lambda_W^2} \quad (\lambda = 0)$$

$$|\lambda| < \frac{5.3 \text{ TeV}^2}{\Lambda_W^2} \quad (\Delta\kappa = 0)$$

In Figure 7.6, the two-dimensional $W + \gamma$ unitarity limits in the $\Delta\kappa - \lambda$ plane are indicated by dotted curves. The two-dimensional W^+W^- unitarity limits in the $\Delta\kappa - \lambda$ plane are indicated by the dashed ellipse. The $W\gamma$ and W^+W^- unitarity limits for $\Delta\kappa$ and λ as a function of Λ_W are shown in Figures 7.7 and 7.8, respectively. Superimposed on these plots are the 68%, 90% and 95% CL limits on $\Delta\kappa$ and λ, shown as dot-dashed, dashed and solid curve, respectively. The intersection of the unitarity limit curves and the experimental 95% CL limits on $\Delta\kappa$ and λ correspond to a compositeness scale sensitivity for the saturation of the unitarity bound of $\Lambda_W \geq 1.0$ TeV. Above this value of Λ_W, the experimental limits on $\Delta\kappa$ and λ are weaker than the unitarity limits, as shown in figures 7.7 and 7.8. This value of Λ_W corresponds to a distance scale sensitivity to possible internal structure of the W boson of

$$L_W = \frac{\hbar c}{\Lambda_W} \leq 2.0 \times 10^{-4} \text{ fm} = 0.08 \, \lambda\!\!\!^{-}_W \tag{7.13}$$

where $\lambda\!\!\!^{-}_W = \hbar c / M_W c^2$ is the reduced Compton wavelength of the W boson.

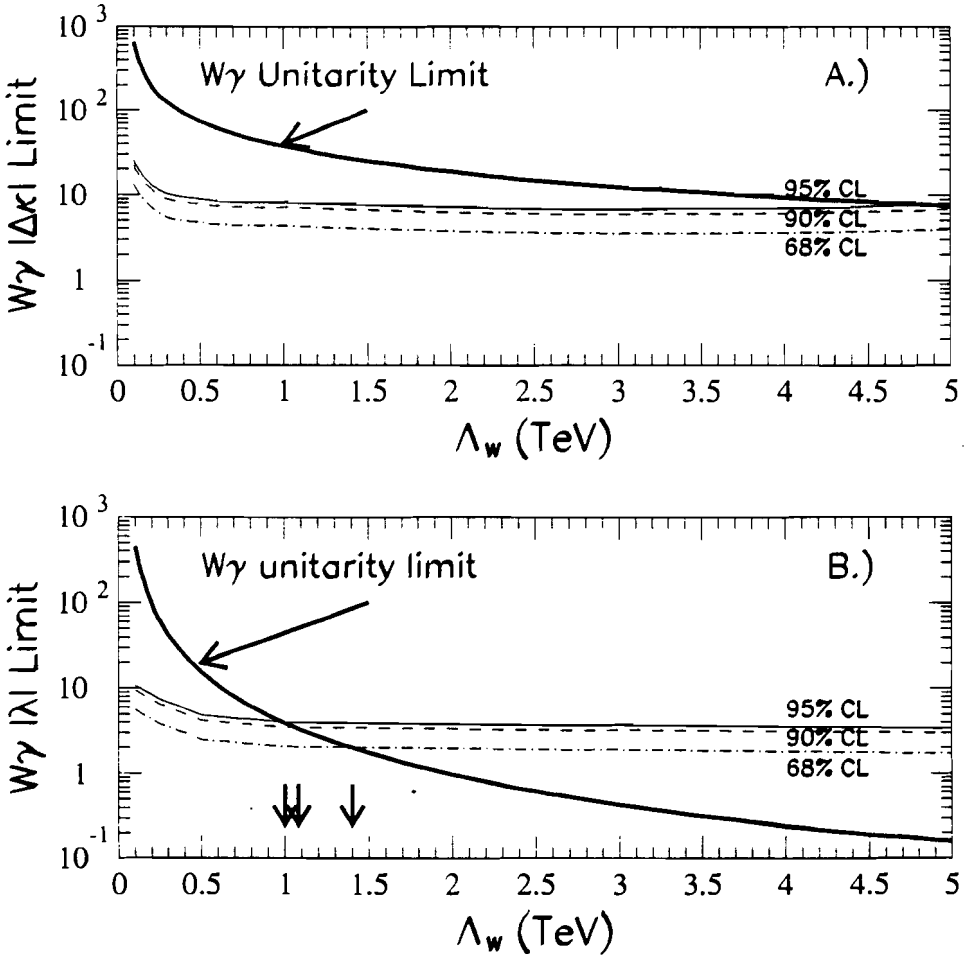

Figure 7.7: Unitarity limits as a function of Λ_W for anomalous $WW\gamma$ couplings, for a generalized dipole form factor pawer $n = 2$. (A) $|\Delta\kappa|$ unitarity limit ($\lambda = 0$) as a function of compositeness scale Λ_W for anomalous $W\gamma$ couplings. (B) $|\lambda|$ unitarity limit ($\Delta\kappa = 0$) as a function of compositeness scale Λ_W for anomalous $W\gamma$ couplings.

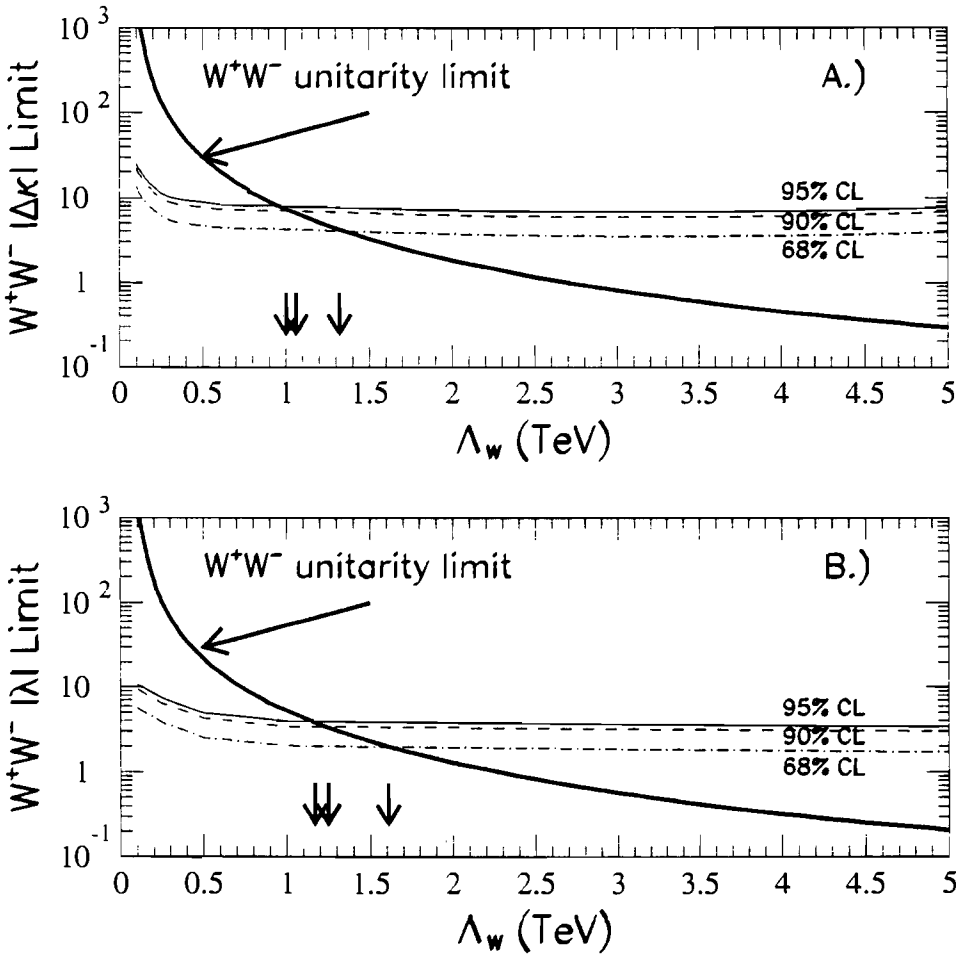

Figure 7.8: Unitarity limits as a function of Λ_W for anomalous $WW\gamma$ couplings, for a generalized dipole form factor pawer $n = 2$. (A) $|\Delta\kappa|$ unitarity limit ($\lambda = 0$) as a function of compositeness scale Λ_W for anomalous W^+W^- couplings. (B) $|\lambda|$ unitarity limit ($\Delta\kappa = 0$) as a function of compositeness scale Λ_W for anomalous W^+W^- couplings.

Note that the unitarity bounds and the Λ_W scale sensitivity have some model-dependence associated with the choice of the form factor power n used in the generalized form factor. For example, we have chosen $n = 2$ for the form factor power in this analysis, motivated by the well-known behavior of the nucleon form factors. If instead, a value of $n = 1$ is chosen for the form factor power, the unitarity bounds on $\Delta\kappa$ and λ are made more strict by a factor of ~ 4, and the corresponding Λ_W-scale sensitivity is reduced by a factor of ~ 2 [15]. The experimental limits on $\Delta\kappa$ and λ are not significantly changed for $n = 1$.

7.4 Limits on W Boson Magnetic Dipole and Electric Quadrupole Moments

Experimental limits on the $\Delta\kappa$ and λ parameters associated with possible anomalous $WW\gamma$ couplings also place bounds on the higher-order electromagnetic moments of the W boson – the magnetic dipole moment, μ_W, its electric quadrupole moment Q_W and also the W boson mean-squared charge radius, $< R_W^2 >$. In the static limit these quantities are related to the $\Delta\kappa$ and λ parameters by:

$$\mu_W = \frac{e}{2M_W}(2 + \Delta\kappa + \lambda) \quad \text{Magnetic Dipole Moment} \tag{7.14}$$

$$Q_W = -\frac{e}{M_W^2}(1 + \Delta\kappa - \lambda) \quad \text{Electric Quadrupole Moment} \tag{7.15}$$

$$< R_W^2 > = \frac{1}{M_W^2}(1 + \Delta\kappa + \lambda) \quad \text{Mean} - \text{Squared Charge Radius} \tag{7.16}$$

Recall that in the SM (at the tree level): $\Delta\kappa = 1 - \kappa = 0$, $\lambda = 0$. The

numerical values expected for these Standard Model parameters are:

$$\mu_W^\circ = \frac{e\hbar c}{2M_W c^2} = 3.691 \pm 0.012 \times 10^{-16} \text{ MeV/T}$$

$$(\mu_e^\circ = \frac{e\hbar c}{2M_e c^2} = 5.788 \pm 0.000 \times 10^{-11} \text{ MeV/T})$$

$$Q_W^\circ = -e\left(\frac{\hbar c}{M_W c^2}\right)^2 = -e\,\lambda\!\!\!^{-2}_W = 6.063 \pm 0.041 \times 10^{-6} \text{ efm}^2$$

$$\lambda\!\!\!^{-}_W = \frac{\hbar c}{M_W c^2} = 2.462 \pm 0.008 \times 10^{-3} \text{ fm}$$

where $\lambda\!\!\!^{-}_W$ is the (reduced) Compton wavelength of the W boson and μ_W° is the Bohr magneton of the W boson. Note that the uncertainties on these quantities are due primarily to the uncertainty on the W boson mass, $M_W = 80.14 \pm 0.27$ GeV/c^2 (the combined CDF+UA2 result) [27, 28]. The W boson electromagnetic moments, μ_W and Q_W and the mean-squared charge radius, $< R_W^2 >$ are summarized in table 7.7.

Figure 7.9 shows the 68.3%, 90.0% and 95.0% single-sided CL contours in the $Q_W/Q_W^\circ - \mu_W/\mu_W^\circ$ plane for cross section results.

Table 7.7: $W\gamma$ EM Moments Limits

Parameter	CL Range	Limits
μ_W/μ_W°	68.3% DS CL	$2.0\ ^{+3.4}_{-3.4}\ (stat)\ \pm\ 0.5\ (syst)$
		$=\ 2.0\ ^{+3.9}_{-3.9}\ (stat+syst)$
	68.3% SS CL	$-2.6\ <\ \mu_W/\mu_W^\circ - 2\ \equiv\ g_W - 2\ <\ +2.7$
$(Q_W/Q_W^\circ = 1)$	90.0% SS CL	$-4.6\ <\ \mu_W/\mu_W^\circ - 2\ \equiv\ g_W - 2\ <\ +4.7$
	95.0% SS CL	$-5.3\ <\ \mu_W/\mu_W^\circ - 2\ \equiv\ g_W - 2\ <\ +5.4$
Q_W/Q_W°	68.3% DS CL	$1.0\ ^{+5.3}_{-4.9}\ (stat)\ \pm\ 0.7\ (syst)$
		$=\ 1.0\ ^{+5.9}_{-5.6}\ (stat+syst)$
	68.3% SS CL	$-3.8\ <\ Q_W/Q_W^\circ - 1\ \equiv\ q_W - 1\ <\ +4.1$
$(\mu_W/\mu_W^\circ = 2)$	90.0% SS CL	$-6.8\ <\ Q_W/Q_W^\circ - 1\ \equiv\ q_W - 1\ <\ +7.1$
	95.0% SS CL	$-7.8\ <\ Q_W/Q_W^\circ - 1\ \equiv\ q_W - 1\ <\ +8.1$
$< R_W^2 > / \lambda_W^2$	68.3% DS CL	$1.0\ ^{+3.4}_{-3.4}\ (stat)\ \pm\ 0.5\ (syst)$
		$=\ 1.0\ ^{+3.9}_{-3.9}\ (stat+syst)$
	68.3% SS CL	$-2.6\ <\ < R_W^2 > / \lambda_W^2 - 1\ \equiv\ r_W^2 - 1\ <\ +2.7$
$(Q_W/Q_W^\circ = 1)$	90.0% SS CL	$-4.6\ <\ < R_W^2 > / \lambda_W^2 - 1\ \equiv\ r_W^2 - 1\ <\ +4.7$
	95.0% SS CL	$-5.3\ <\ < R_W^2 > / \lambda_W^2 - 1\ \equiv\ r_W^2 - 1\ <\ +5.4$

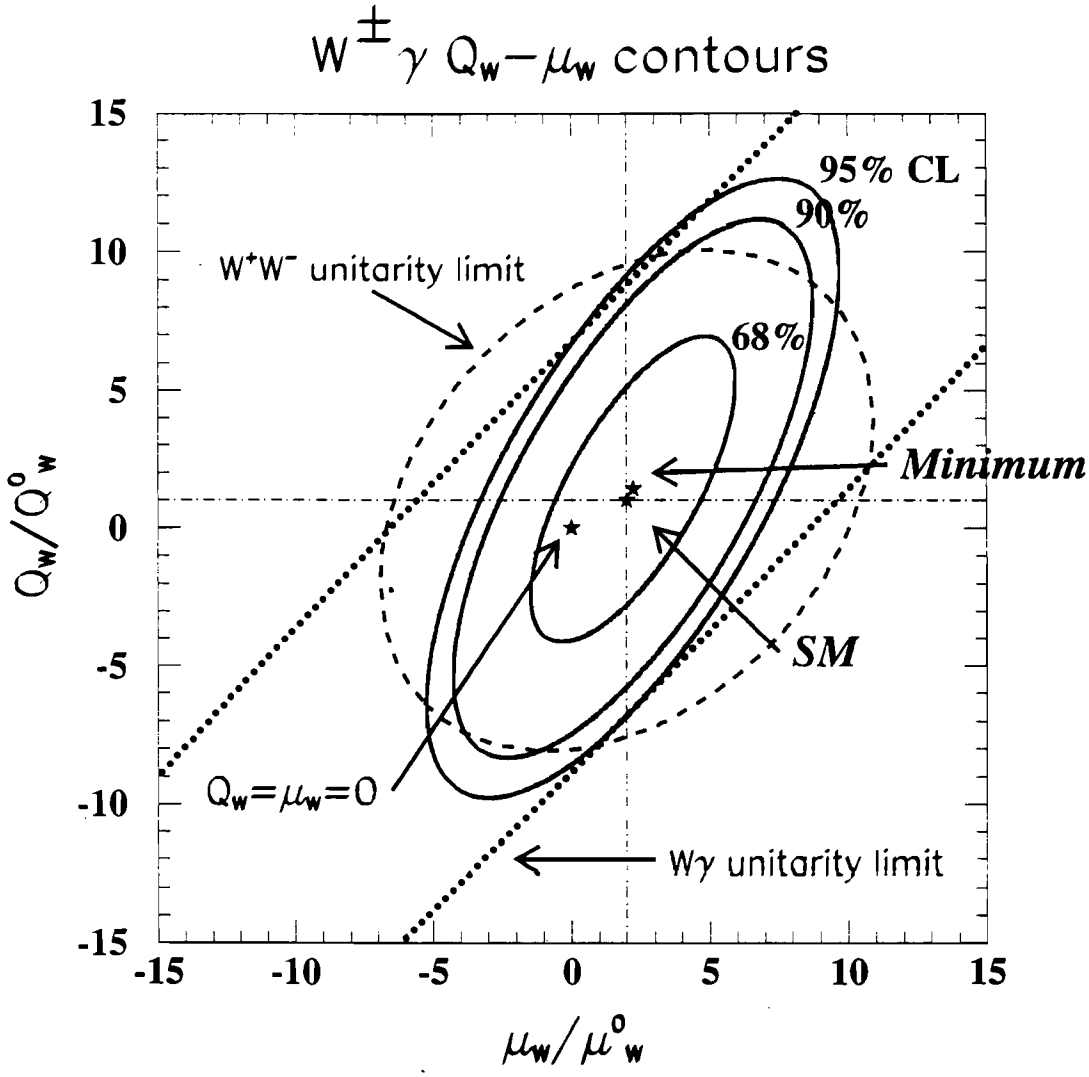

Figure 7.9: $W\gamma$ Cross Section Contours in $Q_W/Q_W^\circ - \mu_W/\mu_W^\circ$ plane

Chapter 8

Conclusions

In this chapter the experimental results for the cross section $\times$ branching ratio, limits on $\Delta\kappa\,(=\,\kappa\,-\,1)$ and λ, the anomalous $WW\gamma$ couplings, are summarized. Future prospects for the study of the $W\gamma$ process will be discussed.

The cross section $\times$ branching ratio for $W(\rightarrow e\nu) + \gamma$ in the inclusive electron W data from the CDF 1988-1989 Tevatron collider run was measured. There were eight $W\gamma$ candidate events in 4.05 pb^{-1} of data. The photons in those events were required to have transverse energy greater than 5 GeV and $\Delta R_{e\gamma} > 0.7$. From these events the experimental cross section times decay branching ratio, $\sigma \cdot B(W\gamma)_{exp}$, was measured to be:

$$\sigma \cdot B(W\gamma)_{exp} = 17.0^{+13.7}_{-13.4}\ (stat + syst)\ \text{pb}$$

Which is in good agreement with the Standard Model prediction of:

$$\sigma \cdot B(W\gamma)_{SM} = 19.0^{+3.3}_{-0.9}\ (stat + syst)\ \text{pb}$$

Using the $W\gamma$ cross section measurement, direct limits on the $WW\gamma$ anomalous coupling parameters, $\Delta\kappa$ and λ are :

$$\Delta\kappa = 0.0^{+5.7}_{-5.2}\ (stat + syst)\quad (\lambda = 0) \qquad \lambda = 0.0^{+2.5}_{-2.5}\ (stat + syst)\quad (\Delta\kappa = 0)$$

$$-7.2 < \Delta\kappa < +7.7 \quad (\lambda = 0,\ 95.0\%\ CL)$$

$$-3.5 < \lambda < +3.4 \quad (\Delta\kappa = 0,\ 95.0\%\ CL)$$

Because the anomalous $WW\gamma$ parameters, $\Delta\kappa$ and λ, are correlated, the $W\gamma$ cross section contour in the $\Delta\kappa$ - λ plane provides a better description of the $WW\gamma$ couplings than the $W\gamma$ cross section projected on the $\Delta\kappa$ and λ axes (see figures 7.4,7.5 and 7.6). These cross section confidence level contours form ellipses in the $\Delta\kappa$ - λ plane. The direct experimental limits on $\Delta\tilde{\kappa}$ and $\tilde{\lambda}$ are within 10|; % of the direct limits on $\Delta\kappa$ and λ.

The UA2 Collaboration has recently published direct limits on $\Delta\kappa$, λ and the $\Delta\kappa - \lambda$ contour (ellipse) from an analysis of $13\,\mathrm{pb}^{-1}$ of $p\bar{p} \rightarrow e^{\pm}\nu\gamma$ data [58]. The $\Delta\kappa$ and λ limits from both the UA2 and this analysis are comparable with each other. The correlation between $\Delta\kappa$ and λ is much stronger for $\sqrt{s} = 630\,\mathrm{GeV}$ than at the Tevatron ($\sqrt{s} = 1800\,\mathrm{GeV}$). As a consequence of the interference effects between these parameters, the axes of the ellipses formed by the UA2 68.3% CL and 95% CL limit contours in the $\Delta\kappa - \lambda$ plane (see figure 5 in reference [58]) are rotated more significantly with respect to the $\Delta\kappa$ and λ axes than the axes of the ellipses formed by the cross section limits presented in this thesis (see figure 7.6 in chapter 7).

In the static limit the $\Delta\kappa$ and λ parameters are related to the W boson magnetic dipole and electric quadrupole moments, and mean-squared charge radius by:

$$\mu_W = \mu_W^{\circ}(2 + \Delta\kappa + \lambda)$$

$$Q_W = Q_W^{\circ}(1 + \Delta\kappa - \lambda)$$

$$< R_W^2 > = \lambda\!\!\!^{-2}_W(1 + \Delta\kappa + \lambda),$$

where $\lambda\!\!\!^{-}_W = (\hbar c)/M_W c^2$ is the (reduced) Compton wavelength of the W boson. $\mu_W^{\circ} = e\hbar/2M_W c$ and $Q_W^{\circ} = -e\,\lambda\!\!\!^{-2}_W$ are the Standard Model values of the W boson Bohr magneton and electric quadrupole moment, respectively. The limits on these

higher-order electromagnetic moments of the W boson were measured to be:

$$\mu_W/\mu_W^\circ \equiv g_W = 2.0^{+3.9}_{-3.9}\,(stat+syst) \quad (Q_W/Q_W^\circ = 1)$$

$$Q_W/Q_W^\circ \equiv q_W = 1.0^{+5.9}_{-5.6}\,(stat+syst) \quad (\mu_W/\mu_W^\circ = 2)$$

$$< R_W^2 > / \lambda\!\!\!^{-2}_W \equiv r_W^2 = 1.0^{+3.9}_{-3.9}\,(stat+syst) \quad (Q_W/Q_W^\circ = 1)$$

$$-5.3 < \mu_W/\mu_W^\circ - 2 \equiv g_W - 2 < +5.4 \quad (Q_W/Q_W^\circ = 1,\ 95.0\%\ CL)$$

$$-7.8 < Q_W/Q_W^\circ - 1 \equiv q_W - 1 < +8.1 \quad (\mu_W/\mu_W^\circ = 2,\ 95.0\%\ CL)$$

$$-5.3 < < R_W^2 > / \lambda\!\!\!^{-2}_W - 1 \equiv r_W^2 - 1 < +5.4 \quad (Q_W/Q_W^\circ = 1,\ 95.0\%\ CL)$$

For saturation of unitarity these results are sensitive to a compositeness scale of $\Lambda_W \geq 1.0\,\text{TeV}$. The limits of the $WW\gamma$ anomalous couplings, $\Delta\kappa$ and λ, probe the possible internal (composite) structure of the W boson at a distance scale of the order $L_W \leq 2.0 \times 10^{-4}\,\text{fm} = 0.08\,\lambda\!\!\!^{-}_W$ at 95.0% CL.

Future

The overall uncertainty in the measurement of $\sigma \cdot B(W\gamma)_{exp}$ in the inclusive electron W data sample is

$$\frac{\delta\sigma \cdot B(W\gamma)}{\sigma \cdot B(W\gamma)} \sim 80\%.$$

The overall uncertainty in the measurement of $\sigma \cdot B(W\gamma)_{exp}$ can be decreased by using the $W\gamma$ events from both the inclusive electron W data sample (this analysis) ($\int \mathcal{L}\,dt = 4.05\,\text{pb}^{-1}$) and the inclusive muon W data sample ($\int \mathcal{L}\,dt = 3.54\,\text{pb}^{-1}$). By using the combined $e + \mu$ inclusive W data samples, the overall uncertainty in the cross section $\times$ branching ratio is

$$\frac{\delta\sigma \cdot B(W\gamma)}{\sigma \cdot B(W\gamma)} \sim 60\%.$$

Table 8.1: The overall uncertainty in $\sigma \cdot B(W\gamma)$ for increasing integrated luminosity

	electron data	Combined $e + \mu$ Results			
	88-89 run	88-89 run	Run Ia	Run Ia+Ib	Run III
$\int \mathcal{L} \cdot dt\,(\mathrm{pb})$	4	4	20	100	1000
$\delta\sigma \cdot B(W\gamma)/\sigma \cdot B(W\gamma)$	$\sim$ 80%	$\sim$ 60%	$\sim$ 22%	$\sim$ 10%	$\sim$ 3%

During the past year the Tevatron ran and the CDF Collaboration collected 21 pb^{-1} of data. Using this data with the same photon cuts as the analysis presented in this thesis the uncertainty in the cross section $\times$ branching ratio would be expected to be reduced to:

$$\frac{\delta\sigma \cdot B(W\gamma)}{\sigma \cdot B(W\gamma)} \sim 22\%.$$

The uncertainty in the cross section $\times$ branching ratio for integrated luminosities of 100 pb^{-1} and 1000 pb^{-1} are summarized in table 8.1.

Improvements in limits on anomalous couplings obey **fourth-root** scaling law; specifically, non Standard Model $\sigma \cdot B(W\gamma)$ depends quadratically on the anomalous couplings α_{anom} [17]:

$$\sigma(\alpha_{anom}) \sim \sigma_{SM} + \alpha^2_{anom} \cdot \sigma_{\alpha_{anom}}$$

Table 8.1 summarizes the overall uncertainty in $\sigma \cdot B(W\gamma)$ for increasing integrated luminosity. Table 8.2 shows how the limits on the anomalous $WW\gamma$ parameters, $\Delta\kappa$ and λ, and subsequently the magnetic dipole and electric quadrupole moments of the W boson are reduced with increasing luminosity.

With increased statistics it is possible to use **differential** distributions to make better comparisons with the Standard Model predictions for $W\gamma$. The possible distributions one could use might include: the photon transverse energy spectrum, (E_T^γ); the angular separation between the lepton from the decay of the W boson and the photon,$\Delta R_{l\gamma}$ and pseudo-rapidity difference between the decay lepton and

Table 8.2: The limits on $\Delta\kappa$ and λ for increasing integrated luminosity

	electron data	Combined $e+\mu$ Results			
	88-89	88-89	Run Ia	Run Ia+Ib	Run III
$\int \mathcal{L} \cdot dt\,(\mathrm{pb})$	4	4	20	100	1000
$\Delta\kappa$ 95 % CL Limits	7.7	7.0	4.6	**3.3**	1.8
λ 95 % CL Limits	3.5	3.1	2.1	1.5	0.8
(μ_W/μ_W°) 95 % CL Limits	5.4	4.9	3.3	2.2	1.2
(Q_W/Q_W°) 95 % CL Limits	8.1	7.4	4.9	3.3	1.9

the photon, $(\Delta\eta_{\gamma-\ell})$. By understanding these distributions for the $W\gamma$ signal and the background to $W\gamma$, it is possible to use more advanced statistical methods such as maximum likelihood or multi-variant analyses to set **considerably** better limits than by simple scaling due to increase integrated luminosity.

Appendix A

Individual Acceptances for $W\gamma$

Table A.1: Individual Acceptances of W boson

$A_{M_W^T}$	$97.9 \pm 0.1\%$
$A_{E_T}^W$	$64.2 \pm 0.02\%$
A_{fid}^W	$45.4 \pm 0.04\%$
$A_{\not\!\!E_T}^{\mathcal{D}}$	$93.5 \pm 0.04\%$
A_W	$27.6 \pm 0.06\%$

Table A.2: Individual Acceptancès of photon

f^γ	$48.2 \pm 0.3\%$
$A_{E_T^\gamma}^\gamma$	1.00
A_{fid}^γ	$77.9 \pm 0.2\%$
$A_{\Delta R_{e\gamma}}^\gamma$	1.00
A^γ	$77.9 \pm 0.2\%$

Appendix B

Individual Efficiencies for $W\gamma$

Table B.1: Individual Electron Efficiencies for the $W\gamma$ Data Sample

ϵ_{zvx}	$95.4 \pm 0.1\%$	$\lvert Z_{vtx}\rvert < 60$ *cm*
ϵ_{iso}	$96.0 \pm 1.0\%$	Isolation $I < 0.1$ Cut
$\epsilon_{(Had/EM)_T}$	$99.0 \pm 1.0\%$	Had/EM Cut
$\epsilon_{\chi^2_{strip}}$	$97.0 \pm 1.0\%$	$\chi^2_{strip} < 15$ Cut
ϵ_{Lshr}	$97.0 \pm 1.0\%$	$L_{shr} < 0.2$ Cut
$\epsilon_{(E/P)_T}$	$93.0 \pm 1.0\%$	E/P < 1.5 Cut
ϵ_{trk}	$100.0^{+0.0}_{-0.1}\%$	CTC Track Reconstruction
$\epsilon_{\Delta z}$	$98.0 \pm 1.0\%$	$\Delta z < 3.0$ *cm* Matching Cut
$\epsilon_{\Delta x}$	$97.0 \pm 1.0\%$	$\Delta x < 1.5$ *cm* Matching Cut
ϵ^e_{L1}	$99.3 \pm 0.3\%$	Level-1 Central Electron Trigger
ϵ^e_{L2}	$98.0 \pm 0.4\%$	Level-2 Central Electron Trigger
ϵ^e_{L3}	$100.0^{+0.0}_{-0.1}\%$	Level-3 Central Electron Trigger

Table B.2: CEM Photon Efficiency Determination

Data Sample	ϵ^{γ}_{ET4}	$\epsilon^{\gamma}_{ET4} \cdot \epsilon^{\gamma}_{\Sigma PT4}$	$\epsilon^{\gamma}_{ET4} \cdot \epsilon^{\gamma}_{\Sigma PT4} \cdot \epsilon^{\gamma}_{N3D}$
W Random Cones	$95.5 \pm 0.5\%$	$93.4 \pm 0.6\%$	$89.2 \pm 0.7\%$
QFL $W\gamma$ MC	$98.9 \pm 0.6\%$	$96.4 \pm 1.0\%$	$90.2 \pm 1.5\%$
MinBias Random Cones	$98.6 \pm 0.2\%$	$97.7 \pm 0.2\%$	$92.8 \pm 0.2\%$
QCDa Random Cones	$99.1 \pm 0.1\%$	$97.6 \pm 0.1\%$	$92.7 \pm 0.2\%$
QCDb Random Cones	$92.7 \pm 0.2\%$	$89.3 \pm 0.3\%$	$84.2 \pm 0.3\%$

Table B.3: CEM Photon Efficiency Determination (continued)

Data Sample	$\epsilon^{\gamma}_{Had/EM}$	ϵ^{γ}_{Lshr}	$\epsilon^{\gamma}_{\chi^2_{stp}+\chi^2_{\psi ir}}$	$\epsilon^{\gamma}_{no\ 2^{nd}\ CES}$
5 GeV e TB	$98.9 \pm 0.2\%$	$99.9 \pm 0.1\%$	$97.3 \pm 0.3\%$	$98.0 \pm 0.1\%$
10 GeV e TB	$99.6 \pm 0.1\%$	$98.8 \pm 0.4\%$	$96.2 \pm 0.4\%$	$97.9 \pm 0.1\%$
18 GeV e TB	$99.1 \pm 0.9\%$	$100.0^{+0.0}_{-1.7}\%$	$98.2 \pm 1.8\%$	$98.2 \pm 1.6\%$
30 GeV e TB	$98.9 \pm 0.9\%$	$100.0^{+0.0}_{-1.1}\%$	$99.2 \pm 0.7\%$	$98.2 \pm 1.0\%$
50 GeV e TB	$98.0 \pm 0.3\%$	$99.9 \pm 0.1\%$	$99.2 \pm 0.2\%$	$97.9 \pm 0.2\%$
QFL $W\gamma$ MC	$99.3 \pm 0.6\%$	$99.7 \pm 0.3\%$	$98.4 \pm 0.5\%$	$94.6 \pm 1.2\%$
QFL γ MC $5 - 15$ GeV	$99.7 \pm 0.1\%$	$99.8 \pm 0.1\%$	$97.4 \pm 0.3\%$	$96.8 \pm 0.3\%$
QFL e MC $5 - 15$ GeV	$99.9 \pm 0.1\%$	$99.9 \pm 0.1\%$	$97.9 \pm 0.2\%$	$95.8 \pm 0.3\%$

Table B.4: Overall CEM Photon Efficiency Determination

ϵ^{γ}_{ET4}	$95.7 \pm 0.3 \pm 0.5\%$	Calorimeter Isolation
$\epsilon^{\gamma}_{\Sigma PT4}$	$97.4 \pm 0.4 \pm 0.8\%$	Tracking Isolation
ϵ^{γ}_{N3D}	$95.3 \pm 0.5 \pm 0.7\%$	No track @ EM Cluster
$\epsilon^{\gamma}_{Had/EM}$	$99.2 \pm 0.1 \pm 0.8\%$	Had/EM Cut
ϵ^{γ}_{Lshr}	$99.9 \pm 0.1 \pm 0.3\%$	Lateral Shower Cut
$\epsilon^{\gamma}_{\chi^2_{stp}+\chi^2_{wir}}$	$98.4 \pm 0.1 \pm 0.9\%$	CES strip/wire χ^2 Cut
$\epsilon^{\gamma}_{no\ 2^{nd}\ CES}$	$97.9 \pm 0.7 \pm 1.0\%$	No 2^{nd} CES Clusters
$\mathcal{P}^{\gamma}_{conv}$	$96.5 \pm 0.2 \pm 1.0\%$	Photon Survival
$\mathcal{S}^{cem}_{e\to\gamma}$	$100.3 \pm 0.6 \pm 1.0\%$	e *vs.* γ Shower Development
ϵ^{γ}_{cem}	$82.0 \pm 1.2 \pm 2.4\%$	Overall Photon Efficiency

Appendix C

CDF Jet Clustering Algorithm

The CDF Jet clustering algorithm differs from the electron clustering algorithm used in the definition of electrons and photons because of the intrinsic size of QCD jets. The CDF jet clustering algorithm uses a cone of fixed radius to define a jet. This energy clustering algorithm was designed to measure the total energy of the initial parton by summing the energy of all the individual particles that came from the fragmentation of that parton. [59] Studies have shown that the fixed cone algorithm produces better jet separation in $\eta - \phi$ space than other jet clustering algorithms. [60] The jet clustering algorithm begins by recording all towers (seeds) with $E_T > 0.2\,\mathrm{GeV}$. A cone of radius $\Delta R = 0.7$ is drawn around the seed tower and all towers whose centroids are inside the cone are added to the cluster. The center of the cluster is calculated using the E_T centroid of each tower in the cluster. A new cone is drawn around the cluster centroid and towers are added or removed from the cluster depending on their centroids. The process of recomputing the cluster centroid by adding or deleting towers from the cluster list continues until the list of towers in the cluster remains stable. [61] Care is taken to handle possible overlapping jets and other pathological topologies that could lead to a non-convergence of the algorithm. The choice of a cone size of $\Delta R = 0.7$ was based on the distribution of energy flow with respect to the jet axis in events dominated by two jets. Most of the energy was contained in a cone of $\Delta R = 0.7$. The merging probability of the CDF jet clustering algorithm for two jets of $\Delta R = 0.85$ is $\sim 25\%$. [61] It was determined through various Monte Carlo and detector simulation studies [59] that the jet clustering algorithm could find jets with an uncorrected $E_T \geq 5$ GeV.

References

[1] Review of Particle Properties, Phys. Rev. D **45**, II.3 (1992).

[2] S.L. Glashow, Nucl. Phys. **22**, 579 (1961); S. Weinberg, Phys. Rev. Lett. **19**, 1264 (1967); A. Salam, in *Elementary Particle Theory: Relativistic Groups and Analyticity (Nobel Symposium No. 8)*, edited by N. Svartholm (Almqvist and Wiksell, Sweden, 1968), p. 367; see also S.L. Glashow, J. Illiopoulous and L. Maiani, Phys. Rev. **D2**, 1285 (1970).

[3] S. Weinberg, Phys. Rev. Lett. **19**, 1264 (1967).

[4] F.J. Hasert it et. al., Phys. Lett. **46B**, 138 (1973).

[5] UA-1 Collaboration, Phys. Lett. **122B**, 103 (1983); UA-2 Collaboration, Phys. Lett. **122B**, 476 (1983).

[6] UA-1 Collaboration, Phys. Lett. **126B**, 398 (1983).

[7] C. Sutton, *The Particle Connection* (Simon and Schuster, New York, 1984), p. 115.

[8] F. Abe *et al.*, Phys. Rev. D **44**, 29 (1991); Review of Particle Properties, Phys. Rev. D **45**, II.1 (1992).

[9] R.W. Robinett, Phys. Rev. D **28**, 1185 (1983); G.N. Valenzuela and J. Smith, Phys. Rev. D **31**, 2787 (1985); J. Cortes, K. Hagiwara and F. Herzog, Nucl. Phys. B **278**, 26 (1986).

[10] F. Abe *et al.*, Phys. Rev. Lett. **70**, 4042 (1993).

[11] F.M. Renard, Nucl. Phys. B **196**, 93 (1982); R. Barbieri, H. Harari and M. Leurer, Phys. Lett. B **141**, 455 (1985); J.P. Eboli, A.V. Olinto, Phys. Rev. D **38**, 3461 (1988).

[12] F. Abe *et al.*, Phys. Rev. Lett. **64**, 152 (1990); F. Abe *et al.*, Phys. Rev. Lett. **69**, 28 (1992); F. Abe *et al.*, Phys. Rev. Lett. **68**, 3398 (1992); A. Roodman, Ph.D. thesis, University of Chicago (1991).

[13] F. Abe *et al.*, Phys. Rev. Lett. **62**, 1005 (1989); F. Abe *et al.*, Phys. Rev. D **44**, 29 (1991); P. Derwent, Ph.D. thesis, University of Chicago (1990);

[14] Review of Particle Properties, Phys. Rev. D **45**, V.2, V.3 (1992).

[15] U. Baur and D. Zeppenfeld, Nucl. Phys. B **308**, 127 (1988).

[16] J.M. Cornwall, D.N. Levin, and G. Tiktopoulos, Phys. Rev. Lett. **30**, 1268 (1973); J.M. Cornwall, D.N. Levin, and G. Tiktopoulos, Phys. Rev. D **10**, 1145 (1974); C.H. Llewellyn Smith, Phys. Lett. **46B**, 233 (1973); S.D. Joglekar, Ann. of Phys. **83**, 427 (1974).

[17] U. Baur and E.L. Berger, Phys. Rev. D **41**, 1476 (1990).

[18] U. Baur and D. Zeppenfeld, Phys. Lett. B **201**, 383 (1988).

[19] K. Hagiwara *et al.*, Nucl. Phys. B **282**, 253 (1987).

[20] Review of Particle Properties, Phys. Rev. D **45**, VIII.8, (1992).

[21] K.O. Mikaelian, Phys. Rev. D **17**, 750 (1978); K.O. Mikaelian, M.A. Samuel and D. Sahdev, Phys. Rev. Lett. **43**, 746 (1979); R.W. Brown, K.O. Mikaelian and D. Sahdev, Phys. Rev. D **20**, 1164 (1979); T.R. Grose and K.O. Mikaelian, Phys. Rev. D **23**, 123 (1981); C.J. Goebel, F. Halzen and J.P. Leveille, Phys. Rev. D **23**, 2682 (1981); S.J. Brodsky and R.W. Brown, Phys. Rev. Lett. **49**, 966 (1982); M.A. Samuel, Phys. Rev. D **27**, 2724 (1983); R.W. Brown, K.L. Kowalski and S.J. Brodsky, Phys. Rev. D **28**, 624 (1983); R.W. Brown and K.L. Kowalski, Phys. Rev. D **29**, 2100 (1984); J. Cortés, K. Hagiwara and F. Herzog, Nucl. Phys. B **278**, 26 (1986).

[22] J. Smith, D. Thomas and W.L. van Neerven, Z. Phys. C **44**, 267 (1989); S. Mendoza, J. Smith and W.L. van Neerven, Phys. Rev. D **47**, 3913 (1993); J. Ohnemus, Phys. Rev. D **47**, 940 (1993) and U. Baur, T. Han and J. Ohnemus, to appear in Phys. Rev. D, and FSU-HEP-930519 preprint (May, 1993).

[23] U. Baur, S. Errede and G. Landsberg, to be published in *the Proceedings of the Workshop on Physics at Current Accelerators and the Supercollider*, edited by J. Hewitt, A. White and D. Zeppenfeld (Argonne, June 2-5, 1993) and FSU-HEP-930727 preprint (July, 1993).

[24] F. Boudjema, K. Hagiwara, C. Hamazaoui and K. Numata, Phys. Rev. D **43**, 2223 (1991); W.J. Marciano and A. Queijeiro, Phys. Rev. D **33**, 3449 (1986).

[25] T.D. Lee and C.N. Yang, Phys. Rev. **128**, 885 (1962); L.D. Landau and E.M. Lifshitz, *Quantum Mechanics* (Addison-Wesley Publishing Co, Inc., Reading, MA, 1965), p. 262; H. Aronson, Phys. Rev. **186**, 1434 (1969); K.J. Kim and Y.-S. Tsai, Phys. Rev. D **7**, 3710 (1973).

[26] D.R. Yennie, M.M. Lévy and D.G. Ravenhall, Rev. Mod. Phys. **29**, 144 (1957); L. Durand III, P.C. DeCelles and R.B. Marr, Phys. Rev. **126**, 1882 (1962).

[27] F. Abe *et al.*, Phys. Rev. D **43**, 2070 (1991); F. Abe *et al.*, Phys. Rev. Lett. **65**, 2243 (1990); W. Trischuk, Ph.D. thesis, Harvard University (1990); P. Schlabach, Ph.D. thesis, University of Illinois at Urbana-Champaign (1990).

[28] J. Alitti *et al.*, Phys. Lett. B **241**, 150 (1990).

[29] D. H. Perkins, *Introduction to High Energy Physics* (Addison-Wesley Publishing Co, Inc., Reading, MA, 1987), *pp.* 139-141.

[30] K. Symon, *Mechanics* (Addison-Wesley Publishing Co, Inc., Reading, MA, 1971) *pp.* 144-147; R. Fernow, *Introduction to Experimental Particle Physics* (Cambridge University Press, New York, 1986), *pp.* 234-236.

[31] F. Bedeschi *et al.*, Nucl. Instr. Methods A **238**, 50 (1988).

[32] G.W. Foster *et al.*, Nucl. Instr. Methods A **269**, 93 (1988).

[33] K. Yasuoka *et al.*, Nucl. Instrum. Methods A **267**, 315 (1988).

[34] L. Balka *et al.*, Nucl. Instrum. Methods A **267**, 272 (1988).

[35] ISAJET Monte Carlo version 6.24,F.E. Paige and S.D. Protopopescu, BNL Technical Report No. 38034, 1986 (unpublished).

[36] QFL Monte Carlo version x.x,

[37] VEGAS, G. Peter Lepage, J. Comp. Phys. **27**, 192-202, Academic Press (1978); G. Peter Lepage, CLNS-80/447 (1980).

[38] PDFLIB version 3.11, H. Plothow-Besch, Computer Phys. Commun. **75**, 396 (1993); H. Plothow-Besch, CERN Report W5051, (1992).

[39] M. Kobayashi and M. Maskawa, Prog. Theor. Phys. **49**, 652 (1973).

[40] P.N. Harriman, A.D. Martin, R.G. Roberts and W.J. Stirling, Phys. Rev. D **42**, 798 (1990).

[41] The VVJET Monte Carlo, U. Baur, E.W.N. Glover and J.J. van der Bij, Nucl. Phys. B **318**, 106 (1989).

[42] PAPAGENO Monte Carlo version 3.12, I. Hinchliffe, (to be published).

[43] PYTHIA version 5.4, T. Sjöstrand, Computer Phys. Commun. **39**, 347 (1986); T. Sjöstrand and M. Bengtsson, Computer Phys. Commun. **43**, 367 (1987); H.-U. Bengtsson and T. Sjöstrand, Computer Phys. Commun. **46**, 43 (1987).

[44] R.G. Wagner, Comp. Phys. Commun. **70**, 15 (1992); see also F.A. Berends, J.P. Revol and R. Kleiss, Z. Phys. C **27**, 155 (1985); F.A. Berends and R. Kleiss, *ibid.* C **27**, 365 (1985).

[45] F. Abe *et al.*, Phys. Rev. Lett. **63**, 720 (1989); H. Keutelian, Ph.D. thesis, University of Illinois at Urbana-Champaign (1990).

[46] VECBOS Monte Carlo, F.A. Berends, W.T. Giele, H. Kuijf and B. Tausk, Nucl. Phys. B **357**, 32 (1991).

[47] HERWIG Monte Carlo version 5.6, G. Marchesini and B.R. Webber, Nucl. Phys. B **310**, 461 (1988).

[48] Review of Particle Properties, Phys. Rev. D **45**, VI.21, (1992).

[49] Review of Particle Properties, Phys. Rev. D **45**, III.39, (1992).

[50] F. Abe *et al.*, Phys. Rev. Lett. **66**, 2951 (1991); F. Abe *et al.*, Phys. Rev. Lett. **67**, 2937 (1991); B. Winer, Ph.D. thesis, University of California at Berkeley (1991); J. Ng, Ph.D. thesis, Harvard University (1991).

[51] P.B. Arnold and M.H. Reno, Nucl. Phys. B **319**, 37 (1989); P.B. Arnold and R.P. Kauffman, Nucl. Phys. B **349**, 381 (1991).

[52] M. Diemoz, F. Ferroni, E. Longo, and G. Martinelli, Z. Phys. C **39**, 21 (1988).

[53] A.D. Martin, R.G. Roberts and W.J. Stirling, Phys. Lett. B **206**, 327 (1989).

[54] A.D. Martin, R.G. Roberts and W.J. Stirling, Phys. Rev. D **47**, 867 (1993).

[55] J.G. Morfin and Wu-Ki Tung, Z. Phys. C **52**, 13 (1991).

[56] U. Baur, S. Errede and J. Ohnemus, to appear in Phys. Rev. D, and FSU-HEP-930322 preprint, (March, 1993).

[57] MINUIT, F. James and M. Roos, CERN Report D506, 1988.

[58] J. Alitti, *et al.*, Phys. Lett. B **277**, 194 (1992).

[59] D. Brown, Ph.D. Thesis, Harvard University, (1989).

[60] John Huth, *Calorimetry for Superconducting Super-Collider*, Proceedings of the Workshop, Tuscaloosa, Alabama, 1989, edited by R. Donaldson and G. Gilchriese (World Scientific, Singapore, 1990), pp. 27-58.

[61] F. Abe *et al.*, Phys. Rev. Lett. **45**, 1448 (1992).